

## An Interdisciplinary Approach to High Temperature Chemistry

M. P. Freeman

Central Research Division, American Cyanamid Co., Stamford, Connecticut

In the field of high temperature chemistry, and especially as it pertains to the effluent of plasma jet devices, there has always been substantial uncertainty about the nature of the chemistry that one should expect when the initial high temperature stream is cooled to more conventional temperatures, often in the presence of an admixed cold reagent or spectator gas. As a first example, we may cite the cracking of methane in a plasma jet to make acetylene. For this reaction, as is generally the case, one must postulate some sort of "freezing temperature" because, of course, acetylene is unstable with respect to decomposition to the elements at room temperature. Now, three groups of workers have carefully regarded this reaction. One group<sup>1</sup> has established that chemical equilibrium at their mixed mean temperature determines the yield. (They say nothing about what happens at the intervening temperatures.) A second group<sup>2</sup> concluded that not equilibrium, but rather reaction kinetics controls the extent of reaction until the mixture becomes so cold the reaction "freezes;" while the third group<sup>3</sup> showed that the reaction was very fast and that the kinetics of mixing controlled the reaction rate. Again a "freezing" temperature was invoked. Reed<sup>5</sup> has opined that each group was correct but that the conflicting results stemmed from the different reaction conditions and geometries involved.

To cite further examples, consider the well-known fixation of up to 3 or 4% of the nitrogen when a nitrogen-oxygen mixture is passed through a streaming plasma device and the stream rapidly quenched. When Ammann and Timmins<sup>6</sup> withdrew product from a stationary cascade arc through a fine water-cooled probe they obtained an unheard of 12% yield. This must almost certainly be associated with the high cooling rate attributed to such probes. Again, consider the rather substantial body of information that has been accumulated for the reaction of methane with a nitrogen plasma to make HCN.<sup>1</sup> Attempts to interpret these data<sup>7,8</sup> have resulted in two plausible but contradictory mechanisms each of which accounts for the observed results very well indeed. On the one hand,<sup>7</sup> the yield is exactly what one might expect if each N<sup>+</sup> ion in the jet results ultimately in two molecules of HCN. To explain how this can happen, one must disregard considerations of chemical equilibrium and say that somehow the high temperature molecular and ionic fragments 'fall together' in the proper way in the very rapid quenching that results from the mixing process. The equally attractive alternative<sup>8</sup> is that the methane mixes in a quite ordinary way with the nitrogen jet and that the mixture is always in local thermodynamic equilibrium. At some point one has to postulate a "freezing temperature" below which all of the HCN precursors (assumed to be cyano, CN) proceed as before along some inevitable reaction path to the final product. The rather sophisticated computer program has never been made available for critical appraisal, but assuming it to be a straightforward result, one must ask whether it shouldn't be possible to differentiate between such diametrically opposed concepts by a consideration of the relevant time scales. Indeed one might suppose this would be standard operating procedure.

In the face of such evident need, it is interesting to ask why so little has been accomplished along these lines. Or to rephrase the question, what factors conspire to place such an analysis outside the accepted purview of "chemistry" or "chemical engineering?" The first factor that comes to mind is the real paucity of information about any of the characteristics, but especially the characteristic times of such strongly cooled fluid flow. Is it reasonable to even think about meaningful quenching rates? Another factor is that the whole concept of "freezing" a reaction has always been a bit nebulous to the chemist. Although the transition from frozen flow to equilibrium flow is of vital importance, the chemist has always been pragmatically interested in forcing the situation one way or the other and has had little interest

in systematic study of the compromise situation. Similarly experimental purists and theoretical chemists have generally tried to avoid non-isothermal situations in view of their general analytical intractability. It is in fact only with the advent of streaming thermal plasma devices (and of reentry) that velocities and residence times have achieved such extreme values that one might expect elementary reaction steps to be spatially resolved and temperature changes to be so abrupt that atomic, ionic, and free radical reactions may not proceed along their anticipated course (c.f. the inexplicable inactivity of N atoms in HCN synthesis).

The purpose of the present work is to attempt to formulate a framework for examining these questions and to try the formulation out on a nitrogen plasma configuration. In the next part we formulate an expression for a critical quenching rate vs temperature. In the following section we examine the cooling sequences of a few plasma jet devices under various conditions and establish that "frozen flow" is probably the rule for both ionic and atomic recombination. Finally, we speculate a little on where one might expect this to lead, introducing the concept of characteristic reaction times so as to facilitate choosing between alternatives in the frozen flow regime.

### Threshold Frozen Flow

The problem starts with a fully equilibrated high temperature flow system. The concentration of some species, thought to be chemically relevant, emerges from, say, a free energy minimization program<sup>9</sup> or, in some cases, a simple equilibrium calculation.<sup>3</sup> In either case, we represent the concentration of the interesting species (in moles cm<sup>-3</sup>) by  $(\Gamma)$ :

$$(\Gamma) = f(N_A, N_B, \dots; P, T), \quad (1)$$

where  $P$  and  $T$  have their usual significance and  $N_A, N_B, \dots$  represent the component molar composition of the mixture (as opposed to the species composition). If we now cause the temperature of this mixture to decrease we may formally write for the time rate change of  $(\Gamma)$ :

$$d(\Gamma)/dt = \partial(\Gamma)/\partial T \partial T/\partial t = \partial f/\partial T \cdot \partial T/\partial t, \quad (2)$$

where  $t$  represents time. The equilibrium value at temperature  $T$  of the concentration of the species of interest,  $(\Gamma)$ , is the result of a balance between a set of rapid forward and reverse reactions:

$$d(\Gamma)/dt \Big|_{\text{equil}} = \sum_i \left\{ -k_f i (\Gamma)(A_i)(B_i) + k_r i (A_i)(E_i)(Z_i) \right\}. \quad (3)$$

At equilibrium at constant temperature both sides of Equation 3 are equal to zero by definition of the equilibrium process. As long as the temperature change is sufficiently slow that

$$d(\Gamma)/dt \Big|_{\text{equil}} \ll (\Gamma) \sum_i \left( -k_f i (A_i)(B_i) \right) \approx \sum_i k_r i (A_i)(E_i)(Z_i), \quad (4)$$

where the left-hand side of Equation 4 is determined from Equation 2, we say that we have equilibrium flow. If on the other hand, the absolute value of the left-hand side, calculated again from Equation 2, is much larger than that of either of the right-hand terms in Equation 4, then kinetic considerations preclude maintaining any semblance of an equilibrium composition; and we say we have frozen flow. In a classic work, Bray<sup>10</sup> performed suitable calculations for air expanded through a hypersonic nozzle and showed that this cross over from fully equilibrated to fully frozen flow is very abrupt. The results of his detailed calculation indicate in fact that the transition may be considered discontinuous, and he suggested modeling it in this way. He went

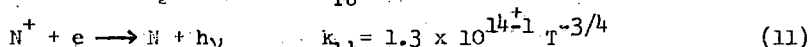
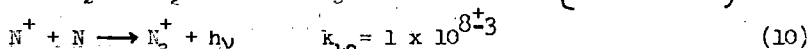
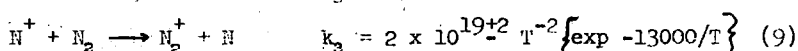
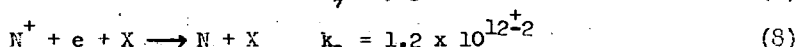
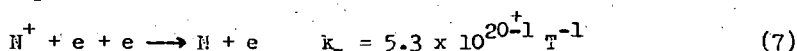
on to argue (though indirectly) that any criterion guaranteed to lie well within this transition region could therefore be used to establish the freezing condition. In his case the condition would be a particular expansion ratio, say; in the present somewhat more general argument the condition will be the result of any or several of many different temperature changing mechanisms, adiabatic expansion, reaction heat, thermal conduction, addition of a cold gas or liquid spray diluent, etc. The criterion suggested by Bray is:

$$\left. \frac{d(T)}{dt} \right|_{\text{equil}} \approx (T) \sum_i \left\{ -k_f (A_i) (E_i) \right\} \approx \sum_i \left\{ k_r (A_i) (E_i) (Z_i) \right\} = \text{URR}(T), \quad (5)$$

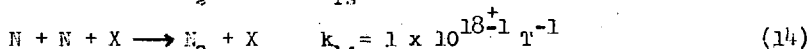
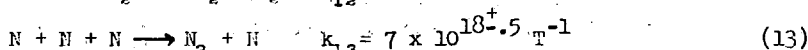
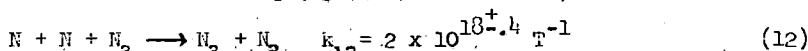
where  $\text{URR}(T)$  represents the total unidirectional reaction rate. Combining Equations 2 and 5 we obtain for the cooling rate required for frozen flow:

$$\left. \frac{dT}{dt} \right|_{\text{freezing}} \approx \frac{\text{URR}(T)}{\frac{\partial}{\partial T} \{ f(N_A, N_B, \dots; P, T) \}}. \quad (6)$$

**Numerical Example.** To implement Equation 6, we introduce now the nitrogen system. Curves of the equilibrium particle densities for nitrogen at 1 atm are shown in Figure 1. It is immediately clear by inspection that one need consider but one equilibrium at a time, for at no temperature available to chemists are more than two species present in chemically significant amounts; however, for the moment we use Figure 1 itself. Nearly every reaction rate of interest for this system may be found in a compendium by Bortner.<sup>12</sup> We consider first the principle reactions destroying the  $N^+$  species.



Reaction 11, radiative recombination, dominates at temperatures of 10,000°K and above, while reaction 9, charge exchange, dominates at lower temperatures. Perfectly straightforward numerical application of these rate expressions together with equilibrium values of species concentrations and their derivatives obtained from Figure 1, yields a curve demarcating the cooling rate regime in Figure 2 within which we expect equilibrated ion flow (right-hand shaded region). The calculation was stopped at 12,500°K on the one hand because this corresponds to a good jet center temperature, while it was stopped at 9500°K on the left because below this temperature the number of ions is uninteresting. Similarly the left-hand shaded region shows the cooling rate regime in which we expect equilibration between atoms and molecules. This regime is calculated from the following (again from Bortner<sup>12</sup>):



Above 8000°K, molecular nitrogen has disappeared completely, while below 4000°K there is no atom population of consequence.

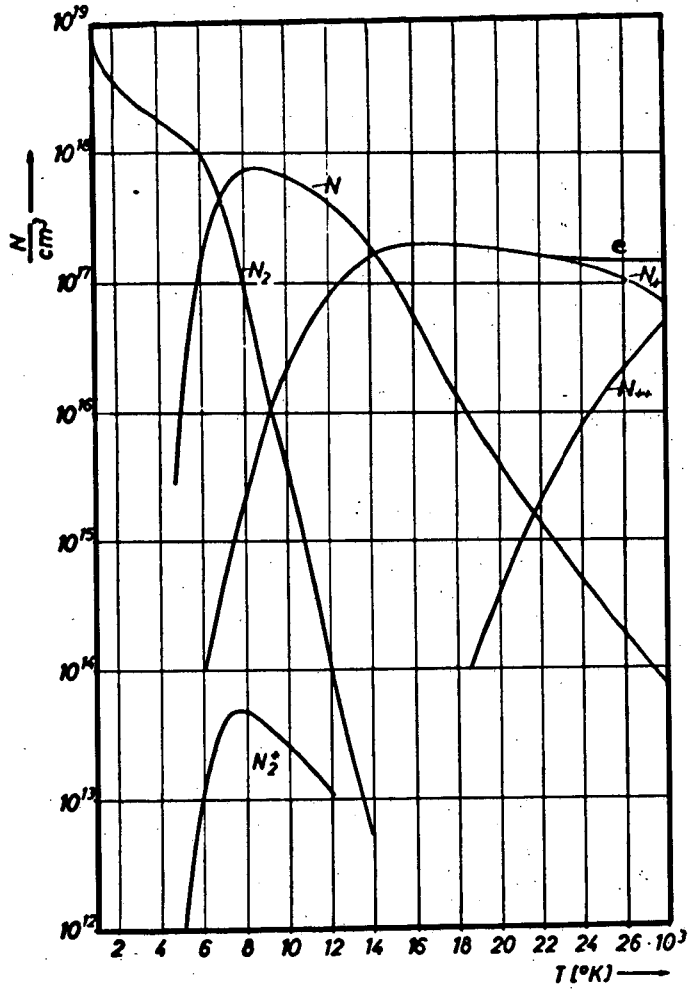


Figure 1: Particle densities of nitrogen at 1 atm total pressure as a function of temperature.

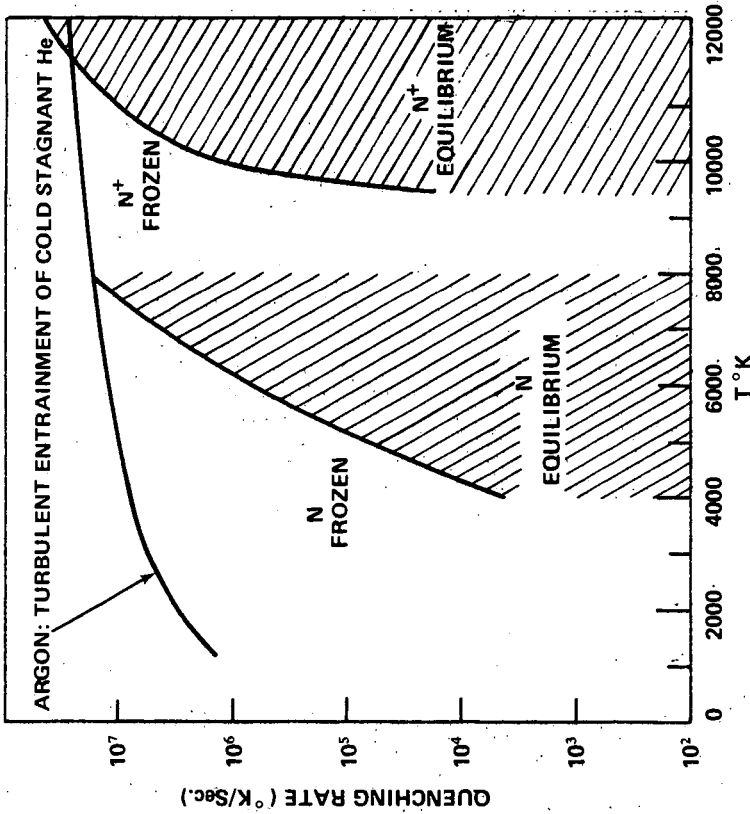


Figure 2: Shaded regions showing for nitrogen at 1 atm cooling rate regimes in which we might expect equilibrated atom-molecule flow (left-hand region); and ion-atom flow (right-hand region). The line shows cooling rates typical of turbulent entrainment by a laboratory scale plasma jet.

Characteristic Reaction Time. It is instructive at this point to examine characteristic times for these reaction rates so as to gain more appreciation for the speed at which significant chemical events occur from a more conventional viewpoint. Considering now just the rate expressions, at any temperature the reciprocal of  $1/N \, dN/dt = d \ln(N)/dt$  will give the time required (by extrapolation of a tangent to the curve) for the concentration of the species of interest to decrease to  $1/e$  of its value. At  $12,500^\circ\text{K}$  and  $10,000^\circ\text{K}$  the characteristic times are 64 and 320  $\mu\text{sec}$ , respectively. Similarly defined atom/molecule relaxation times at  $8000^\circ\text{K}$  and  $5000^\circ\text{K}$  are 413  $\mu\text{sec}$  and 13.4 msec, respectively. To place these numbers in perspective, it has previously been estimated<sup>14</sup> that under typical laboratory conditions for a tube confined flow at  $\frac{1}{2}$  atm, a peripherally added reagent has a characteristic mixing time of about 60  $\mu\text{sec}$  which requires about 1 cm of jet travel.

### Characteristic Quenching Rates

As of the present time, the actual quenching rates achieved in various high temperature flow configurations are not at all well known; however, it is necessary to make some estimate of these rates for comparison with the critical freezing rate of the preceding section. We will, therefore, do the "best we can" for two very important situations, turbulent entrainment of a cold stagnant gas on the one hand and simple cold-walled tube confined flow on the other. There are, of course, other familiar quenching situations: cold liquid quenching, cold doorknob impingement, peripherally pumped coolant added to a tube confined jet, and many others which have not yet yielded to analysis, but which almost certainly lie between the two extreme methods analyzed here.

Thanks to the experimental work of Grey and his co-workers<sup>13,14,15</sup> we have experimental results for the very important situation where a  $3/4$ " diam argon jet (350scfh) is allowed to turbulently entrain a surrounding essentially stagnant cold helium sheath. This should provide a lower bound to the quenching rate for practical purposes; certainly nitrogen entraining methane would have at least a comparable cooling rate. A curve derived from their data is shown in Figure 2 and clearly demonstrates the characteristic high cooling rate that is nearly independent of temperature. Frozen flow must clearly be expected for this quenching method. The second flow situation that has been experimentally characterized is for cold-wall contained plasma flows. In Figure 3 "tube average" curves are presented for various initial conditions.<sup>16</sup> The curves come from the relation

$$\frac{dT}{dt} = \frac{\frac{\partial h(T)}{\partial z} \frac{\partial z}{\partial t}}{\frac{\partial h(T)}{\partial T}} \quad (15)$$

where  $h(T) = H(T) - H(298)$  and is related to the axial coordinate  $z$  by the relation<sup>16</sup>

$$\frac{h(T)}{h(T_0)} = \left( \frac{s}{z + s} \right)^{2/3} \quad (16)$$

In this expression  $s$  is a characteristic flow development length and is experimentally on the order of 10 diameters (to within a factor of 2). Using the continuity equation for the velocity term we obtain:

$$\frac{dT}{dt} = \frac{-\frac{2}{3} \frac{G}{A s} \left\{ \frac{h(T)}{h(T_0)} \right\}^{3/2}}{\rho(T) \frac{\partial \ln[h(T)]}{\partial T}} \quad (17)$$

For the curves shown,  $G/A$  is taken as  $0.07 \text{ moles cm}^{-2} \text{ sec}^{-1}$ ,  $s$  as 5 cm and  $\rho(T)$  and  $h(T)$  are taken from the extensive tables for nitrogen published by Hilsenrath and

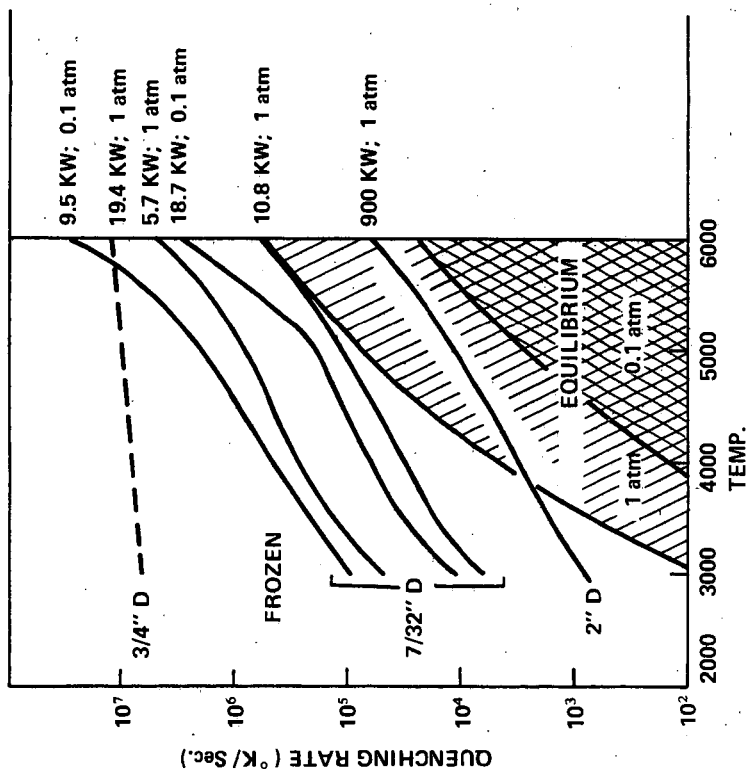


Figure 3: Characteristic quenching rates for various "tube average" flow configurations and entry conditions. The dashed line is again the curve representing turbulent entrainment of stagnant cold helium by an argon jet (Figure 2). Equilibrium flow regimes are shown for nitrogen at 0.1 atm and 1 atm, respectively.

and Klein.<sup>17</sup> The values of  $T_0$  shown, much lower than actual entrant centerline temperatures, were chosen to correspond to easily attainable net entrant power levels for gas flows of .017 g mole sec<sup>-1</sup>. Note that all else equal, a quenching rate a factor of 10 higher would be obtained with a .020" quenching probe.<sup>6</sup>

On the same figure equilibrium flow regimes are shown for the nitrogen atom/molecule reaction at 0.1 atm and 1 atm, respectively. To the extent the "tube average" curves may be believed, we can draw the conclusions that equilibrium flow is possible in a tube. It is favored by

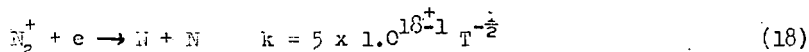
- larger diameters (quenching rate is inversely proportional)
- higher pressures
- higher power levels.

One may equally well infer that frozen flow is also possible in tubes. In particular, a .020" diam tube might very well be used to "freeze" a flow with very nearly the same efficiency as turbulent entrainment.

The "tube average" curves may drastically understate the quenching in a tube, of course. Figure 4 illustrates, in a very exaggerated way, that while the "tube average" model takes a flow from 7000 to sub-thousand temperatures in a few milliseconds, in actual fact nearly one-fourth the total flow is at 12,000°K and goes to sub-thousand temperatures in (probably) comparable times. Calculations are currently in progress to see if any great discrepancy is encountered; however, Figure 3 agrees so well with the writer's experience that it seems unlikely that any surprises will arise in this area.

### Discussion

Frozen flow is generally necessary at some point for the recovery of useful products. It is clear from the trends displayed in the preceding sections that freezing is generally inevitable and in fact generally to be expected at fairly high temperatures in laboratory scale units (but not necessarily at such high temperatures for the larger production units, such as the Westinghouse unit described at this meeting). Once the fact of frozen flow has been established, one may examine relative characteristic reaction times (such as defined above) to test the feasibility of proposed reaction mechanisms (or alternatively by rearrangement of Equation 6 to establish a limiting value on reaction rates when the information is unavailable). Just by way of illustration, consider one interpretation of the HCN experiments cited above that involves an  $N_2^+$  intermediate (a specie not favored by equilibrium). It is now clear that under the reaction conditions the composition of the flow freezes long enough to intermix well with the carbon-containing species while still several per cent ionized. That is, the quenching rate is 20 to 30°K ( $\mu$ sec)<sup>-1</sup> while the characteristic reaction time (see above) for the radiative recombination of  $N^+$  and  $e^-$  lengthens from 64  $\mu$ sec at 12,500°K to 320  $\mu$ sec at 10,000°K. Thus, we arrive with most of our ions intact at a temperature where formation of  $N_2^+$  by charge exchange (Equation 11) is the fastest available  $N^+$  ion removing reaction (characteristic time = 150  $\mu$ sec). However,  $N_2^+$  has virtually no chance of participating directly in bulk chemistry because of the extremely fast dissociative neutralization reaction



which clearly has a characteristic time of about 10<sup>-10</sup> seconds. Thus, if the ions do participate in this reaction, it must be through carbon-containing moieties as intermediates. By the same token, however, the alternative explanation, that of fully equilibrated flow, seems equally untenable in light of the present considerations.



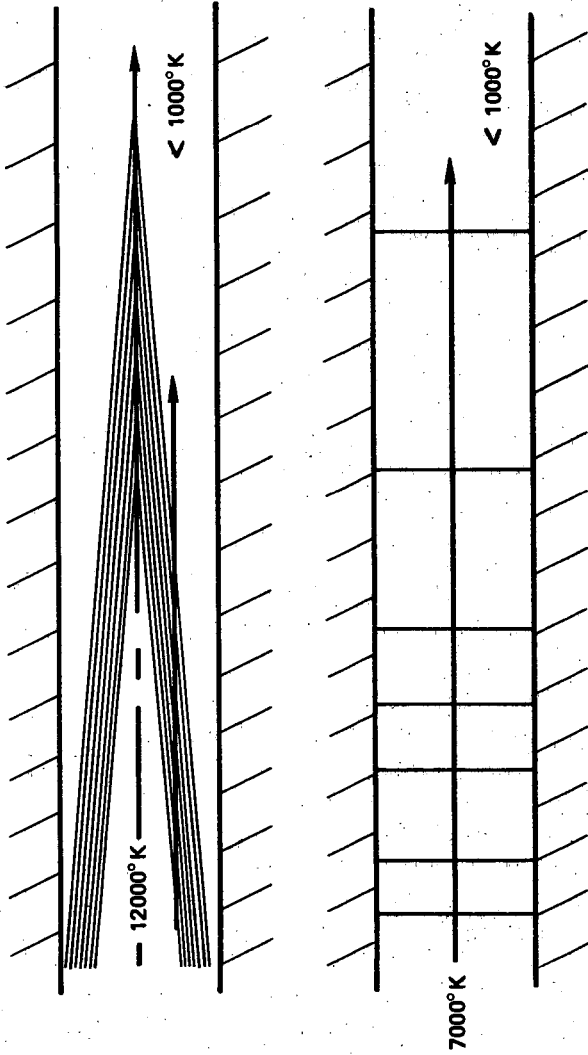


Figure 4: Isotherms for the "tube average" model (bottom) compared to the highly exaggerated decay of the more realistic isotherms of the hot center jet.

## Conclusions

By taking a freezing criterion from aerodynamics and quenching and chemical kinetic rate data from whatever sources available, it is clear that it is possible to bring new light to bear, however poorly in focus, on the subject of high temperature chemistry, particularly that of streaming thermal plasmas. Especially for tube confined plasmas, the trends with changes in total pressure, tube diameter and input power density are seen to be straight forward. Turbulent entrainment of a stagnant cold gas is seen to be fast enough to freeze even the simplest reactions in the nitrogen plasma system (excepting the dissociative neutralization of  $N_2^+$ ) while fine probes are seen to be nearly as good. Finally, the concept of "characteristic reaction time" has been invoked to help examine illustratively the plausibility of a particular reaction mechanism in a frozen flow regime.

## References

1. M. P. Freeman, *Advan. High Temperature Chem.*, 2, 151 (1969).
2. V.G. Melamid, T.A. Mukhtarova, L.S. Polak, and Y.L. Khait, "Kinetika i Termodynamika Khimicheskikh Reaktsii v Nizkotemperaturnoi Plazme" (L. S. Polak, ed.) p. 12, *Inst. Neftekhim Sinteza Akad. Nauk SSR* (1965).
3. J. E. Anderson and L. K. Case, *Ind. Eng. Chem. Process Design Develop.*, 1, 161 (1962).
4. M. P. Freeman and J. F. Skrivan, *A.I.Ch.E.J.*, 8, 450 (1962).
5. T. B. Reed, *Advan. High Temperature Chem.*, 1, 259 (1967).
6. P. R. Ammann and R. S. Timmins, *A.I.Ch.E.J.*, 12, 956 (1966).
7. M. P. Freeman and C. C. Mentzer, *Ind. Eng. Chem. Process Design Develop.*, 9, 39 (1970).
8. B. R. Bronfin and L. S. Cohen, *Proc. Third Int. Symp. High Temp. Technol.* (1967), Butterworths, London and Toronto, p. 433.
9. D. R. Cruise, *J. Phys. Chem.*, 68, 3797 (1964).
10. K. N. C. Bray, *Fluid Mech.*, 6, 1, (1959).
11. F. Burhorn, *Z Phys.*, 155, 42 (1959).
12. M. H. Bortner, "Chemical Kinetics in a Reentry Flow Field," AD418159 (1963).
13. P. F. Jacobs and J. Grey, "Turbulent Mixing in a Partially Ionized Gas," Princeton University Aeronautical Engineering Laboratory Report No. 625, October, 1962.
14. P. M. Williams, M. P. Sherman, P. F. Jacobs and J. Grey, "Heat Transfer from a Partially Ionized Gas to a Gaseous Coolant," Princeton University Aeronautical Engineering Laboratory Report No. 651.
15. J. Grey and P. F. Jacobs, *AIAA J.*, 2, 433 (1964).
16. J. F. Skrivan and W. Von Jaskowsky, *Ind. Eng. Chem. Process Design Develop.*, 4, 371, (1965).
17. J. Hilsenrath and M. Klein, "Tables of Thermodynamic Properties of Nitrogen... 2000°K to 15,000°K," AD432210 (1964).

## DIAGNOSTIC TECHNIQUES FOR HIGH TEMPERATURE PLASMA REACTIONS\*

J. H. Mullen, J. M. Madson, L. N. Medgyesi-Mitschang, T. C. Peng, P. M. Doane

McDonnell Douglas Research Laboratories  
McDonnell Douglas Corporation  
St. Louis, Missouri 63166

## Introduction

Numerous experimental techniques have been employed in the study of interactions between charged and neutral constituents of a plasma. The particular technique employed in any experiment has been determined by the phenomena under investigation. In particular, beam and drift tube experiments as well as afterglow techniques have been used to study phenomena such as ionization, electron recombination and electron attachment in a temperature range near room temperature. Some recent measurements on the electron attachment process have been made at elevated gas temperatures where the reaction products were analyzed with a mass spectrometer<sup>1,2,3</sup>. The usual limitation on the gas temperature in these experiments is the maximum working temperature of the material used for the target gas heater. Electron recombination, electron attachment and ion-molecule reaction processes in plasmas have also been studied using a flowing afterglow technique<sup>4,5</sup>. This technique has an advantage over the stationary afterglow method for reaction rate studies in that it permits the injection of target molecules into a flowing plasma stream without subjecting these molecules to the main discharge excitation mechanisms. However, temperatures used in flowing afterglow studies have usually been less than 600°K. To study these processes at higher temperatures and in particular temperatures encountered by reentry vehicles (2000 - 4000°K), plasma discharges having these high temperatures must be employed. For these studies arc heated plasma sources have been used with both subsonic channel flows<sup>6</sup> and supersonic free jets<sup>7,8</sup>. Interpretation of experimental results is difficult with both of these techniques because of the inhomogeneity of plasma parameters in the reaction region. The system described in this paper encompasses the desirable aspects of the above mentioned approaches and enables quantitative reaction rate measurements to be made<sup>9</sup>.

## Overall System Description

The experimental apparatus shown in Fig. 1 is composed of a plasma source, chemical reaction channel, expansion region and mass analysis chamber. The gases, heated in an electrodeless induction plasma discharge, react with supersonically injected target molecules in a sonic reaction channel and are subsequently "chemically frozen" by rapid expansion in a free molecular jet. The electron density, excitation temperature, electron temperature, and gas temperature of the plasma at the source is measured with an optical spectrometer, an X-band microwave radiometer, and high temperature thermocouples. In addition, excitation temperatures are also measured in the reaction channel. Free electron number densities and ion-molecule intensities in the free expansion region are measured simultaneously with a Ka-band microwave interferometer and a free jet ion-molecular beam mass sampling system using a quadrupole mass spectrometer. The design, construction and particulars of the plasma system and instrumentation will be described subsequently.

\*This research was conducted under McDonnell Douglas Independent Research and Development Program

**Figure 1 Schematic Drawing of Experimental Apparatus**

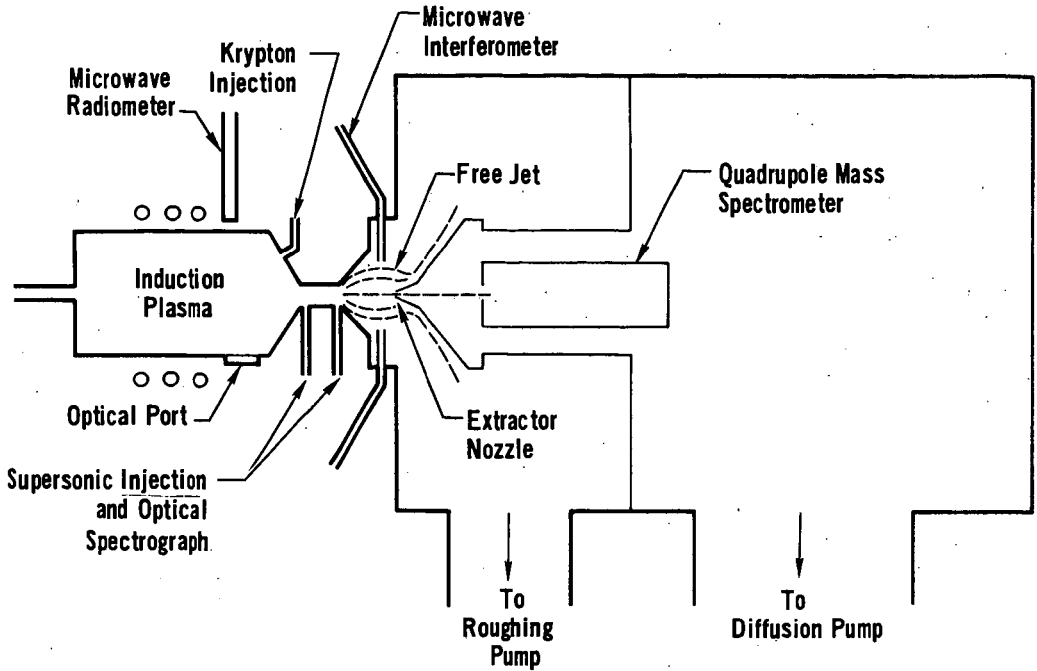
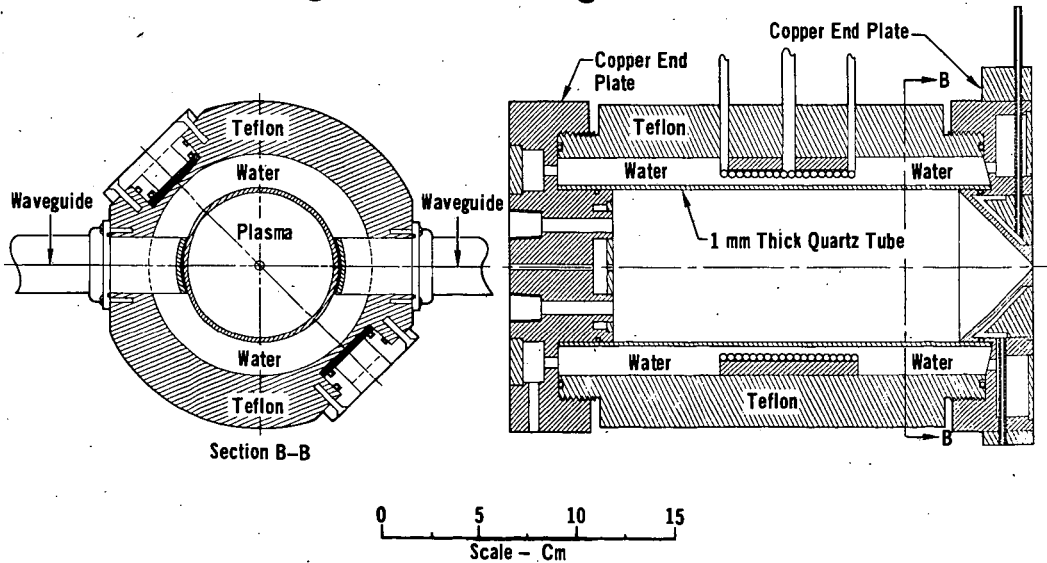


**Figure 2 rf Discharge Chamber**



## Plasma Source

An electrodeless induction plasma similar to those of Reed<sup>10</sup> and Eckert, et al<sup>11</sup> is used as the plasma source. A 0 to 100 kW, class C, rf oscillator operating at 1 MHz is used to supply the plasma heating power. This plasma source eliminates electrode contamination of the plasma in the chemical reaction channel and permits uniform heating of the plasma with electron temperatures close to the gas temperature in the central core region. A scale drawing of the discharge tube is shown in Fig. 2. The 80 mm diameter plasma discharge tube is made of 1 mm thick quartz, approximately 160 mm long. The ends are made to fit the O-ringed copper end pieces by padding standard diameter quartz tubes on machined carbon mandrills mounted in a glass blowing lathe. Allowance has to be made for the expansion of the carbon during this step. The end plates (threaded for assembly to the water jacket) are made of copper and are water cooled. The water jacket is machined from a 203 mm O.D. - 101 mm I.D. cast Teflon tube and handles a 1.14 l/sec flow rate. Two oppositely wound, eight turn coils of 3 mm O.D. copper tubing surround the plasma discharge tube and are mounted collinearly inside the water jacket. A 1.5 mm clearance between the discharge tube and the water jacket gives adequate coolant water flow. To prevent rf sputtering between the coils and the copper end plates, the coils are center fed and grounded at the ends so that the rf plasma potential is minimum at each end of the discharge. In this configuration, the quartz plasma tubes have operated for more than 100 hours before failure.

In operation, the plasma is initiated at low power at  $10^{-3}$  to  $10^{-1}$  Torr pressure. After initiation the discharge can be operated from 1 to 760 Torr at oscillator power inputs ranging from 1 to 69 kW using argon. On air the discharge can be operated from 1 to 600 Torr with power inputs from 20 to 100 kW. At low oscillator power inputs (i.e. < 39 kW) a tungsten rhenium thermocouple is used to measure the local gas temperature of the plasma at the entrance to the plasma channel. These measured temperatures for various argon mass flow rates are shown in Fig. 3 as a function of source pressure. The source pressure is controlled by changing the oscillator power input. Above 2850°K the thermocouple melted. The dashed lines represent theoretically predicted curves based on gas dynamic considerations. The deviation at the higher mass flow rates and high temperatures apparently is due to bending of the thermocouple from the center of the channel. Gas temperature data above this range is difficult to obtain. However, by monitoring the source pressure at higher powers the temperature can be predicted from the theoretical curve. Because the gas is sonic at the thermocouple, the temperature derived from Fig. 3 must be multiplied by 1.33 to obtain the source chamber temperature. The highest operating chamber pressures are indicated by a star in Fig. 3 and show the maximum temperatures obtainable. These points were limited by the maximum plate current of the oscillator triode (10 amperes) rather than the maximum power capability of the triode itself. An improvement in power output is possible by reducing the number of turns on the plasma coil. When gas mixtures such as air which contain diatomic molecules are used, loading of the oscillator is sufficiently low so the maximum plate current coincides with maximum power. The design described here is a compromise that provides operation on monatomic as well as diatomic gases without mechanical or electrical modifications. Table I shows typical operating conditions for the plasma source operating on argon and air.

## Optical Spectrographic Measurements

To interpret the chemical reactions in the channel it is necessary to know the electron temperature of the plasma in the source and reaction channel. In most electric discharges there is some degree of nonequilibrium between the electron and gas temperatures. Simple techniques such as thermocouples can not be used to determine both of these temperatures because the energy in the free electrons represents only a small fraction of the total energy in the gas. Langmuir probes were not

Figure 3 Channel Gas Temperatures

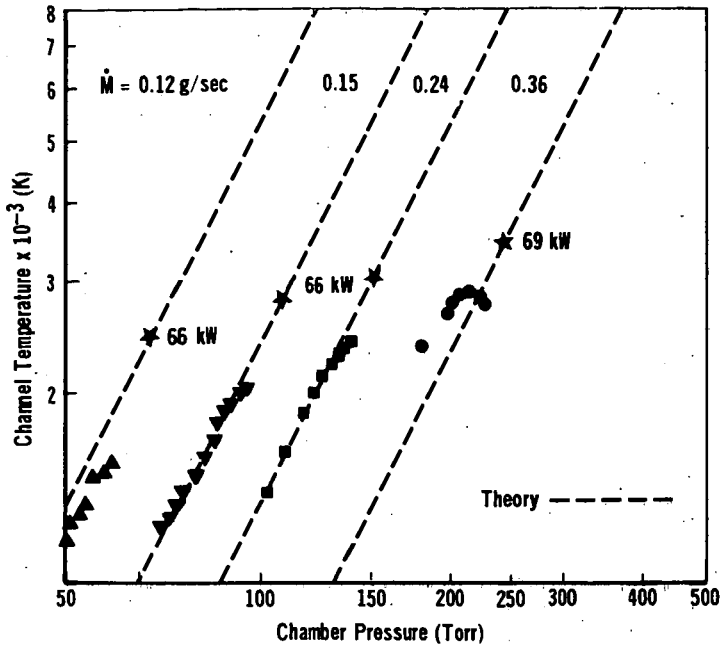


Figure 4 Radiometer Schematic

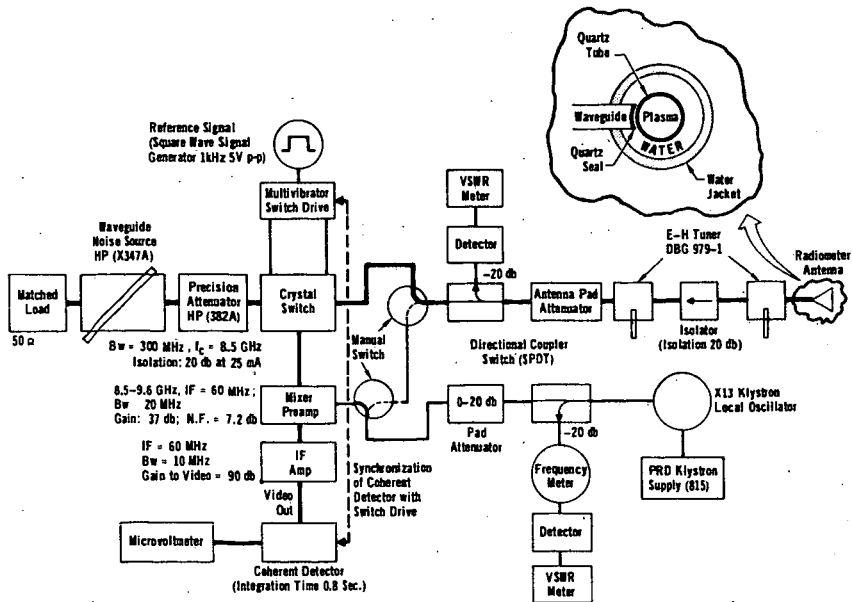
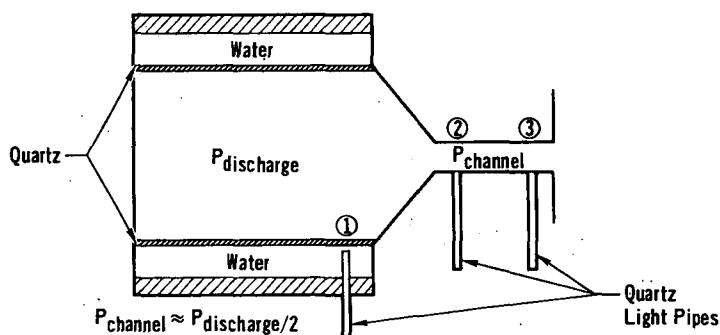


Table I Typical rf Plasma Operating Conditions

Line Power (kW)	M g/sec	Discharge Pressure (Torr)	Plate		Grid		Filament		rf Generator Efficiency (%)	Gas
			V (kW)	I (Amp)	V (kV)	I (Amp)	V (Volt)	I (Amp)		
90	0.104	165	8.5	10	1.0	0.94	12.7	195	58.0	Air
85	0.130	206	8.5	9.5	1.13	1.00	12.7	195	58.5	Air
95	0.163	258	9.2	9.7	1.25	1.14	12.8	200	60.9	Air
100	0.326	542	10	9.8	1.55	1.40	12.8	200	62.0	Air
6	0.193	139*	2.8	2.55	0.07	0.06	12.8	200	~50	Argon
24	0.193	166*	4.5	5.1	0.27	0.18	12.8	200	~50	Argon
66	0.193	164	6.55	9.65	0.74	0.30	12.8	200	~50	Argon
69	0.273	247	6.65	9.85	0.77	0.31	12.8	200	~50	Argon

\*With Thermocouple in Channel

Table II Spectrographically Measured Excitation Temperatures



Discharge Chamber Pressure (Torr)	T <sub>1</sub> Chamber Temperature (K)	T <sub>2</sub> Channel Upstream Temperature (K)	T <sub>3</sub> Channel Downstream Temperature (K)
51.7	8820	5560	5600
103	8540	—	—
155	8480	5260	5390
310	11810	6020	—
465	10326	—	5350
620	8510	6410	4120

used because of the difficulty involved in inserting them into the source and interpreting the resulting data. Furthermore, any perturbation introduced by them in the discharge region causes devitrification and rapid failure of the quartz tube. Optical spectrographic techniques<sup>12,13,14</sup> were found to be applicable.

Spectrographic observations of the plasma at the source and at two axial positions in the reaction channel were made. Aluminized quartz light pipes were used to direct the light to a one-meter (Jarrell Ash Model 78-466) spectrograph. Excitation temperatures were obtained at the three positions and for various flow conditions shown in Table II. The discharge chamber temperature at 310 and 465 Torr are thought to be in error as a result of a discharge instability in this pressure range and the slow response of the strip chart recorder. The excitation temperatures were obtained from Boltzmann plots of Ar I line intensities. The entire optical system (including the light pipes) was calibrated between 5000 and 4000 Å using a tungsten ribbon filament lamp.

In the optical measurements, the excitation temperature was assumed to be close to the electron temperature due to the efficient energy exchange between free electrons and the upper bound electronic states. Electron density measurements were attempted using line profile and continuum techniques. Plasma source operating conditions were 114 Torr and 51 kW of rf power. No line broadening was detected indicating that the electron densities were less than  $1.0 \times 10^{16}$  e/cm<sup>3</sup>. The electron density calculated from the Kramers - Unsöld equation for continuum radiation was  $1.5 \times 10^{16}$  e/cm<sup>3</sup>.

#### Microwave Radiometer Measurements

In addition to the optical spectrographic excitation temperature measurements of the plasma source the electron temperature was measured using radiometric techniques. As is known the emitted spectrum of any homogeneous source becomes more continuous as the depth of the source increases, since initially the strongest lines tend to be reabsorbed, then the weaker ones, and eventually all parts of the continuum until the spectrum resembles a blackbody continuum<sup>15</sup>. However, in the laboratory this happens at best over a rather limited frequency range. (If this were not the case, radiative energy losses would be formidable.) Ordinarily in the microwave frequency range no line spectra are present and only continuum radiation occurs. In laboratory plasmas with plasma frequencies above the radiometer frequency considerable reflection of the continuum radiation at the plasma-air interface occurs resulting in very low levels of radiated power.

For the radiometric measurements a modified Dicke X-band microwave radiometer operated at 8.5 GHz shown in block diagram form in Fig. 4 was used<sup>16,17,18</sup>. In operation the radiometer is electronically switched between the plasma source and a standard noise source. A standard noise source and a 50 dB precision attenuator combination form a 10,000°K calibrated blackbody temperature standard against which the temperature of the plasma is compared. The difference in thermal radiation between the plasma and the standard is detected, amplified, and processed by the radiometer as follows<sup>19,20</sup>. The signal is passed through a balanced low-noise mixer IF pre-amp combination, followed by a high gain IF amplifier. This is followed by a coherent detector in synchronism with the electronic X-band switch and the output is read on a precision microvoltmeter<sup>21</sup>.

The radiometer receiving antenna is a contoured open-ended waveguide, capped by a similarly contoured 1.5 mm thick quartz window (Fig. 2). The waveguide is oriented so that the E-plane is parallel to the axis of the discharge chamber, resulting in the smallest amount of mismatch. Because of the small radiation signal from the source, this mismatch was tuned out.



To accomplish this, the following modifications were adopted from the conventional radiometer. Provision was made to operate the system in a non-radiometer mode via a "test loop". In this mode, the local oscillator (L.O.) signal is passed directly to the radiometer antenna through a set of manual switches by-passing the remainder of the circuit, allowing simple transmission and reflection measurements to be made. Due to the high plasma density ( $N_e > 10^{15}$  e/cm<sup>3</sup>), no transmitted signal through the plasma could be measured as signal attenuation exceeded 60 dB. The E/H tuner closest to the antenna was adjusted for maximum noise signal in the usual radiometer mode with the discharge operating at 150 Torr. The other E/H tuner was tuned for minimum reflected signal in the test loop mode to eliminate any reflections at the isolator.

The fine adjustment of the radiometer was accomplished in the usual radiometer mode with the antenna attenuator set at maximum and the phase and amplitude of the reference signal in the coherent detector adjusted for maximum deflection on the microvoltmeter.

With the radiometer system adjusted for maximum sensitivity and the antenna network tuned and matched, the radiometer was used for electron temperature determination. The radiation power incident upon the radiometer may be expressed analytically as

$$P = kBT = kB (1-\Gamma) T_p = kB (1-\Gamma) AT_r$$

so that

$$T_r = \frac{P}{kB (1-\Gamma) A}$$

where  $k = 1.38 \times 10^{-23}$  joules/°K (Boltzmann's constant); B is the bandwidth of the incident radiation (Hz);  $\Gamma$  is the reflection coefficient due to the mismatch introduced by the antenna window, the quartz plasma jacket, and the water gap;  $T$ ,  $T_p$  and  $T_r$  are the effective blackbody temperature, plasma blackbody temperature and radiation temperature respectively; A is the absorption coefficient (i.e. equal to the emissivity) which includes reflections at the plasma quartz interface and the plasma absorption.

By proper matching of the radiometer antenna,  $\Gamma = 0$ . The radiation temperature is obtained by setting the precision attenuator in the reference leg so that the radiometer output (on the microvoltmeter) is nulled. In this way a balance is achieved between the plasma and reference leg signals and consequently between the equivalent noise temperatures of the plasma and the standard noise source. The decibel reading on the precision attenuator yields  $T_p$  via the calibration curve which relates the equivalent blackbody temperature to the attenuator setting. From this temperature the electron radiation temperature  $T_r$  can be obtained if A is known. The radiation temperature equals the electron temperature  $T_e$  when the electrons are Maxwellian distributed. Past measurements have shown that the plasma is in equilibrium, at least in the LTE sense, so that the assumption of a Maxwellian distribution is reasonable for the electrons and thus  $T_r$  is assumed equal to  $T_e$ .

To relate  $T_p$  to  $T_r$  (and hence  $T_e$ ), the emissivities were calculated for a slab plasma for a given discharge pressure ( $P_t$ ), fraction of ionization ( $p$ ) and  $T_e$ . In these calculations the electron-ion and electron-neutral interactions were included, using Appleton-Bray<sup>22</sup> for the former and Brown's cross section data<sup>23</sup> for the latter. For the range of  $N_e$  between  $10^{10}$  and  $5 \times 10^{16}$  e/cm<sup>3</sup> and  $T_e$  less than 18,000°K, the electron-ion collisions were found to be dominant. Representative results from these computations for the emissivity as a function of the fraction of ionization

are given in Fig. 5. If the electron density measured with the microwave interferometer is used ( $5 \times 10^{15} \text{ e/cm}^3$ ) to calculate  $\epsilon$  the resulting electron temperature agrees with the spectrographically measured temperature (Fig. 6).

#### Reaction Channel Design

The reaction channel for this system was designed so the plasma chemistry could be most easily interpreted. The channel was made sufficiently long for reaction rates to be determined but not long enough for an appreciable boundary layer buildup or for fully development pipe flow. A well established result of fluid mechanics is that for Reynolds numbers below 2300, flow through a channel will remain laminar even in the presence of strong disturbances in the flow prior to its entrance<sup>24</sup>. The Reynolds number for the channel is

$$R_e = \frac{\rho \bar{u} D}{\mu}$$

where  $\rho$  = density of flow in channel,  
 $\bar{u}$  = average velocity,  
 $D$  = channel diameter,  
 $\mu$  = viscosity of flow in channel.

Using the mass flow relationship  $\dot{m} = \rho u A$ , where  $A$  = channel cross section,

$$R_e = \frac{4\dot{m}}{\pi D}$$

Typical operation conditions are

$\dot{m} = 0.23 \text{ g/sec}$   
 $D = 0.4 \text{ cm}$   
 $\mu \approx 1.1 \times 10^{-3}$  (assuming a  $T^{1/2}$  temperature dependance and  $3000^\circ\text{K}$ ).

The resulting Reynolds number is approximately 700 indicating laminar flow. Experimentally the flow can be made turbulent by increasing the mass flow rate to approximately 1.00 g/sec.

The velocity profile in the transient or inlet portion of a circular channel for laminar flow has been investigated experimentally by Nikuradse<sup>25</sup>. Only after approximately 50 channel diameters downstream would the flow velocity be described by Hagen-Poiseville pipe flow. Using the results of Nikuradse, velocity profiles at several stations for a 1.6 cm channel are shown in Fig. 7. The velocity profile is shown to be nearly flat at the end of the channel indicating no appreciable boundary layer buildup.

#### Target Gas Injection and Mixing

The target gas injection system is composed of a high pressure reservoir, regulator, pressure gauge, needle valve and supersonic orifice mounted in the wall of the channel near the entrance. The orifices are commercially available pinholes, made of 25  $\mu\text{m}$  thick nickel ranging from 35 to 200  $\mu\text{m}$  in diameter. These orifices are silver soldered to stainless steel tubes and mounted in the channel. The orifice is operated above the critical pressure ratios  $P_u/P_c$  (upstream pressure/channel pressure) so target gas injection is always supersonic. If the channel gas were not flowing the position of the first Mach disc would be

$$X = 0.67 D \sqrt{P_u/P_c}$$

Figure 5 Microwave Emissivity at 8.5 GHz

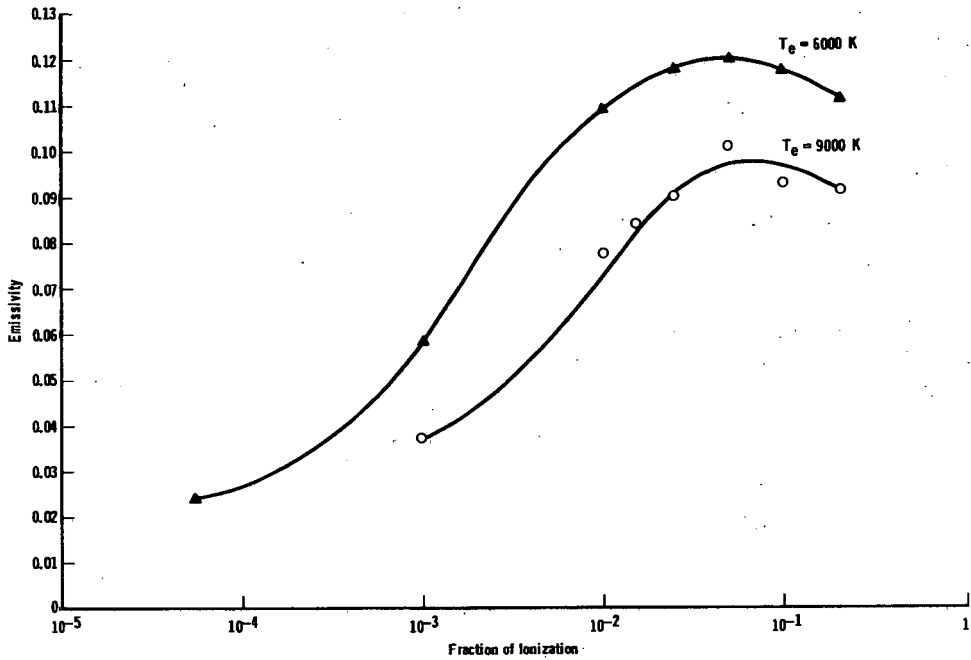


Figure 6 Source Electron Temperature

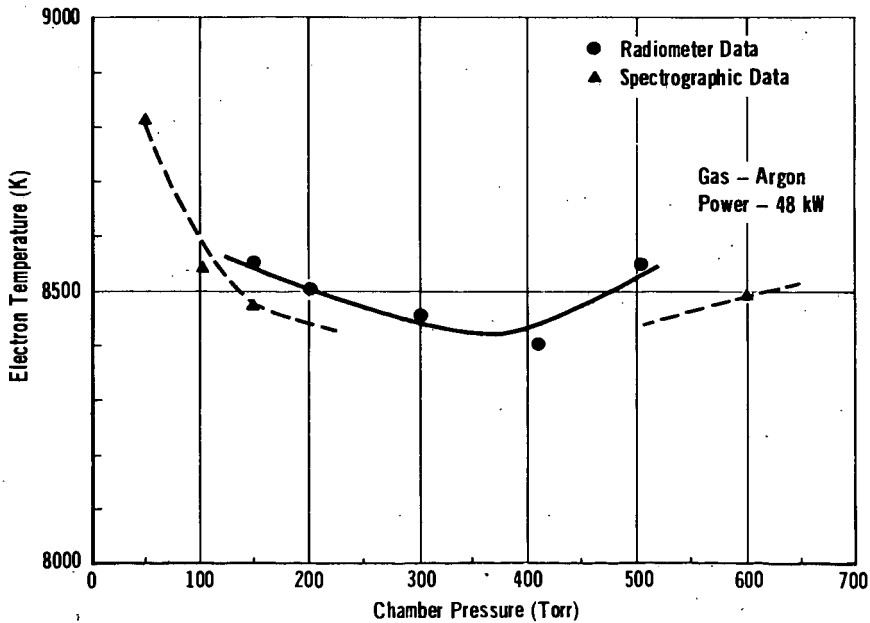


Figure 7 Channel Velocity Profile

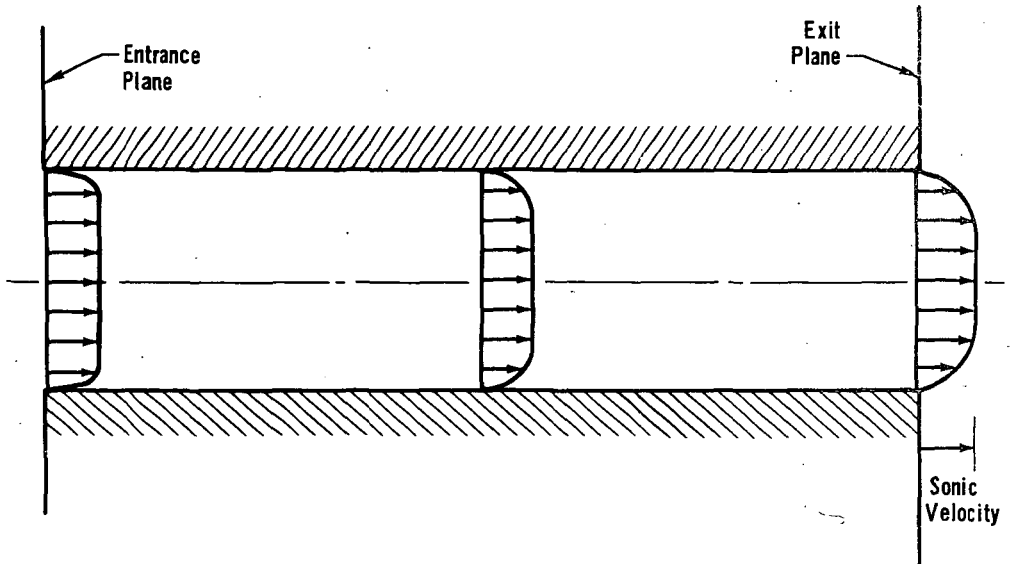
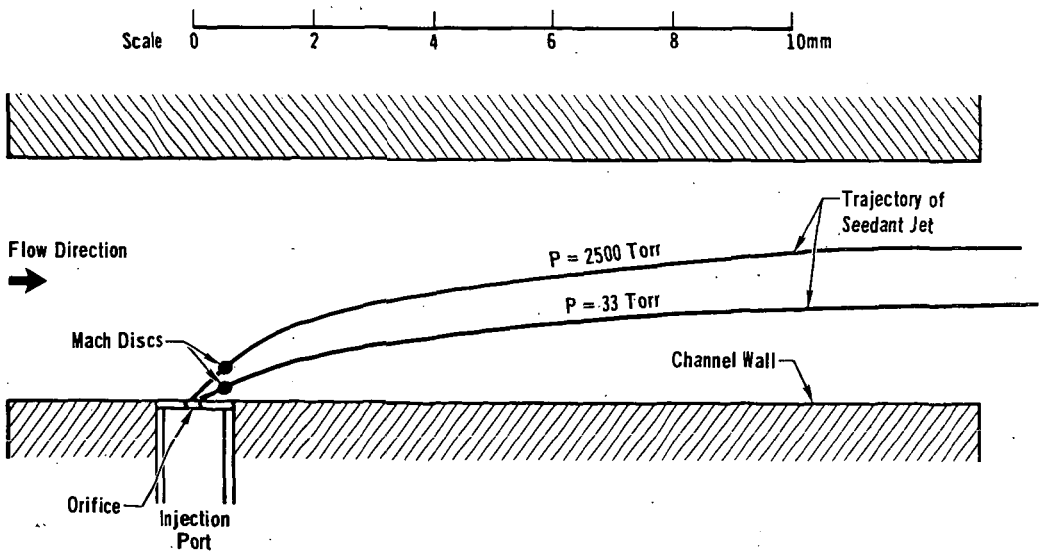


Figure 8 Target Gas Injection



where  $X$  = Mach disc distance from orifice, and  
 $D$  = orifice diameter.

However, the plasma in the reaction channel is traveling at sonic velocity which makes the mixing problem much more difficult. Shandorov<sup>26</sup> and Ivanov<sup>27</sup> have developed an empirical expression for the trajectory of the deflected jet based on experimental studies. They have investigated a range of dynamic pressure ratios from 2 to 22 and for 45° to 90° range of angles between initial injection flow and channel flow. The centerline for two dynamic pressure ratios calculated from these expressions is shown in Fig. 8 as dashed lines. Using the Mach disc location along this centerline and Mach disc diameter given by Crist, et al<sup>28</sup>,

$$\frac{D_m}{D_j} = 0.22 (P_u/P_c)^{2/3},$$

where  $D_m$  = diameter of Mach disc, and  
 $D_j$  = diameter of orifice,

the Mach disc is shown superimposed for a 200  $\mu$ m orifice. The nature of the flow after the Mach disc is probably free turbulent flow. The lifetime of this turbulent flow is uncertain, since the channel main flow is strongly laminar ( $Re \approx 700$ ) and will eventually damp out the turbulence.

From this target gas injection analysis, it is apparent that care must be taken in interpreting chemical reactions in the channel. Rate constants evaluated from this experiment also include mixing rates. However, since the  $\ln$  of the electron density as a function of target molecule density is linear over a large range mixing appears to be no problem. The mixing could obviously be improved by using three injection nozzles around the circumference of the channel spaced every 120°. This modification is presently being incorporated.

#### Expansion Flow Field

The plasma and reactants pass from the reaction channel into an expansion chamber evacuated by 141.5 l/sec vacuum pump. For an argon mass flow of 0.22 g/sec, and a discharge pressure of 165 Torr, the pressure in the expansion chamber is 0.26 Torr. The channel pressure is maintained at approximately 87 Torr. These were the conditions at which most of the present plasma chemistry experiments were performed. The expansion flow is a free jet for which the flow field has been substantially investigated<sup>29</sup>. For the above operating conditions the free jet expansion has a theoretical Mach disc location of 12.2 nozzle diameters (4.85 cm) downstream from the channel exit. However, this theoretical location is based on experimental verifications for a single component gas expansion. Thus for a plasma, the theoretical location of Mach disc is only indicative of a general distance near which the real Mach disc is likely to be present. In our experiment, a visual observation indicates a probable location for the Mach disc at 5.71 cm downstream from the channel exit. This is also the location for the extractor nozzle through which the plasma sampling is made.

As in the case of the Mach disc calculation, the thermodynamic, fluiddynamic and collision parameters in the free jet flow field have been calculated from the known correlations of single component gas free jet experiments (Fig. 9) due to the lack of established experimental correlations for a plasma free jet.

The calculated terminal Mach number is 14.26 and is located at  $X/D = 9.25$  on the free jet axis (Fig. 10a), indicating that there will be no interference from interparticle collisions at the extractor nozzle location at  $X/D = 14.4$ . In the

### Figure 9 Expansion Flow Field

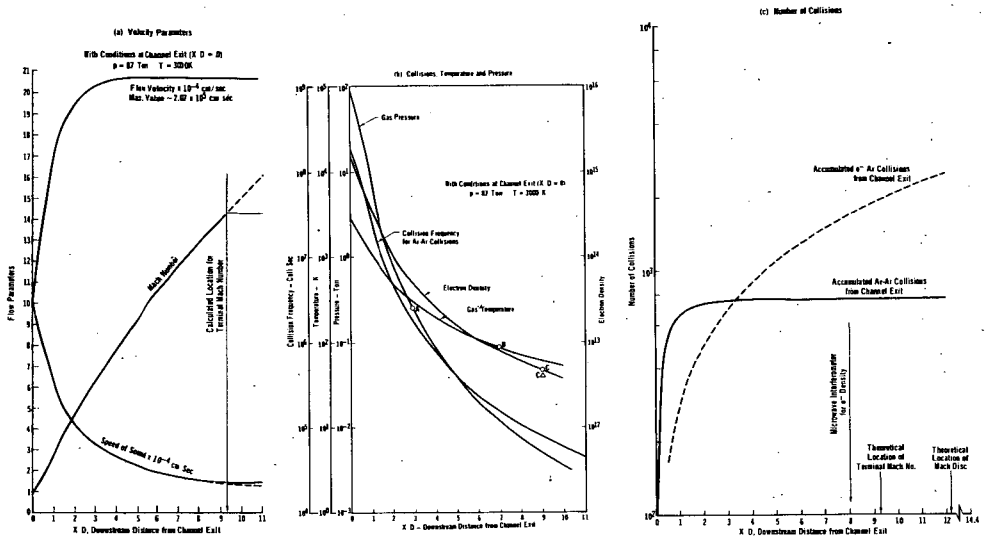
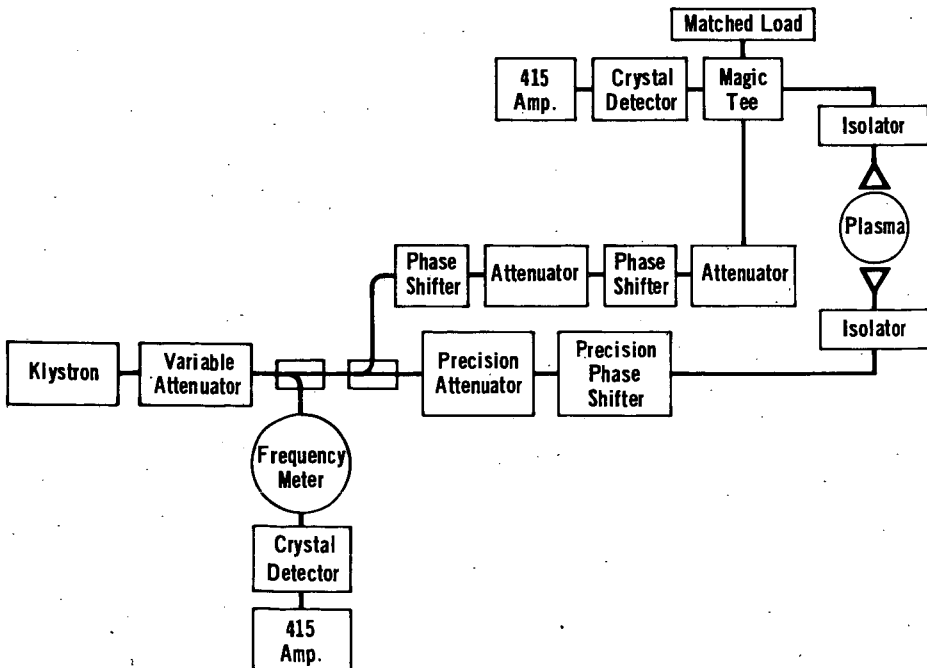


### Figure 10 Ka-Band Microwave Interferometer



free jet before the terminal Mach number, the flow field is a collision dominated laminar flow closely described by isentropic relations. Calculations indicate that the environmental pressure level (0.26 Torr) is reached at  $X/D \approx 3$  (Pt. A in Fig. 10b). Penetrations of the background gas molecules are present further downstream; however, because of the low collision frequency, the presence of the background gas in this part of the free jet is not expected to cause significant change to the composition sampled at the extractor nozzle by the mass spectrometer.

The temperature of the argon in the free jet reaches the freezing point of  $\approx 87^\circ\text{K}$  at  $X/D \approx 7$  (pt. B in Fig. 10b). Thus, argon dimers may be formed. However, the collisions between argon atoms become so few that the chance of dimer formation is greatly reduced. The electron density curve in Fig. 10b is also calculated using isentropic relations with  $\gamma = 5/3$ . Based on the spectroscopically measured excitation temperature ( $8500^\circ\text{K}$ ) in the discharge chamber and subsequent correlation in the sonic reaction channel, the electron density at the channel exit is  $\approx 1.7 \times 10^{15} \text{ e/cm}^3$  and is calculated to be  $\approx 4.8 \times 10^{12} \text{ e/cm}^3$  at  $X/D \approx 9$  (pt. C in Fig. 10b) where the electron density measured by the microwave interferometer is  $4.2 \times 10^{12} \text{ e/cm}^3$  (pt. C' in Fig. 10b).

The interparticle collisions in the free jet are an important factor in correlating the data sampled at the extractor nozzle position downstream ( $X/D = 14.4$ ) with the composition at the channel exit. The extent to which the plasma composition may be altered in the free jet depends on the accumulated number of collisions from the channel exit downward to the extractor nozzle. For Ar-Ar collisions (Fig. 10c), and most of the collision between argon and neutral reaction products, the accumulated number of collisions rises rapidly in the first nozzle diameter distance with little increase further downstream. The total number of the thermal collisions is estimated at  $\approx 700$ , sufficient to cause rotational and vibrational transitions, but not numerous enough to cause much excitation or ionization of the Ar atom or dissociation of reaction products. Also shown in Fig. 10c is the accumulated e - Ar collisions from the channel exit. The number of collisions are calculated from the established cross sections for low energy e - Ar interactions<sup>30</sup>. The accumulated number of e - Ar collisions indicates an increasing trend reflecting a fairly constant collision frequency due to the Ramsauer-Townsend effect. For the conditions of this experiment it is reasonable to assume that the collision frequency between electrons and neutral reaction products is nearly the same as the e - Ar collision frequency. This means that electron attachment reactions may occur in the free jet. However, the electron density is reduced by two orders of magnitude because of isentropic expansion and consequently the attachment contribution in the free jet should be small compared with that in the reaction channel. In any case, to remove any doubt, electron attachment or electron ionization measurements should be performed using two channel lengths so it can be shown that the reactions are indeed occurring in the channel.

#### Microwave Interferometer Measurements of Electron Densities

An important parameter necessary to evaluate electron target molecule reactions is the electron density. Electron densities are measured with a Ka-band (27-40 GHz) microwave interferometer<sup>31</sup> in the free jet region 2.5 cm from the exit plane as shown in Fig. 10. Open ended waveguides are used for antennas and are located so that the plasma is just outside of the antenna near field. An isolator is used behind the transmitting antenna to prevent reflections due to plasma scattering from entering the system. An additional isolator is placed behind the receiving antenna so the crystal detector behind the magic tee can be tuned to the incident received signal only and thus avoid reactive tuning due to the plasma path length. Precision phase shifters and attenuators are used throughout the circuit to obtain maximum accuracy and sensitivity.

The electron density and electron-neutral collision frequency are evaluated by relating the measured phase shift and attenuation due to the plasma to that predicted from a plane wave analysis assuming a parabolic electron density profile for a given diameter shown in Fig. 11. This system is capable of measuring electron densities from  $2 \times 10^{10}$  to  $1 \times 10^{13}$  e/cm<sup>3</sup>. Figure 12 shows the measured electron density as a function of rf generator power for various argon mass flow rates. Because the plasma is underdense, the electron-ion collision frequency is small compared to the interferometer signal frequency, no appreciable attenuation occurs. The measured electron densities in the free jet can be related to the electron densities in the channel as described in the preceding section. The electron density at the exit plane of the free jet at a mass flow of 0.22 g/sec and 57 kW of rf power was shown to be approximately 354 times higher than that measured 2.5 cm further downstream.

### Mass Sampling System

The ion sampling system is shown schematically in Fig. 13. The center core flow of the expanded plasma plus target gas reaction products is sampled with a specially designed conical extractor nozzle. The cone angles of the extractor minimize boundary layer effects near the orifice and prevent gas particles from being scattered back into the expansion plume. The extractor is conduction cooled by water cooling its mounting flange. The extractor tip is located in the expansion region between the location of the transition zone and the Mach disc and contains a 250  $\mu$ m orifice through which the plasma is sampled. Mass analysis of the sampled plasma is achieved with a commercial quadrupole analyzer and ionizer (EAI 150A) located behind the extractor nozzle. Ion currents from the analyzer are collected with a Faraday cage and measured with an electrometer. Biasing on the input electrodes to the quadrupole and the Faraday cage is adjusted to optimize the positive or negative ion signal. Neutral species detection is accomplished by activating the internal filament and biasing supplies of the quadrupole control unit. Background pressures in the system during normal operation are 0.26 Torr in the expansion region and about  $2 \times 10^{-6}$  Torr in the analysis region. A sample of positive and negative ion data using SF<sub>6</sub> target molecules is shown in Fig. 14.

### Interpretation of Experimental Measurements

Chemical rates for various kinds of reactions can often be evaluated by the use of a forward rate dominated model. For a forward dominated 2nd order process, the rate constant at temperature T is given by

$$K(T) = \frac{1}{t(n-N_0)} \ln \left[ \frac{N_0[N(t) + n-N_0]}{n N(t)} \right]$$

where  $N_0$  = initial reactant number density,  
 $N(t)$  = reactant number density after reacting time t, and  
 $n$  = target molecule number density.

This forward rate dominated model assumes that the reactant number density depletion is due solely to the reaction of interest. If more than one new species are observed by the mass spectrometer, care must be exercised in using this model and in general the measured reaction rate will be an average for all the reactions observed.

Reactions involving the plasma free electrons are often of major interest in the study of plasma chemistry. In this case  $N_0$  becomes the initial electron number density and  $N(t)$  is the electron number density after reacting for time t;  $K(T)$  is



Figure 11 Electron Density (N) - Collision Frequency (V) Contour Plot

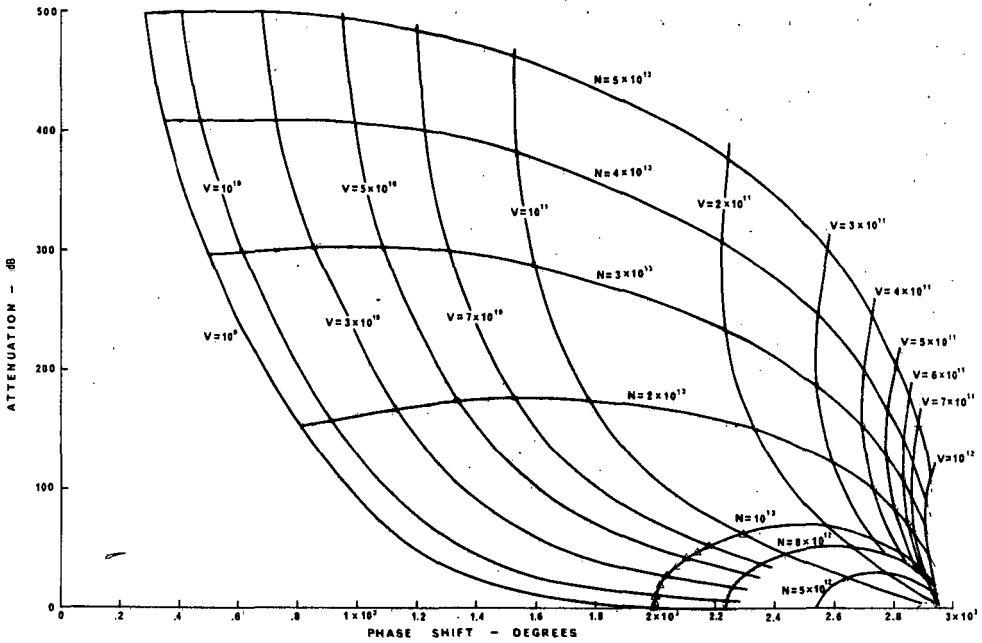
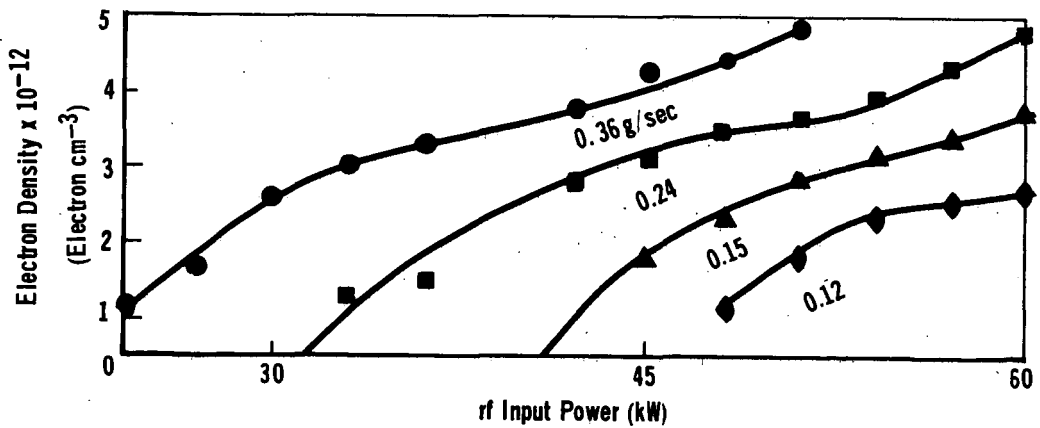
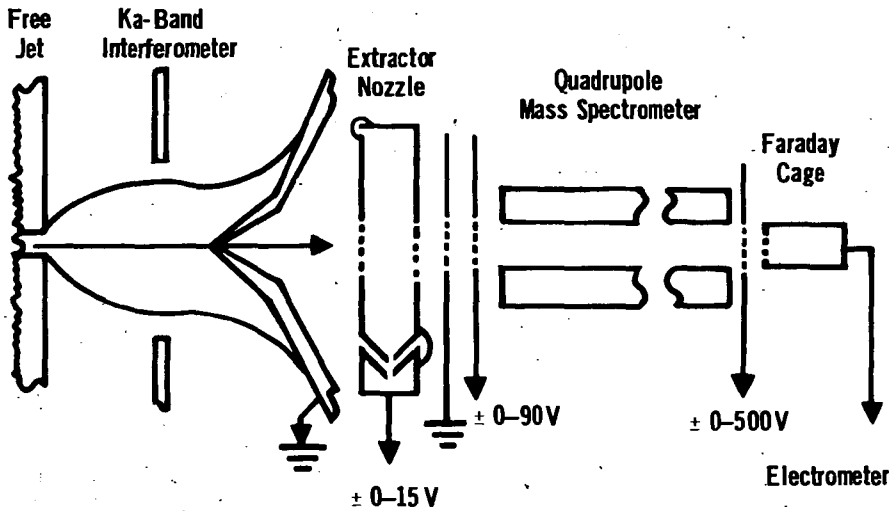


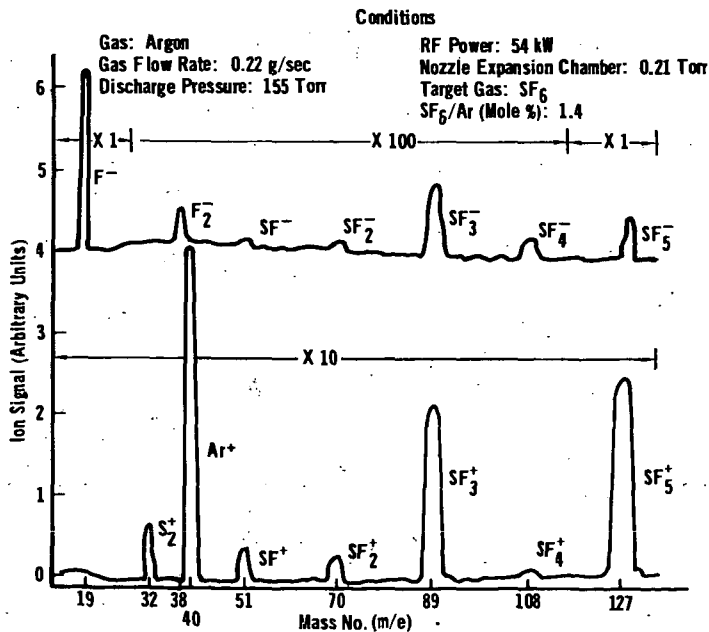
Figure 12 Measured Electron Densities



**Figure 13 Schematic of Ion Sampling Systems**



**Figure 14 SF<sub>6</sub> Positive and Negative Ion Spectrum**



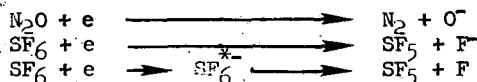
evaluated from the preceding equation. Therefore, this measurement technique provides a method for obtaining electron reaction rate constants at readily controllable temperatures. This rate constant can be compared to the theoretically predicted electron reaction cross sections  $\sigma(T, E)^{32}$  by

$$K(T) = \frac{1}{m_e} \int_0^{\infty} \sigma(T, E) f(E) dE,$$

where  $f(E)$  = electron energy distribution, and  
 $m_e$  = electron mass.

Since many investigators have found that the electron dissociative attachment cross section for some target molecules increases significantly with the target molecule temperature<sup>1,2</sup>, the experimental apparatus described in this paper will extend these measurements to higher temperatures.

As an example, the dissociative attachment rate constant for



are evaluated at 3000°K. Electron temperatures for the experiment are assumed to be equal to the Ar excitation temperatures measured spectroscopically. Electron densities measured with the microwave interferometer and negative ion densities measured with the mass spectrometer are shown in Figs. 15 and 16. Note that for N<sub>2</sub>O the rate of decrease of electron density approximately equals the rate of increase of negative ions. Since the plasma is less than 1% ionized the target molecule number density is usually much greater than the electron number density (i.e.  $n \gg N_0$ ) and the equation for the second order rate reduces to

$$K(T) = \frac{1}{nt} \ln \frac{N_0}{N(t)}$$

From a plot of  $\ln N_0/N(t)$  as a function of  $n$ ,  $t$   $K(T)$  is evaluated.

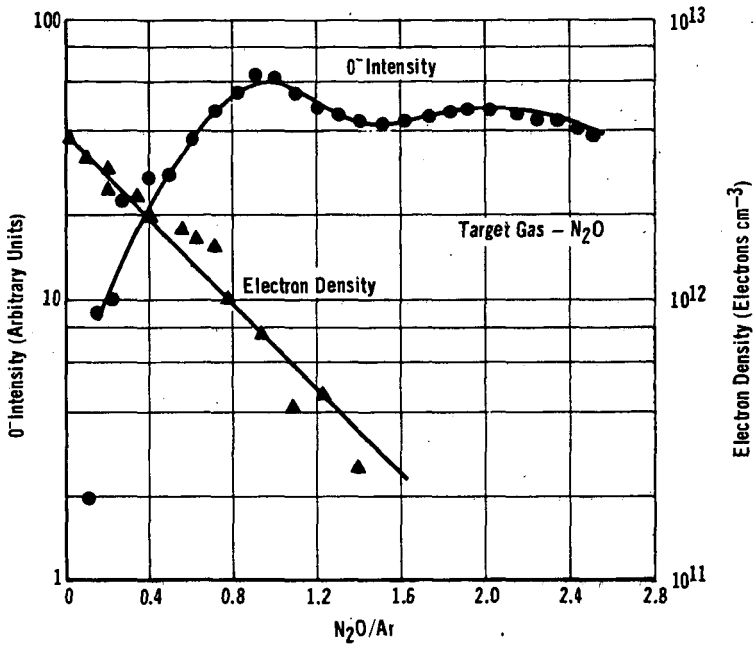
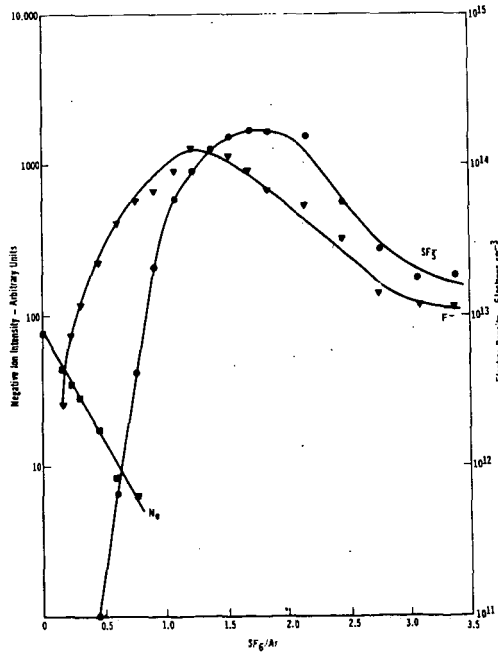
The initial rate of increase of the  $\text{F}^-$  and  $\text{SF}_5^-$  is used to evaluate the rate constants when using  $\text{SF}_6$  as a target gas. Initial slopes are usually used to evaluate the forward reaction rates because so few reaction products are formed at the low target gas mole fractions and consequently no appreciable reverse reactions appear. Measured reaction rates for various electrophilic target molecules are shown in Table III for a gas temperature of 3000°K.

## Conclusions

A system has been developed for the measurement of chemical kinetics in high temperature plasmas. Plasma temperatures and electron densities have been measured in the reaction region. Reaction temperatures from 1000 to 3000°K have been attained. Direct measurements of reaction products including both positive and negative ion species and free electrons have been achieved. Electron attachment rate constants for several electrophilic target molecules have been calculated from the negative ion signals at a reaction temperature of 3000°K. Additional experimental attachment studies will be necessary to extend the measured attachment rates over a broad temperature range for comparison with data obtained by other investigators. Preliminary

Table III Measured Reaction Rates ( $T_g = 3000K$ )

Probable Reaction	Estimated Rate $\times 10^{11}$ ( $\text{cm}^3/\text{part. sec.}$ )	Determined from
$\text{Ar}^+ + \text{H}_2 \longrightarrow \text{ArH}^+ + \text{H}$	6.3	$\text{Ar}^+$ Decay
$\text{e} + \text{N}_2\text{O} \longrightarrow \text{O}^- + \text{N}_2$	18	$\text{O}^-$ Increase
$\text{e} + \text{Br}_2 \longrightarrow \text{Br}^- + \text{Br}$	13	$\text{Br}^-$ Increase
$\text{e} + \text{SF}_6 \longrightarrow \text{F}^- + \text{SF}_5$	142	$\text{F}^-$ Increase
$\text{e} + \text{SF}_6 \longrightarrow \text{SF}_6^{*-} \longrightarrow \text{SF}_5 + \text{F}$	140	$\text{SF}_5^-$ Increase

Figure 15 Electron Density and  $O^-$  IntensityFigure 16 Negative Ion Intensity and Electron Density Using  $SF_6$  Target Molecules

results indicate that the electron attachment rates measured at 3000°K can differ significantly from those measured at lower temperatures.

#### Acknowledgment

The authors are indebted to Dr. R. A. Hefferlin for the optical spectrographic measurements of the source and reaction channel excitation temperatures and the electron density in the source.

#### References

1. P. J. Chantry, *J. Chem. Phys.* 51, 3369 (1969).
2. W. L. Fite and R. T. Brackman, Proceedings of the Sixth International Conference on the Ionization Phenomena in Gases (SERMA, Paris, 1963) Vol. 1, p. 21. W. L. Fite, R. T. Brackman and W. R. Henderson, Proceedings of the Fourth International Conference on the Physics of Electronic and Atomic Collisions (Science Bookcrafters, Inc., Hastings-on-Hudson, New York), p. 100.
3. W. R. Henderson, W. L. Fite and R. T. Brackman, *Phys. Rev.* 183, 157 (1969).
4. F. C. Fehsenfeld, A. L. Schmeltekopf, P. D. Goldan, H. I. Schiff and E. E. Ferguson, *J. Chem. Phys.* 44, 4087 (1966).
5. D. B. Dunkin, F. C. Fehsenfeld, A. L. Schmeltekopf and E. E. Ferguson, *J. Chem. Phys.* 49, 1365 (1968).
6. K. E. Starner, "Evaluation of Electron Quench Additives in a Subsonic Air Arc Channel," Aerospace Report TR-0200 (4240-10)-2 September 1968.
7. S. Atallah, W. A. Sanborn, A. Hoodbhoy, "The Effect of Chemical Additives on the Electron Density of Plasma Jets," AFRL 66-5, December 1965.
8. S. Aisenberg, "The Use of Chemical Additives for the Alleviation of the Plasma Sheath Problem," *Proceedings of the Conference on the Applications of Plasma Studies to Reentry Vehicle Communications, Vol. 1, (1967).*
9. J. H. Mullen, R. L. Cowperthwaite, and T. C. Peng, Twenty-Second Annual Gaseous Electronics Conference, Gatlinburg, Tennessee (1969), *Bull. Am. Phys. Soc.*, 51 3369 (1969).
10. T. B. Reed, *J. Appl. Phys.* 32, 821 (1961).
11. H. V. Eckert, F. L. Kelly and H. N. Olsen, *J. Appl. Phys.* 39, 1846 (1968).
12. R. Hefferlin, Progress in High Temperature Physics and Chemistry, (Pergamon Press, New York, 1969), Vol. 3, Chap. 2.
13. G. V. Marr, Plasma Spectroscopy (Elsevier, London, 1968).
14. W. Lochte-Holtgreven, Plasma Diagnostics, (North Holland Publishing Co., John Wiley & Sons, New York, 1968), Chap. 3.
15. G. Bekefi, Radiation Processes in Plasmas, (John Wiley, New York, 1966) Chap. 2.
16. R. H. Dicke, *Rev. Sci. Instr.* 17, 268 (1946).

17. D. B. Harris, *Microwave Journal*, 3, 41, 47 (1960).
18. P. D. Strum, *PROC. IRE*, 48, 43 (1958).
19. J. S. Hey and V. A. Hughes, *PROC. IRE*, 48, 119 (1958).
20. G. G. Haroules and W. E. Brown III, *Rev. Sci. Instr.*, 38, 1043 (1967).
21. E. A. Ohm and W. W. Snell, *Bell System Tech. J.*, 42, 2047 (1963).
22. J. P. Appleton and K. N. C. Bray, *Fluid Mech.*, Part 4, 659 (1964).
23. S. C. Brown, Basic Data of Plasma Physics, (MIT Press, 1959), Chapter 1.
24. H. Schlichting, Boundary Layer Theory, (McGraw-Hill, 4th Ed. 1960), p. 35-36.
25. *Ibid*, p. 257.
26. G. N. Abramovich, Theory of Turbulent Jets, (MIT Press, Cambridge, Mass., 1963), p. 543.
27. *Ibid*, p. 544.
28. S. Crist, P. M. Sherman, D. R. Glass, *AIAA J.*, 4, 58 (1966).
29. J. B. French, *AIAA J.* 3, 993 (1965).
30. G. Francis, Ionization Phenomena in Gases, (Butterworth Scientific Publications, 1960), Chap. 2, p. 19.
31. M. A. Heald and C. B. Wharton, Plasma Diagnostics with Microwaves, (John Wiley, New York, 1965), Chap. 6 and 9.
32. T. F. O'Malley, *Phys. Rev.* 155, 59 (1967).

PRESSURE EFFECT ON PRODUCT SELECTIVITIES IN THE PYROLYSIS  
OF METHANE IN AN ARC-PLASMA HEATER

C. Hirayama  
M. G. Fey  
F. E. Camp

Westinghouse Research Laboratories  
Pittsburgh, Pennsylvania 15235

## INTRODUCTION

There have been a number of electric arc processes reported for the conversion of hydrocarbons to acetylene and associated products. To date, only two of these processes have been adapted to commercial scale production of acetylene. 1) The original Huels flaming-arc process<sup>1</sup> in Germany pyrolyzed a hydrocarbon feed stock in a direct current arc. The gas was introduced into the heater in a swirling pattern so as to aid in rotating the arc. A heavy hydrocarbon was also injected downstream of the heater nozzle as the initial quench. More recently, the feed stock hydrocarbon has been injected into a hot hydrogen plasma<sup>2</sup> in order to reduce the carbon content in the product. 2) The DuPont process<sup>3</sup> (presently not in use<sup>4</sup>) utilized a direct current arc similar to Huels', but with a magnetic rotation of the arc. In this process, the plenum was maintained below atmospheric pressure. The Huels process, although not so stated in the published literature, presumably cracked the hydrocarbon at atmospheric (or higher) pressure. Unless there is use for the carbon from these pyrolysis processes, it is imperative that the soot content in the product be minimized.

For most practical plant practice, it is desirable that the pressure of the product gas from the heater be as high as possible. This would minimize the compression necessary for efficient absorption of acetylene from the cracked gas in the separation plant. It is known that higher pressure in the cracking chamber tends to yield higher carbon; conversely, lower pressure reduces the carbon yield. For example, the DuPont process, which reportedly operated at 400 torr in the plenum, yielded only about three percent of carbon, whereas the earlier Huels process yielded approximately twenty percent carbon.

We here report the effect on acetylene selectivity of pressures between one and seven atmospheres in the electric-arc heater reaction chamber when methane is pyrolyzed.

## EXPERIMENTAL

The electric-arc heater of 3000 kilowatts has been described previously.<sup>5</sup> However, for the present experiments, the heater was operated in the self-stabilizing, high-flow mode on a.c. power, as described by Fey.<sup>6</sup> Suffice it to report here that the chemical data obtained on the present arc heater and that reported by Fey are similar.

### Test Conditions

Methane of C.P. grade (98.6% CH<sub>4</sub>, 0.2% C<sub>2</sub>H<sub>6</sub>, 1.1% N<sub>2</sub>, 0.1% O<sub>2</sub>) was delivered to the heater from a pressurized tube-trailer, and was metered through a critical flow orifice. The gas was introduced to the heater at room temperature. The residence volume of the heater chamber was 0.6 ft.<sup>3</sup>.



The gas samples at the heater nozzle were collected as previously described<sup>5</sup> with a water cooled copper probe of 1/8 inch i.d. A carbon filter (Purolator part #51383 fiber filter fitted into a glass vessel) was inserted before the sample manifold. The chemical analyses of the product gas were obtained by mass spectrometry.

During a run, the power level was varied over several steps by changing the gas flow rate and/or by changing the arc power. A product gas sample at each step was collected after the desired arc power level became stabilized. The electrical, flow and pressure data were continuously recorded on a Honeywell Model 1612 visicorder.

The pressure in the arc chamber was controlled by an 8" long cylindrical graphite insert fitted into the heater nozzle. Different pressure levels were obtained by inserts of different orifice diameters and by varying the gas flow rate. The orifice diameter varied from 1.06 to 3.00 inches. The heater chamber pressure was measured by inserting a calibrated transducer into the end-plug of the heater.

## RESULTS

Table I summarizes typical operational characteristics of the arc heater. The arc power level varied from 1 to 2.5 megawatts, with a thermal efficiency approaching 90%. The methane mass flow rate was as high as 0.78 lbs/sec, and the enthalpy of the gas varied from approximately 1300 to 4000 Btu/lb. The pressure in the heater chamber varied from atmospheric to 87.9 psig.

Table II summarizes the molar composition of the product at conditions corresponding to the operations shown in Table I. The material balance was made on the basis of the C/H ratios of the feed and of the product gas. The results in Table II are slightly in error since a small amount of the product was adsorbed on the trapped carbon in the filter. This was evidenced by an aromatic odor of the carbon sample. However, this error is less than five percent, as shown by a separate test in which the feed gas was doped with 2% argon as a material balance probe.

The concentration of acetylene, C, in the product was fitted to various functions,  $f(P/H)$ , where P is the heater chamber pressure in atmospheres, and H the enthalpy, in Btu/lb, into the feed stock. The best linear correlation obtained was of the form  $\log C = A - B\sqrt{P/H}$ , where A and B are constants. Figure 1 shows the plot for all of the data. The scatter in the data was greater at high  $\sqrt{P/H}$ .

Table III shows the overall conversion (percent reaction) of the methane in the first column. As shown in Figure 2 for all of the collected data at atmospheric and for higher pressures in this experiment, the conversion increases almost linearly with the enthalpy.

Table III also shows the carbon material balance in columns 2 to 10. Note the relatively large amount of methane in the product. The last column in this table shows the specific energy requirement (SER) for acetylene production under the conditions reported herein. At atmospheric pressure, runs 1 to 3, the SER remains approximately constant, around 4.0 kwh/lb  $C_2H_2$ , at enthalpies of 2100 to 3650 Btu/lb. At pressures between 4 and 22 psig the SER's are below 5 kwh/lb  $C_2H_2$ . The acetylene concentrations in these instances (runs 4 to 8),

Table I. Heater Operating Characteristics

Run No.	Arc Power KW	Mass Flow Rate, lbs/sec	Heater Efficiency %	Enthalpy Btu/lb	Heater Pressure psig
1	1598	0.565	77.5	2100	0
2	1440	0.344	73.1	2900	0
3	1860	0.345	73.2	3650	0
4	1527	0.437	83.4	2760	3.8
5	1411	0.522	83.7	2140	5.7
6	1066	0.623	80.0	1297	13.4
7	1585	0.480	83.8	2620	15.3
8	1670	0.780	85.4	1735	21.6
9	1583	0.441	83.8	2850	22.3
10	2380	0.531	86.1	3660	33.8
11	2290	0.565	85.0	3270	35.0
12	2420	0.627	88.6	3170	44.5
13	1960	0.642	86.4	2500	56.0
14	1612	0.524	86.1	2510	69.5
15	1960	0.608	86.6	2642	87.9

Table II. Molar Composition of Product

Run. No.	$\text{CH}_4$	$\text{H}_2$	Mole %						$\text{C}_6\text{H}_6$	C
			$\text{C}_2\text{H}_2$	$\text{C}_2\text{H}_4$	$\text{C}_2\text{H}_6$	$\text{C}_3\text{H}_4$	$\text{C}_3\text{H}_8$	$\text{C}_4\text{H}_2$		
1	55.3	33.5	8.2	0.33	0.11	0.26	0.01	0.42	0.04	1.8
2	35.1	48.2	11.2	0.54	0.06	0.31	0.02	0.45	0.10	4.0
3	22.8	56.5	11.8	0.56	0.03	0.23	0.02	0.44	0.08	7.5
4	48.4	38.5	9.2	0.34	0.10	0.34	0.03	0.46	0.05	2.5
5	61.9	28.5	6.8	0.29	0.10	0.27	0.04	0.36	0.04	1.7
6	69.6	22.6	5.3	0.30	0.10	0.18	0.02	0.26	0.04	1.6
7	46.9	38.9	7.8	0.56	0.08	0.24	0.02	0.3	0.08	5.1
8	63.6	26.9	6.0	0.41	0.11	0.23	0.02	0.25	0.05	2.5
9	51.1	35.8	7.2	0.68	0.08	0.25	0.02	0.26	0.10	4.4
10	33.0	48.2	8.0	0.86	0.05	0.23	0.03	0.24	0.12	9.2
11	39.4	43.7	7.1	0.94	0.06	0.23	0.02	0.22	0.14	8.2
12	32.9	48.0	7.5	0.84	0.05	0.21	0.03	0.22	0.11	10.1
13	51.8	34.4	4.8	1.0	0.10	0.19	0.03	0.13	0.14	7.4
14	73.2	19.0	2.2	0.72	0.10	0.11	0.02	0.05	0.11	4.4
15	49.6	35.5	3.4	1.4	0.10	0.16	0.03	0.06	0.17	9.6

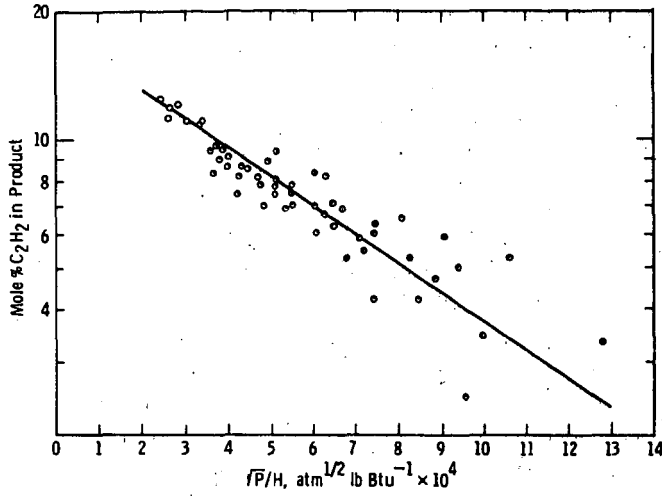


Fig. 1—Product acetylene concentration as a function of  $\sqrt{P}/H$

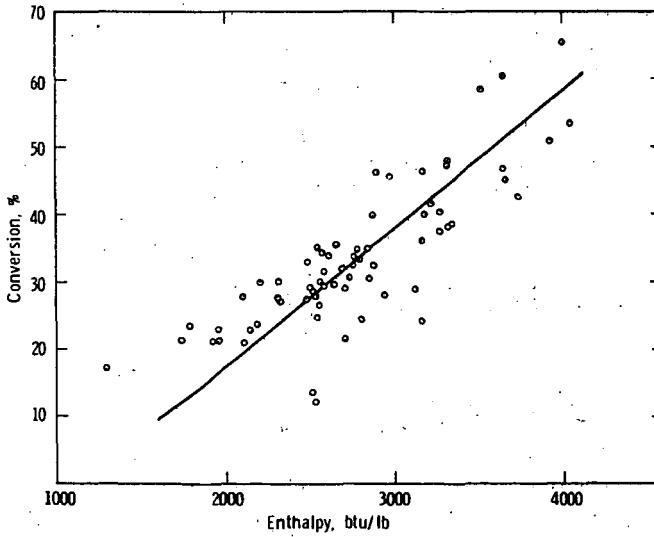


Fig. 2—Conversion of methane as a function of enthalpy

Table III. Conversion, Carbon Material Balance  
(Conversion to Carbon Products) and SER

Run No.	Conversion %	Conversion to Carbon Products, Mole %										C	SER kwh/lb C <sub>2</sub> H <sub>2</sub>
		CH <sub>4</sub>	C <sub>2</sub> H <sub>2</sub>	C <sub>2</sub> H <sub>4</sub>	C <sub>2</sub> H <sub>6</sub>	C <sub>3</sub> H <sub>4</sub>	C <sub>3</sub> H <sub>8</sub>	C <sub>4</sub> H <sub>2</sub>	C <sub>6</sub> H <sub>6</sub>				
1	28.1	71.6	21.4	0.86	0.30	1.0	0.04	2.2	0.30	2.3	4.1		
2	46.6	53.2	33.9	1.7	0.17	1.4	0.09	2.7	0.87	6.1	3.8		
3	60.5	39.3	40.7	1.9	0.10	1.2	0.10	3.0	0.86	12.8	4.0		
4	33.7	65.9	25.1	0.94	0.28	1.4	0.12	2.5	0.41	3.4	4.3		
5	22.8	76.8	17.0	0.71	0.25	1.0	0.15	1.8	0.30	2.1	4.9		
6	17.2	82.5	12.5	0.70	0.23	0.63	0.07	1.2	0.28	1.9	4.2		
7	34.0	65.7	21.9	1.6	0.21	1.0	0.08	1.7	0.72	7.1	4.6		
8	21.2	78.4	14.7	1.0	0.26	0.87	0.07	1.2	0.36	3.0	4.5		
9	30.5	69.2	19.5	1.8	0.21	1.0	0.08	1.4	0.85	6.0	5.7		
10	46.9	52.7	25.7	2.8	0.17	1.1	0.13	1.6	1.1	14.7	5.4		
11	40.3	59.5	21.5	2.8	0.20	1.0	0.08	1.3	1.2	12.3	5.8		
12	46.6	53.1	24.3	2.7	0.17	1.0	0.13	1.4	1.0	16.2	4.9		
13	28.6	71.0	13.0	2.8	0.25	0.80	0.11	0.71	1.1	10.2	7.2		
14	13.5	86.1	5.2	1.7	0.25	0.40	0.07	0.22	0.81	5.2	18		
15	29.7	69.9	9.7	4.0	0.28	0.70	0.11	0.36	1.5	13.5	10		

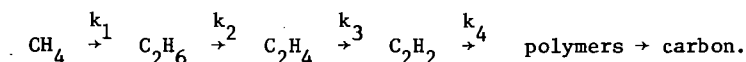
however, are low because of the low enthalpies. At higher pressures, the SER increases as a result of increasing carbon yield.

Table IV shows typical selectivity (yield) values, arranged in the order of increasing pressure in the heater chamber. (These values are obtained from Table III by dividing the respective quantities in columns 3 to 10 by the quantity in the first column. The selectivities are actually low since the conversions are higher than calculated on the basis of the C/H ratio (see below)). Runs 1 to 3 show the effect of increasing temperature on the selectivities at atmospheric pressure. There is a significant increase in carbon yield as the pyrolysis temperature increases. As the pressure increases, there is a trend toward decreasing acetylene and diacetylene, while the ethylene, benzene and carbon yields tend to increase. The methylacetylene yield remains nearly constant with pressure. Figure 3 shows the correlations between the acetylene and carbon selectivities with pressure. Note that the pressure has been corrected to psia in this figure. The scatter of the data points arises in part from the variation of enthalpy encountered in these runs. The acetylene selectivity is best fitted with a linear correlation,  $S = 79 - 0.44 P$ , where  $S$  is the selectivity (in mole percent) and  $P$  the absolute pressure (psia). The carbon selectivity is a non-linear function of the pressure.

## DISCUSSION

In an electric arc process, the acetylene is formed from the hydrocarbon primarily at the high temperature around the arc column. The product is then rapidly quenched as it mixes with more feed gas. At the high flow rates reported here, the acetylene is more or less frozen as it is swept out of the heater. Within the heater chamber, however, the acetylene could polymerize. In the heater, there are regions of very high temperature where local thermodynamic equilibrium exists. Consequently, solid carbon will always be a product. It is well to remember, however, that cracking of a gas in an electric arc heater is considerably more complicated than that in an isothermal system at the same enthalpy. There is considerable local temperature inhomogeneity in an electric arc system.

The conversion of methane to acetylene and to ultimate products is generally believed to follow a path<sup>7</sup>:



The ratio of  $[\text{C}_2\text{H}_6]$  to  $[\text{CH}_4]$  is very small, because of the large  $k_2$ , so that ethane is often not detected in the pyrolysis product from methane. The ethylene is converted to acetylene by a monomolecular process,<sup>8</sup> whereas the acetylene is polymerized to its product by a bimolecular process.<sup>9</sup> One of the polymerization products of acetylene is diacetylene, which decomposes in a manner very similar to acetylene.<sup>10</sup> The diacetylene further polymerizes to ultimately yield carbon. At temperatures above 1000°C, all of these reactions are very rapid.

It is not surprising that both the acetylene and diacetylene selectivities decrease with increasing pressure since the decompositions of both compounds are similar bimolecular processes whose rates of reaction vary as the square of the pressure.<sup>11</sup> It is apparent from the data in Table IV that the acetylene decomposition is much more sensitive to increasing pressure than is the monomolecular reaction by which the acetylene is formed from ethylene. The latter reaction rate varies only as the first power of the pressure. The increase in

Table IV. Selectivity of Products in Mole % and Heater Chamber Pressure

Run No.	SELECTIVITY					C	Pressure, psig
	$C_2H_2$	$C_2H_4$	$C_3H_4$	$C_4H_2$	$C_6H_6$		
1	76.1	3.1	3.6	7.8	1.1	8.2	0
2	72.5	3.6	3.0	5.8	1.9	13.1	0
3	67.2	3.1	2.0	5.0	1.4	21.1	0
4	74.5	2.8	4.2	7.4	1.2	10.1	3.8
5	74.5	3.1	4.4	7.9	1.3	9.2	5.7
6	72.6	4.1	3.7	7.0	1.6	11.0	13.4
7	64.5	4.7	2.9	5.0	2.1	20.8	15.3
8	69.3	4.7	4.1	5.7	1.7	14.2	21.6
9	64.0	5.9	3.3	4.6	2.8	19.7	22.3
10	54.8	6.0	2.3	3.4	2.3	31.3	33.8
11	53.3	7.0	2.5	3.2	3.0	30.5	35.0
12	52.1	5.8	2.1	3.0	2.1	34.7	44.5
13	45.5	9.8	2.8	2.5	3.8	35.7	56.0
14	38.5	12.6	3.0	1.6	6.0	38.5	69.5
15	32.8	13.5	2.4	1.2	5.0	45.5	87.9

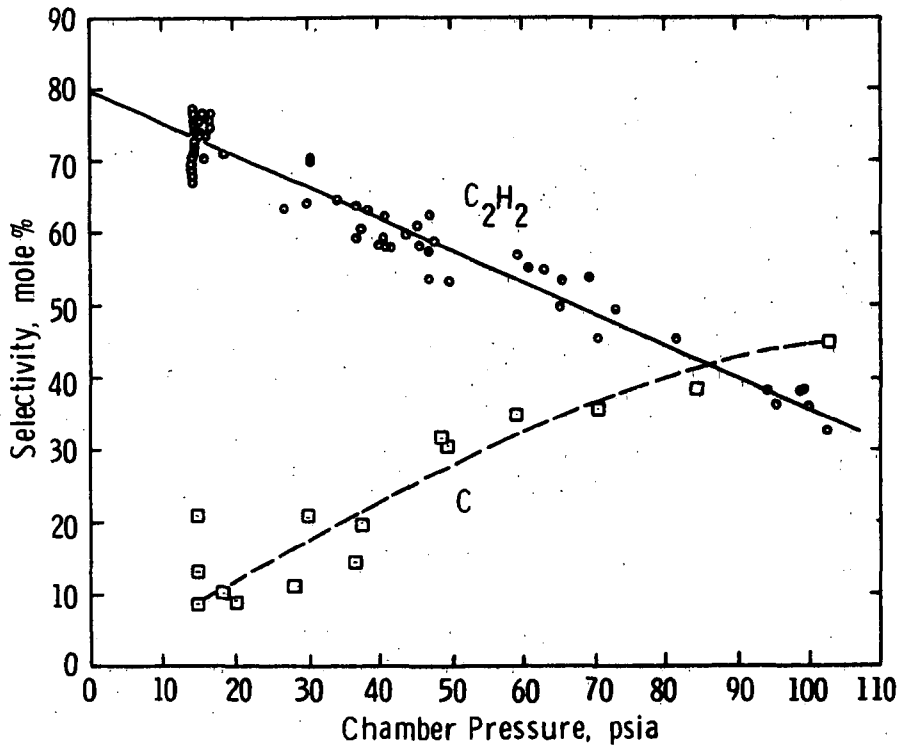


Fig. 3—Acetylene and carbon selectivity as function of chamber pressure



carbon yield with pressure is to be expected since this is the ultimate decomposition product from acetylene, and there is a significant decrease in the  $C_2H_2$  with pressure. The increase in benzene yield with pressure is consistent with the mechanism suggested by Cullis and Franklin<sup>12</sup> for the formation of this species. All of the variations in yield with pressure are in qualitative agreement with the kinetic results reported by the above authors.

The relationship between the acetylene concentration and the enthalpy, as shown in Figure 1, is consistent with the Arrhenius law. However, the exact significance of the correlation between the acetylene concentration and  $\sqrt{P}$  is not known. The kinetics of the competing reactions for the formation and decomposition of acetylene at increasing pressures is obviously complex. Nevertheless, the trend of decreasing acetylene with increasing pressure is in qualitative agreement with the kinetics of acetylene decomposition.

Methane is one of the decomposition products of acetylene<sup>10,12</sup> and can become a significant product. Therefore, the actual conversion is higher than that calculated from the C/H ratio. Especially at high pressure and low acetylene selectivity does the contribution of regenerated methane become significant in the overall product concentrations. Unfortunately, the exact amount of regenerated methane is not known, so that the overall conversion cannot be corrected.

For a viable acetylene process it is apparent that the pressure in the reaction zone should be as low as practical in order to increase the  $C_2H_2$  yield and to decrease the soot content. On the other hand, if the carbon content can be economically reduced, for example by downstream injection of steam without seriously affecting the acetylene yield or by absorption in heavy oil, operation around atmospheric pressure would yield acetylene at about 4 kwh/lb  $C_2H_2$ . Should the carbon be a desired by-product, this electric arc process would become attractive.

## CONCLUSION

The acetylene selectivity from the electric arc pyrolysis of methane decreases linearly with pressure. Consequently, the carbon yield is increased significantly as the pressure increases above one atmosphere.

## REFERENCES

1. H. Gladisch, *Hydroc. Proc. & Pet. Ref.* **41**, 159 (1962).
2. H. Gladisch, *Chem.-Ing. Tech.* **41**, 204 (1969).
3. R. A. Schulze, *Chem. & Ind.* **9**, 1539 (1968).
4. Anon., *Chem. Engineering*, May 20, 1968, p. 71.
5. C. Hirayama and D. A. Maniero, Preprints of papers presented, Div. of Fuel Chemistry, Am. Chem. Soc., Vol. 10, No. 1, pp. 123-132, March 1966.
6. Paper presented, Am. Chem. Soc., Fuel Chem. Div., Chicago, Sept. 1970.
7. e.g., S. A. Miller, "Acetylene, Its Properties, Manufacture and Uses," Vol. 1, Academic Press, New York, p. 373.
8. G. B. Skinner and E. M. Sokolski, *J. Phys. Chem.* **64**, 1028 (1960).
9. H. B. Palmer and F. L. Dormish, *J. Phys. Chem.* **68**, 1553 (1964).
10. K. C. Hou and H. B. Palmer, *J. Phys. Chem.* **69**, 863 (1965).
11. O. A. Hougen and K. M. Watson, "Chemical Process Principles," part 3, John Wiley & Sons, New York, 1947, pp. 832-839.
12. C. F. Cullis and N. H. Franklin, *Proc. Roy. Soc.* **1964**, 139.

## THE HEATING OF SOLIDS IN HIGH TEMPERATURE PLASMA

by

P. H. Wilks and M. L. Thorpe  
TAFI/IONARC  
Dow Road  
Bow (Concord), New Hampshire

### INTRODUCTION

Until recently, processing of solid particulate matter in plasma systems has been thermally inefficient, with systems capable of handling only small feed rates. The economic implications of this were overwhelming, and retarded the development of commercial scale plasma heating processes. The actual direct cost of energy was only a small part of the total cost. The major detriment lay in the high capital costs of energy conversion equipment which would be required for a thermally inefficient process.

Within the past two years we have culminated a 10 year effort and achieved a major upgrading of plasma generator solids heating capability. A pilot plant has been in operation for over two years, producing commercial quantities of materials, with processing capabilities over 1000 lbs/hr. and powder sizes up to 1000 microns. Power requirements have been dramatically reduced.

### SYSTEM PERFORMANCE

The TAFI/Ionarc plasma furnace, in operation since 1968, has achieved efficient heat affectation of solid particles on a large scale. We have found the most logical measure of particle heating performance to be the spheroidizing capability of the system. Performance measurement works as follows. The plasma system is turned on and adjusted to the desired power level, say 1000 kW. A 300 pound sample is then fed through the plasma column at a fixed rate. A series of tests are performed in this manner with all parameters except feed rate held constant. The particles are allowed to cool and solidify while

still in flight. The product is then collected, screened, and the various fractions run over the sphere separation table shown in Figure 1. These measurements give a complete picture relative to the heat affectation capability of the device operating under the test conditions. The spheroidization process is an automatic one; if the particles become molten, surface tension pulls them into a spherical shape. Melted particles below 150 microns are almost all spherical upon passing through a device. As the particle size increases above 150 microns, careful product analysis reveals a gradual increase in the number of egg shaped particles and non-perfect spheres in the product. This is undoubtedly caused by the large mass of the particle and the associated distortion forces as compared with the surface tension forces. If a feed stock below 150 microns is utilized, essentially 100 percent spheres are achieved under conditions adequate to melt all particles. Therefore, feed stocks in this size range are used when evaluating the spheroidizing capability. The performance measurement then is one of continually increasing the feed rate through the device in a series of tests and measuring the decreasing number of spheres formed. With such data it is easy to determine the minimum kWh/lb. of feed stock which achieves complete melting of all the particles. It has been observed that this is a reproducible number which can be compared with similar data generated with different feed injection techniques, power levels, apparatus geometries, feed stock size, feed stock composition, etc. Figure 2 shows zircon sand (zirconium silicate) which has been spheroidized. The illustration shows particles below 150 microns which have been processed at 1 kWh/lb. Note that they are all spherical. In Figure 3, the polished cross sections show that the spherical particles have been melted throughout. On the other hand, larger particles, such as the 300 micron particle shown in Figure 4, are not completely spherical. The center core has not been heated to  $1775^{\circ}\text{C}$ , which is the dissociation temperature of zircon.<sup>1</sup> This is clearly seen in Figure 4, where clear, glassy zircon can be seen in the center surrounded by a completely dissociated mixture of zirconium oxide and silica.

We feel that by this performance measurement technique we can accurately compare various plasma systems and their particle heating capability. We have been intensively active in this field since 1956 and have compared a variety of plasma torches using this technique. Typically, a conventional dc spray torch, shown in Figure 5, exemplifies the dc plasma torches used for particle heating. Powder is injected downstream of the arc foot point to prevent contamination of these areas. Much of the thermal impact of such a device is lost because the particles cannot be passed through the arc and thereby take advantage of the temperatures in this region, which are often twice that of the tailflame where particles are injected. It is recalled that the thermal radiation from hot gas is a function of the fourth power of the temperature; therefore, much

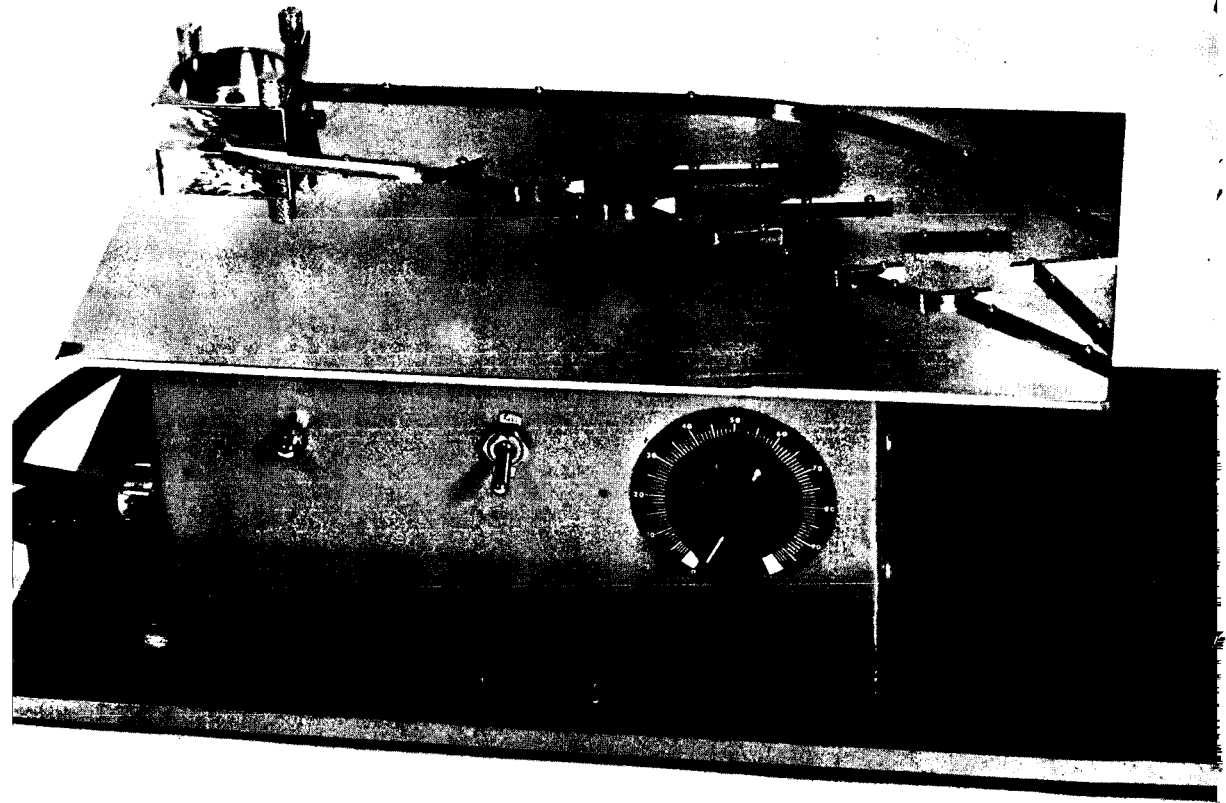


Figure 1. Table for Separating Spherical Powders

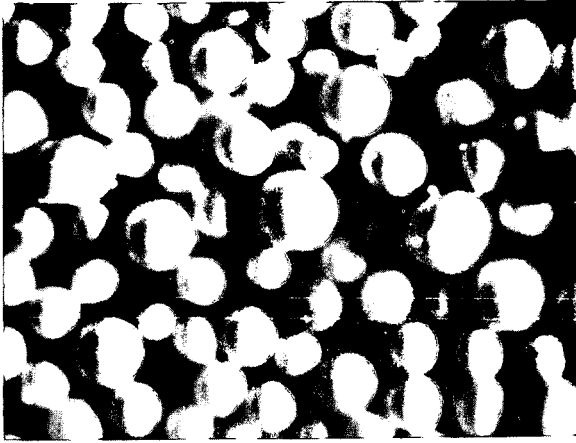


Figure 2. Typical Zircon Product As  
Removed from Furnace  
Without Upgrading.

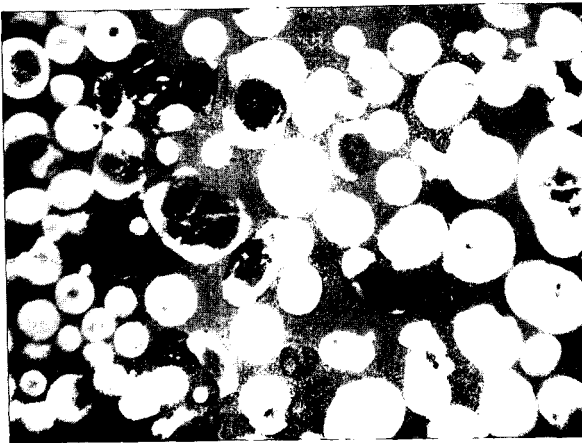


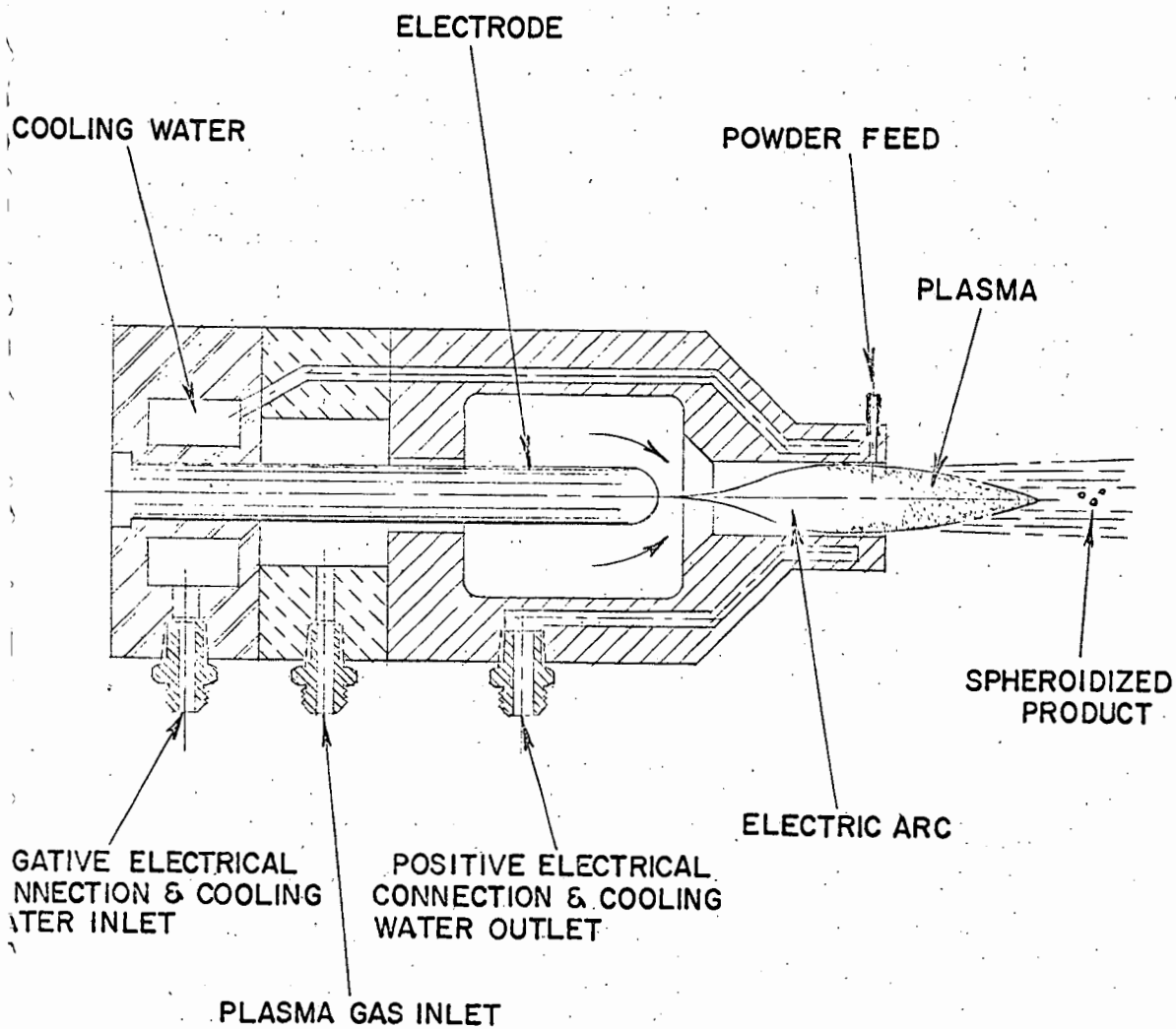
Figure 3. Typical Zircon Product  
Showing Degrees of  
Heat Affectation

Section in oblique, reflected light  
shows dissociated mixture (white)  
with cores of residual  $\text{ZrSiO}_4$  (gray,  
translucent).



Figure 4. Partially Dissociated 300 Micron Zircon Furnace Product

This particle, in partially polarized transmitted light, shows a core of residual  $\text{ZrSiO}_4$ , with rim of monoclinic  $\text{ZrO}_2$  (fibrous) and cubic  $\text{ZrO}_2$  (black). The reason for the black color of the cubic  $\text{ZrO}_2$  phase is explained by the exceedingly fine grained nature and the high index of refraction of cubic  $\text{ZrO}_2$  resulting in total reflection of the light. In reflected light this phase would be perfectly white. Note the sequence  $\text{ZrSiO}_4$ , monoclinic  $\text{ZrO}_2$ , cubic  $\text{ZrO}_2$ , indicating formation of monoclinic  $\text{ZrO}_2$  ahead of cubic  $\text{ZrO}_2$ .



CONVENTIONAL DC SPRAY TORCH

FIG.5

more particle heating capability is lost than is apparent from conductive heat transfer calculations. Our measurements would indicate radiant energy is the dominant factor in heating particles.

We therefore feel, on the basis of comparing the performance of a variety of devices, that we have achieved a dramatic improvement in solids handling capability with the plasma heater. This manifests itself in two ways; first, a much higher thermal efficiency (0.5 - 1.5 kWh/lb.) for such materials as zircon, ilmenite, aluminum oxide, and most metals. This is to be compared with energy requirements of 5 - 10 kWh/lb. which were typical of previously available devices. Secondly, we have achieved reliable scale up, which has permitted the design and operation of a reliable 1000 kW-1000 lb/hr. system, illustrated in Figure 6. This is to be compared with previous systems which operated in the 1-10 lb/hr. range and with which most investigators have worked. Units can be easily duplexed, and it would appear that further scale up will not be difficult. In fact, thermal efficiency seems to improve, as might be expected, as the scale of the apparatus is increased. Powder melting costs with such a device, including all operating costs, plant amortization, and labor are in the range of \$0.06/lb. at the 1000 kW level. Projected costs are as low as \$0.01-0.02/lb. in the range of 10,000 kW. A third advantage of our present system is its ability to operate with almost any gas environment, including hydrogen, oxygen and chlorine. This has permitted us to subject molten particles to an almost unlimited number of reducing, oxidizing and reactive environments. Conventional gas-solid reaction kinetics<sup>2</sup> continue to govern. However, with the molten particles it appears that liquid turbulence may be considerable and complete particle reaction can be achieved in many systems with particles below 100 microns. Iron ore is a good example of this. We have achieved nearly complete reduction in one pass through the device at power levels below 2 kWh/lb, even though the reaction is endothermic.

One can vaporize a considerable portion of the feed stock by increasing the kWh/lb. This gives the obvious advantage in some chemical reactions of creating a vapor for reaction with the environment. Under such circumstances the solid feed could be recycled until consumed. The power consumption for vaporization, however, would be in the range of two to seven times the power consumption required for spheroidizing, thus limiting such an application to relatively high priced materials. We have estimated the cost of producing fumed silica by such a technique, passing beach sand through the plasma and vaporizing 10-20 percent of it. Operating and amortization costs are in the range of \$0.15/lb. An interesting by-product is produced in this case; clear, amorphous silica spheres, which can be used as reflective beads in the sign and pavement lining industry. The advantage of silica over glass, which is used at present, lies in the superior reflectivity of silica.



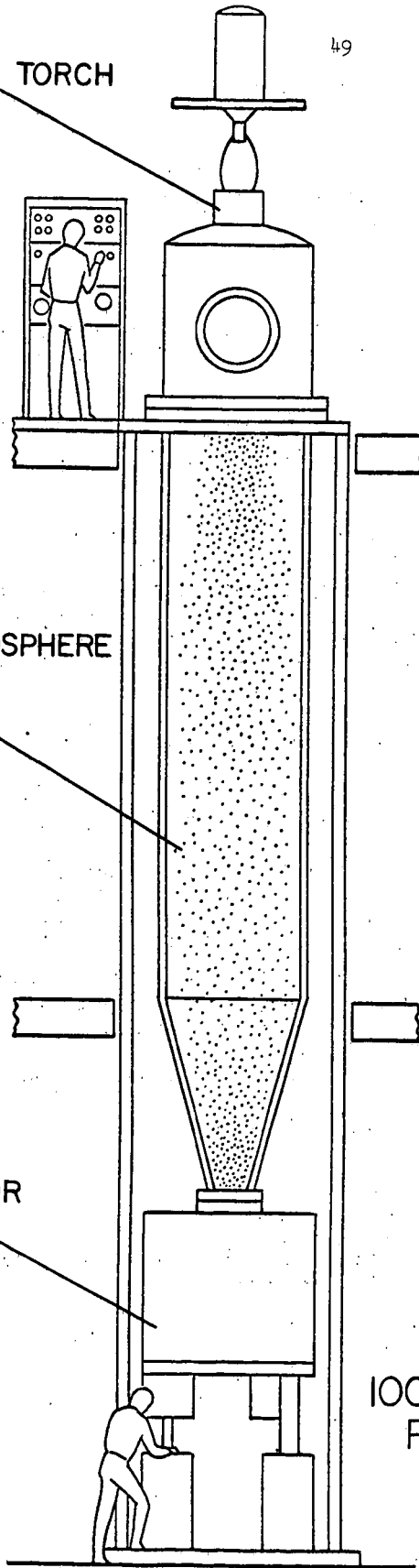
PLASMA TORCH

CONTROLLED ATMOSPHERE  
TANK

COLLECTOR

1000 KW - 1000 LB./HR.  
PLASMA POWDER  
FURNACE

FIG. 6



The hybrid particle heater, in which commercial scale activities are carried out, might be applicable or adaptable to the treatment of coal particles. The already promising economic picture derived from the work of Krukoniš and co-workers<sup>3</sup> for the Office of Coal Research might be made even more favorable.

The specific geometry of our hybrid particle heater is company confidential, however, we have made this system available to industry on a variety of business arrangement bases.

### CONTINUOUS MONITORING

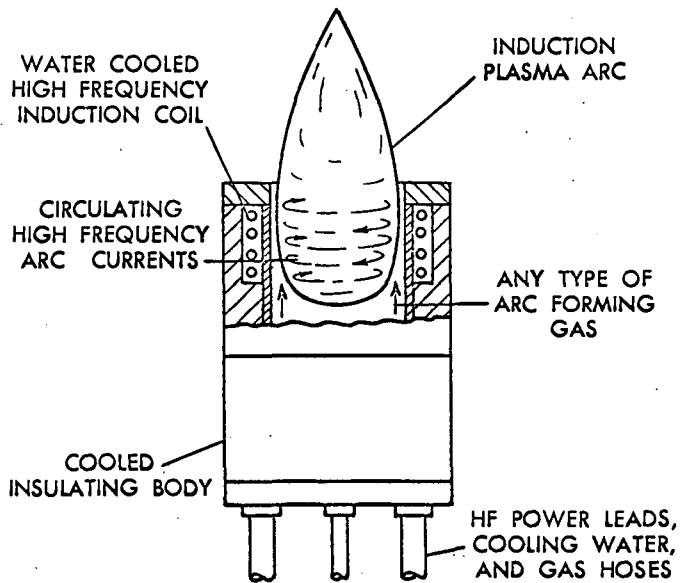
One application of solids heating which is quite interesting and timely is the determination of sulfur in coal and various ores. This can be either a pollution oriented or process control application and operates on the principle of instantaneous and complete oxidation of the test material, which is fed continuously into an oxygen plasma. Spectrographic or chromatographic techniques may be used to assay the resulting oxides.

### ORE PROCESSING

The spheroidization-dissociation phenomena described previously for zircon, which is the starting material for the zirconium oxide industry, typifies one of the applications of the plasma generator to ore processing. We have developed a complete flow sheet for the economic production of zirconium dioxide via the plasma route. This involves the dissociation of zircon ore (zirconium silicate) to zirconium dioxide and silica, followed by conventional hydrometallurgical processing of the dissociated product to various purities of zirconium dioxide. A variety of purities have been produced, ranging from 70 percent to ultrapure, hafnium-free nuclear grade material. It appears that the process has some economic advantages. Large samples of some of the grades have been produced and are in the hands of end users for evaluation.

### INDUCTION PLASMA HARDWARE

We have been active in the development of induction plasma heating systems for approximately 10 years. It is recalled that the induction plasma generator, shown in Figure 7, uses an intense electromagnetic field to heat



SCHEMATIC INDUCTION HEATER

FIG. 7

gases without hot electrodes. The basic advantages of the system, from the standpoint of heating solids and gases, include absolute freedom from contamination, since no electrodes are used and all containing materials can remain at water cooled temperatures. Second, the containing walls can be constructed of almost any material, ranging from quartz to nickel, hence, reactive gases can be handled with ease. Third, the device produces relatively large arc diameters (6-12 inches at 1000 kW). These large diameters result in velocities as low as 1-2 ft/sec and concomitantly long residence time. The simple gas mixing system of the induction plasma holds many advantages for performing chemical reactions. Moreover, performance has been improved in several areas recently to make the system even more attractive. A description of some of these improvements follows.

### 1. Power Density

Initially, plasma generators were constructed with quartz walls. Water cooling of the quartz was then added. This wall construction, however, was limited to power densities corresponding to the containment of diatomic gases at a maximum enthalpy of 7000 Btu/lb. Recently, segmented water cooled metal walls of the type shown in Figure 8 have been developed and operated at power levels up to 1000 kW. Diatomic gases at enthalpies of 40,000 Btu/lb. are successfully contained within these structures.

More recently, permeable walls have been utilized. This technique involves transpiration of a gas through the containing wall of the induction arc. This appears to have two advantages; first, essentially eliminating the wall heat loss to the device, which normally removes 20-30 percent of the input power; and second, preventing build-up of reactants and reaction products on the wall.

### 2. Pressure

Recently, torches have been operated at pressures in the range of 1000 psi. Previous to this only 1-2 atm. operation had been demonstrated reliably. This development should widen applications in the chemical industry. Reactions in which yields improve with increasing pressure, such as nitrogen fixation<sup>4</sup>, may become economically attractive.

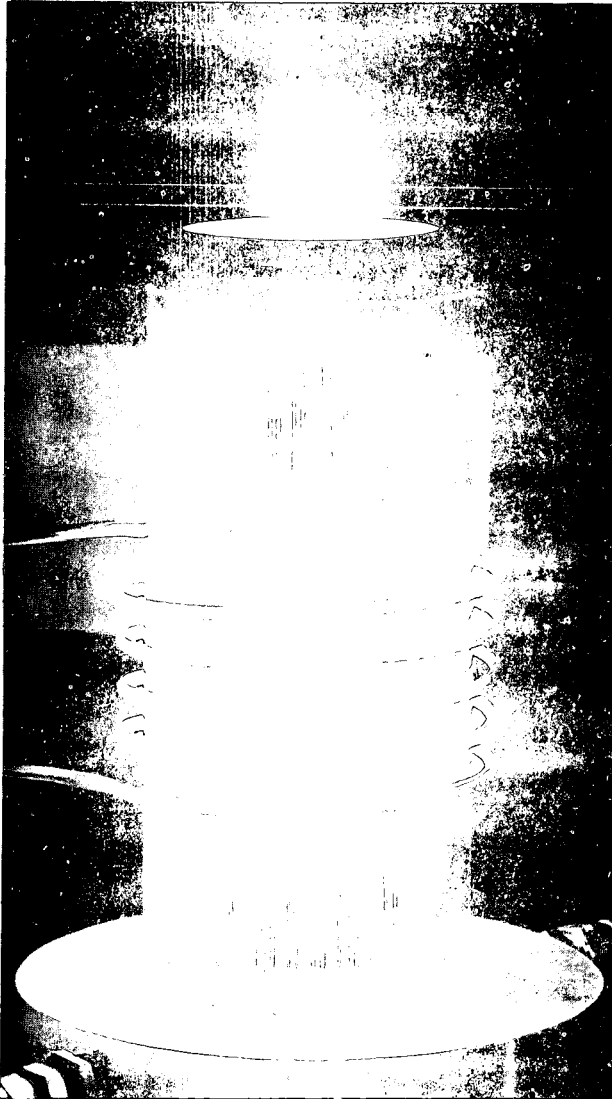


Figure 8. 6" Diameter Metal Wall Induction Torch in Operation at Low Power

### 3. Frequency

From the standpoint of power conversion economy, the ultimate in an induction chemical plant heater would be direct 60 cycle heating of gas. This now appears to be a possibility. During the past year, frequencies have been reduced from the 4 MHz-400 KHz range to 10 KHz. This has changed the power supply from an electron tube device to a motor generator, with consequent reduction in capital cost and simplified maintenance. Tests are presently underway at 960 Hz and a development program is underway to demonstrate 60 Hz heating during 1971.

## CONCLUSION

In summary, advances made during the past two years have taken processes to treat solids in plasma out of the laboratory and into the pilot plant. Economically justified large scale commercial processes have been designed and could be placed in operation with today's technology. In addition, recent improvements in plasma generating equipment and technology promise to speed the advent of large scale industrial plasma chemistry.

## REFERENCES

1. Levin, E.M. et al., "Phase Diagrams for Ceramists," American Ceramic Society, Columbus, Ohio, 1964.
2. Hougen, O.A., and Watson, K.M., Chemical Process Principles, John Wiley and Sons, Inc., New York, 1953, pp. 1063-1067.
3. Krunkonis, V., Phase I Feasibility Report - Avco Arc-Coal Process, Avco Space Systems Division, Lowell, Massachusetts, April, 1968.
4. Polak, L.S., and Stchিপatchev, V.S., "Kinetics and Thermodynamics of Chemical Reactions in Low Temperature Plasma," Nauka, Moscow, 1965, p. 151.

## DEUTERIUM LABELING OF PRODUCTS FORMED DURING PLASMA PYROLYSIS OF COAL

R. E. Gannon and V. J. Krukonis

AVCO Corporation S/D  
 Lowell Industrial Park  
 Lowell, Massachusetts 01851

INTRODUCTION

Studies have shown that rapid high temperature pyrolysis of coal produces gaseous products with acetylene as the predominant hydrocarbon species. (1-12) This is consistent with thermodynamic data (13,14) which indicate that at reaction temperatures of 1500 to 2000°C acetylene is the most stable of hydrocarbon species. The thermodynamic data also show that the stability of acetylene decreases below 1200°C; consequently, in a pyrolytic process for the production of acetylene two distinct steps must be considered, viz., a high temperature generation step and a quench step to inhibit acetylene decomposition.

During the Avco Arc Coal Program, sponsored by the Office of Coal Research, a program whose goal is the development of a commercially feasible plasma process for the conversion of coal to acetylene, it was observed that acetylene yields are greater when plasma pyrolysis is carried out in a hydrogen atmosphere rather than in other environments, e.g., helium, argon, or nitrogen. A comparison of acetylene yields for coal pyrolysis carried out in hydrogen and in argon is shown in Figure 1. The data show that yields in hydrogen are about twice those obtained in argon. Other experiments showed that helium and nitrogen were no more effective than argon.

The improved acetylene yields in hydrogen can undoubtedly be related to the two reaction paths by which acetylene is generated from coal. The first involves the reaction of hydrogen contained in the coal and the second utilizes an external source of hydrogen. The reactions are illustrated by the following equations:



The reaction described by equation (1) has been reported by several authors (5-9) and is illustrated by the data given in Figure 1 for the formation of acetylene in argon which shows the carbon and hydrogen in coal can react to form acetylene. The second reaction has been verified by injecting hydrogen-free char into a hydrogen plasma to form acetylene, (9), and also by reacting carbon and hydrogen at high temperature (16). The pyrolysis of coal in a hydrogen plasma, therefore, allows both reactions to contribute to the formation of acetylene, whereas, pyrolysis in an argon or helium plasma allows only reaction (1) to occur.

During the investigation of the quench step of the process, it became evident that hydrogen is also a more effective quench medium than is argon or helium. The quench reaction is complicated by the uncertainties in the acetylene generation reaction but uncertainties can be avoided, however, by separating the acetylene generation from acetylene quenching. For the investigation of the quenching reactions, known amounts of acetylene were used to model the generation step and reaction and decomposition during quenching were studied separately. The experiments were performed at a reduced pressure of 0.5 atmosphere, typical of the operating conditions of the AVCO Arc-Coal Process. Acetylene was metered into the arc plasma and inlet and exit gases were sampled and analyzed in order to measure the decomposition of the acetylene that occurred during

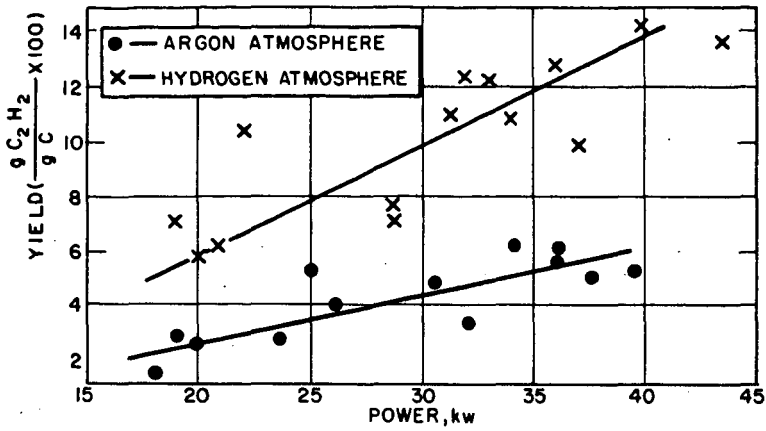


Figure 1 EFFECT OF ATMOSPHERE ON ACETYLENE YIELD

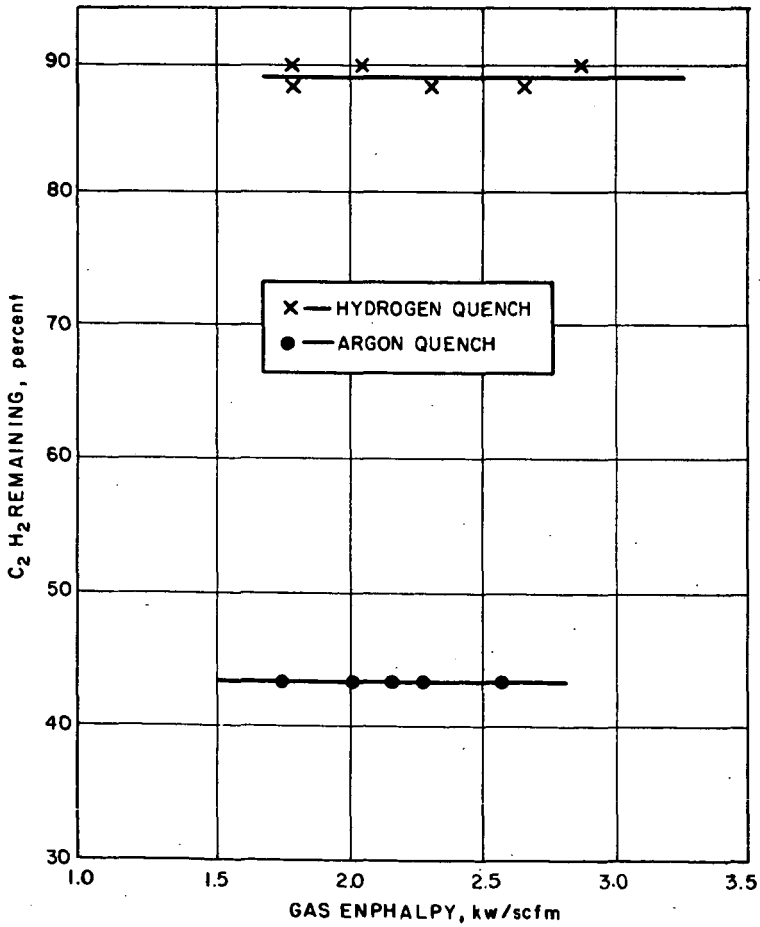


Figure 2 DECOMPOSITION OF ACETYLENE IN PLASMA PIPE REACTOR



the quenching process. The results, given in Figure 2, show that in hydrogen only about 12% of the acetylene is lost, whereas, in argon, decomposition was about 57%. Thus, at similar plasma enthalpy levels, the gross results show that hydrogen is a more effective quench medium.

Two reasons for the improved results with the hydrogen quench can be postulated, viz.,

- a. Hydrogen is a more effective coolant and rapidly lowers the temperature of the reaction mixture preventing excessive decomposition of acetylene.
- b. Hydrogen acts as a primary chemical reactant.

Using deuterium as "tagged" hydrogen atoms, a series of experiments was performed to elucidate the mechanism and to obtain a better understanding of the role of the hydrogen quench. For example, even though the data in Figure 2 showed that only 12%  $C_2H_2$  decomposed in  $H_2$ , it could not be determined whether the molecules analyzed in the effluent were the same molecules that were injected into the plasma. Deuterium was injected into the plasma with acetylene and the exit gases were analyzed mass spectrometrically to determine if any exchange occurred between acetylene and deuterium. If the role of the quench medium were strictly to prevent decomposition of  $C_2H_2$  molecules (as inferred by postulate a) there should be no exchange of the deuterium with acetylene and the product stream should be mainly  $C_2H_2$ ,  $H_2$ ,  $D_2$  (and perhaps  $HD$ ). If, on the other hand, postulate b, involving a chemical reaction, represents the role of the quench hydrogen (deuterium), then significant amounts of  $C_2HD$  and/or  $C_2D_2$  should be identifiable in the product stream.

## RESULTS AND DISCUSSION

Initial deuterium plasma reactions were designed to study the acetylene decomposition mechanism. A reactor, consisting of a 30 Kw, high temperature plasma generator, as shown in Figure 3, was used for the study. The generator could be operated on either hydrogen or deuterium and acetylene was injected directly into the plasma using either a hydrogen or deuterium carrier gas.

For the initial tests of the series, the plasma generator was operated at a reduced pressure of 0.5 atmosphere using deuterium as both the arc gas and as the carrier gas to convey given amounts of acetylene into the plasma. Gas flows were selected to give a mixture with an acetylene concentration typical of the product stream of the acetylene-coal reaction. Chromatographic analysis of the streams showed that the original mixture contained 7.1% acetylene which is representative of the 7 - 10% concentrations obtained during coal pyrolysis tests. Analysis of the effluent showed that 6.2%  $C_2H_2$  was present. The 13% loss of acetylene due to the decomposition in the deuterium plasma is consistent with previous data given in Figure 2 which shows about 12% decomposition for acetylene in the hydrogen plasma.

Mass spectrometric analysis of the product stream showed that only 1.0% of the acetylene present in the effluent (0.05% of the gas mixture) was not deuterated. Acetylene composition data are given in Table I and show that the acetylene does not remain molecular in the plasma, thus eliminating from further consideration Postulate a which states that the hydrogen quench acts to "preserve"  $C_2H_2$  molecules formed from coal by rapidly cooling the product stream. The data in Table I are also consistent with the data in Figure 2 which show for the range of power levels investigated that decomposition is relatively insensitive to gas enthalpy.

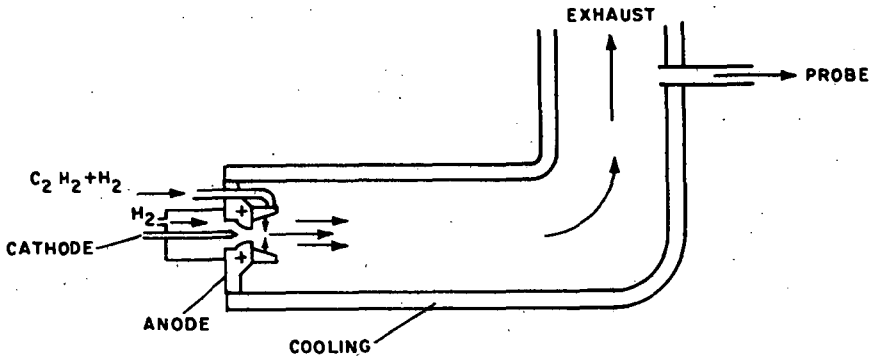


Figure 3 TUBE REACTOR

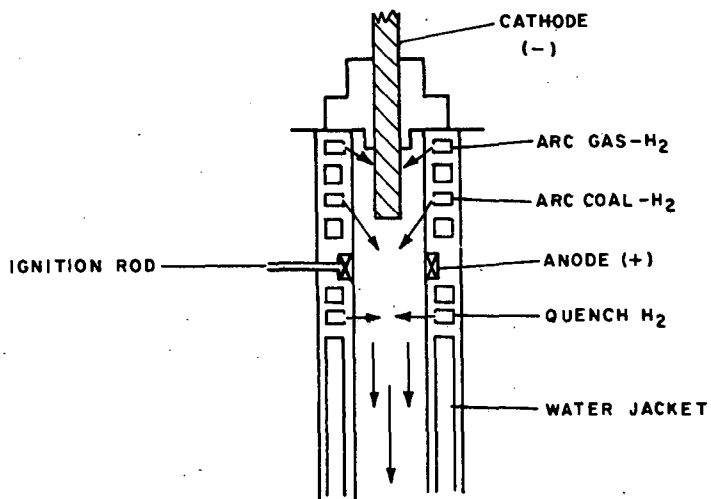


Figure 4 ROTATING ARC REACTOR

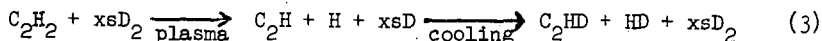
TABLE I

Measured Isotopic Composition of C <sub>2</sub> H <sub>2</sub> in Deuterium Plasma		
(D <sub>2</sub> - Arc Gas, D <sub>2</sub> - Quench Gas)		
Isotopic Species	Measured Composition	
	11.4 Kw	19.8 Kw
C <sub>2</sub> H <sub>2</sub>	1.1%	1.0%
C <sub>2</sub> HD	15.1%	15.7%
C <sub>2</sub> D <sub>2</sub>	83.5%	83.2%

Based on the observed results of the initial experiments; that is, 1) that essentially all the original C<sub>2</sub>H<sub>2</sub> exchanges with the deuterium and, 2) that about 87% of the deuterated product is identified as acetylene, it is evident that the description of the reactions of acetylene with hydrogen in the plasma (Postulate b) must allow for the high temperature decomposition of acetylene followed by its interconversion during the rapid cooling. A more complete description of the mechanism requires a better definition of the species present in the plasma.

Previous workers, Steacie (15), Plooster and Reed (16), and Borisova and Ermin (17), have considered the formation and decomposition of acetylene and its intermediate species under different test conditions but all came to a similar conclusion, viz., the most likely intermediate species at high temperature or other energetic conditions would be the C<sub>2</sub>H radical. Their conclusions were generally based on considerations of minimum energy requirements. In the decomposition of acetylene, five simple carbonaceous species are possible: C, CH, CH<sub>2</sub>, C<sub>2</sub>, and C<sub>2</sub>H. In order to form C, CH or CH<sub>2</sub>, the rupture of the triple acetylenic bond, requiring approximately 240 kcal, is necessary. The formation of C<sub>2</sub> requires the rupture of two C-H bonds, 150 kcal, whereas the formation of C<sub>2</sub>H requires the rupture of a single C-H bond, about 100 kcal. Other workers, Baddour and Iwasyk (18) and Baddour and Blanchet (19), studying the carbon-hydrogen reactions at plasma temperatures have also shown by calculation that C<sub>2</sub>H should be the prevalent species at temperatures between 2000 and 3000° K. Although the decomposition of acetylene via a C<sub>2</sub>H intermediate followed by re-combination with an H atom to re-form acetylene appears to be most likely from least energy considerations, the C<sub>2</sub>H radical has not been isolated or experimentally identified by any of the previous workers. On the other hand, traces of the C<sub>2</sub> radical which requires an additional 50 kcal for its formation has been identified by Steacie (15) and by Borisova and Ermin (17),

The C<sub>2</sub>H route has achieved among workers in plasma pyrolysis of hydrocarbons a foremost position to describe and explain yields of acetylene greater than those predicted by equilibrium calculations. The following reaction can be written to describe the C<sub>2</sub>H route in the deuterium plasma experiments.

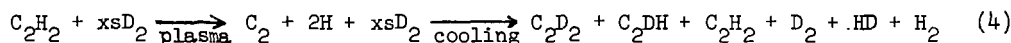


If equation (3) were a valid description of the reaction of acetylene in an arc plasma, then C<sub>2</sub>HD should be the predominant acetylenic species present in the product stream.

The experiments were carried out using 4.95 SCFM of D<sub>2</sub> and 0.38 SCFM of C<sub>2</sub>H<sub>2</sub>. Based upon statistical probability, the acetylene in the product stream should consist of 3.7% C<sub>2</sub>H<sub>2</sub> and 96.1% C<sub>2</sub>HD. The measured composition of 1.0% C<sub>2</sub>H<sub>2</sub>, 15.7% C<sub>2</sub>HD, and

83.2%  $C_2D_2$  shown in Table I was not consistent with equation (3) probability and it must be concluded that the mechanisms as written for postulate b, is not valid. It is also evident, because of the large amount of fully deuterated acetylene 83%, that any mechanism that postulates a  $C_2H$  radical as an incontrovertable entity throughout the lifetime of species in the plasma is not substantiate.

Because the  $C_2$  radical has been identified in some of the high temperature mixtures (15, 17), the contribution of this species should be considered as an intermediate. The following reaction describes such a mechanism:



Again, using the laws of statistical probability, it can be shown that for an original mixture of 4.95 SCFM  $D_2$  and 0.38 SCFM  $C_2H_2$  a product stream of 86%  $C_2D_2$ , 13.2%  $C_2DH$ , and 0.5%  $C_2H_2$  can be predicted, based on the reaction (4). The predicted composition is in excellent agreement with the measured composition given in Table I, and consequently indicates that the postulated  $C_2$  mechanism is an adequate model for predicting the product mix for the decomposition and reformation of acetylene in a plasma. In reconciling these results with the  $C_2H$  mechanism suggested by the previous authors (15, 16, 17), it must be recognized that, although the data precludes the existence of a  $C_2H$  entity that retains its identity throughout the decomposition and re-formation of acetylene, it does not preclude the existence of a  $C_2H$  radical that is able to experience multiple exchanges as indicated by Reaction (5), viz.,

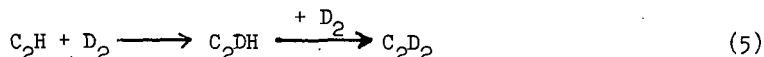


Table II summarizes the experimental results given in Table I and compares the data to those calculated on the basis of a mechanism that assumes: 1) a stable  $C_2H_2$  molecule, i.e., the  $C_2H_2$  mechanism, 2) a  $C_2H$  intermediate, and 3) a  $C_2$  intermediate species. The excellent agreement between the experimental results and those predicted by the  $C_2$  mechanism are obvious.

TABLE II

Isotopic Composition of Acetylene in Deuterium Plasma					
(D <sub>2</sub> - Arc Gas, D <sub>2</sub> - Quench Gas)					
Species	Measured Composition		Predicted Composition		
	14.4 kw	20.6 kw	C <sub>2</sub> H <sub>2</sub> mech.	C <sub>2</sub> H mech.	C <sub>2</sub> mech.
C <sub>2</sub> H <sub>2</sub>	1.1	1.0	100%	3.7%	0.5
C <sub>2</sub> HD	15.1	15.7	---	96.3%	13.2
C <sub>2</sub> D <sub>2</sub>	83.5	83.2	---	---	86.0

The  $C_2$  mechanism and the associated statistics were applied to subsequent tests in an effort to understand the roles of the various gas streams and their interactions with the coal feed. To distinguish between the roles of the arc gas and the quench stream, deuterium was used as the arc gas and hydrogen was used as the quench gas. The results of these tests are shown in Table III. An additional column, (the measured value minus the predicted value) has been added to indicate discrepancies from the predictions based on purely random selectivity (and equal reactivity) of the separate streams.

TABLE III

Isotopic Composition of Acetylene					
(D <sub>2</sub> - Arc Gas, H <sub>2</sub> - Quench Gas)					
Species	Measured Composition		Predicted Composition	Measured - Predicted	
	14.1 kw	20.5 kw		14.1 kw	20.5 kw
C <sub>2</sub> H <sub>2</sub>	21.4%	18.5%	29.2%	-7.8%	-10.7
C <sub>2</sub> HD	47.5	46.5	49.6	-2.1	-3.1
C <sub>2</sub> D <sub>2</sub>	31.0	35.0	21.2	+9.8	+13.8

The data indicate that the exchange is not purely statistical but instead that the acetylene exchanges with the higher enthalpy deuterium which has passed through the arc. The preference is obvious since the arc gas is hotter and more ionized than is the quench. If the explanation is valid, it should be possible to verify the preference of acetylene to exchange with gas which has passed through the arc by reversing the gas streams and using hydrogen as the arc gas and deuterium as the quench. Results of such tests are given in Table IV.

TABLE IV

Isotopic Composition of Acetylene					
(H <sub>2</sub> - Arc Gas, D <sub>2</sub> - Quench Gas)					
Species	Measured Composition		Predicted Composition	Measured - Predicted	
	15.7 kw	21 kw		15.7 kw	21 kw
C <sub>2</sub> H <sub>2</sub>	38.0	40.7	30.2	+7.8	+10.5
C <sub>2</sub> HD	45.7	45.6	49.6	-3.9	-4.0
C <sub>2</sub> D <sub>2</sub>	16.0	13.7	20.2	-4.2	-6.5

Again, consistent with the previous tests, it is seen that the arc gas is more reactive than the carrier gas, and it is also consistent that in each test the arc gas appears to be more reactive at higher power levels.

In order to investigate the combined or simultaneous reactions of acetylene generation and quench reactions during coal pyrolysis, deuterium was used as a carrier gas to conduct coal into a deuterium plasma. Although deuterium was the only gas introduced into the reactor, it was necessary to consider the amount of hydrogen which was liberated from the coal in applying the statistical analysis. With a Pittsburgh Seam Coal with a 5% hydrogen content and 160 g/min feed, a maximum of 3.24 SCFM of H<sub>2</sub> was introduced into the arc reactor. The measured distribution of the deuterated acetylenic species at several power levels is given in Table V and the data are compared with the predicted distribution based on C<sub>2</sub> statistics.

TABLE V

Isotopic Composition of Acetylene Generated During Coal Pyrolysis				
(D <sub>2</sub> - Arc Gas, D <sub>2</sub> - Quench Gas, 0.5 Atm)				
Species	Measured Composition			Predicted Composition
	10.8 kw	13.6 kw	16.0 kw	(100% Utilization of H <sub>2</sub> in Coal)
C <sub>2</sub> H <sub>2</sub>	3.6%	3.8%	5.1%	10.8%
C <sub>2</sub> HD	25.0	27.5	31.6	44.2
C <sub>2</sub> D <sub>2</sub>	71.3	68.8	63.2	45.0

The discrepancy between the measured and predicted values is probably caused by the assumption in the calculations that 100% of the hydrogen in the coal is liberated for acetylene generation. Chemical analyses have shown that appreciable amounts of hydrogen still remain in the char. Recalculating the predicted distribution based on a fractional availability of hydrogen from the coal results in more quantitative agreement with the measured values as shown in Table VI.

TABLE VI

Comparison of Measured and Predicted Isotopic Distribution of Acetylene Generated During Coal Pyrolysis								
(D <sub>2</sub> - Arc Gas, D <sub>2</sub> - Quench Gas, 0.5 Atm.)								
Species	Measured Composition			Calculated Dist. Based on Available H <sub>2</sub>				
	10.8 kw	13.6 kw	16. kw	30% H <sub>2</sub>	35%	40%	45%	50%
C <sub>2</sub> H <sub>2</sub>	3.6	3.8	5.1	1.6	2.2	2.7	3.4	4.0
C <sub>2</sub> HD	25.0	27.5	31.6	22.6	25.4	27.6	30.0	32.0
C <sub>2</sub> D <sub>2</sub>	71.3	68.8	63.2	75.6	72.8	69.7	66.5	64.0

By comparing the measured distribution with the calculated values, it appears that at 10.8 kw about 35% of the hydrogen in the coal is available for acetylene formation, at 13.6 kw the value increases to about 40%, and at 16 kw it increases to 50% level.

The role of the quench medium in the prototype reactor for the AVCO Arc-Coal Process was then investigated. The prototype reactor, shown in Figure 4, basically consists of a solid cylindrical graphite cathode, 5/8" in diameter and an annular graphite anode with a 1½" I.D. Pulverized coal is injected directly into the plasma as shown in the figure and quenching is accomplished by injecting hydrogen about ½" below the anode. The arc operates at power levels between 80 and 120 kw. Magnetic field coils around the anode induce a high speed rotation to the arc which increases the effectiveness of contact between the pulverized coal and the high temperature environment, and also serves to stabilize the arc.

In these tests the arc gas and coal-carrier gas was hydrogen but deuterium was used as the quench gas so that the role of the quench could be studied. The resulting distribution of the acetylenic species is given in Table VII as well as a

calculated distribution based on test parameters, viz., 11.5 SCFM arc gas, 5.8 SCFM coal carrier gas, 3.24 SCFM of  $H_2$  contained in the coal and 10.6 SCFM deuterium quench gas. The 3.24 SCFM of  $H_2$  from the coal is based on 100% availability of the  $H_2$  in the coal. This estimate is undoubtedly high and 60 to 70% is probably more realistic, but in this test in which 17.3 SCFM and  $H_2$  were passed through the arc any small error in the amount of the  $H_2$  liberated from the coal would have a negligible effect on the calculation.

TABLE VII

Coal Conversion to Acetylene in Prototype Reactor with Deuterium Quench			
Species	Measured Distribution	Calculated Distribution	Measured - Calculated
$C_2H_2$	55%	43.5%	+11.5
$C_2HD$	38.8	44.8	- 6.0
$C_2D_2$	6.6	11.6	- 5.0

This experiment was similar to a previous experiment (Table V) in that hydrogen was used as the arc gas and deuterium was added downstream. The differences between the measured and calculated values again indicate the higher reactivity of the arc gas. Nonetheless, it is to be noted that the quench gas was identified in 45% of the acetylene product. If the quench gas had been argon or other relatively inert gas, no viable compound would have been formed in these reactions and the high temperature acetylene species,  $C_2$  and  $C_2H$ , would have decayed to carbon. Similarly, consecutive exchange reactions could not occur with inert gas present.

### CONCLUSIONS

Conclusions about the decomposition of acetylene in a hydrogen atmosphere that can be drawn from the series of deuterium plasma reactions can be summarized as follows:

1. Reaction mechanisms which require undisassociated  $C_2H_2$  or a  $C_2H$  entity cannot be substantiated.
2. Calculations which utilize a route involving a  $C_2$  intermediate can be used to predict the product distribution.
3. At low gas enthalpy levels, only a small percentage of the hydrogen in the coal takes part in acetylene formation. As power is increased, more hydrogen is liberated from the coal for acetylene formation.
4. Although the results show that the arc gas is more reactive than the quench gas, they also show that the quench reacts chemically in preserving acetylene. For this reason, the use of a hydrogen quench is important in obtaining high acetylene yields.

### ACKNOWLEDGEMENTS

This work is being supported by the Office of Coal Research, U. S. Department of the Interior, under Contract No. 14-01-000-493.

The technical contributions of Albert Bothe, Robert McDonough and Richard Reudiger in planning and performing the described experiments are acknowledged and appreciated. The mass spectrographic analyses were performed at the Massachusetts Institute of Technology using their high resolution mass spectrograph. The guidance and assistance of Professor Klaus Bieman and Dr. Guy Arsenault in performing experiments and analyzing the data were most valuable.

#### REFERENCES

1. Littlewood, K., McGrath, I. A., Paper C9, 5th International Conference on Coal Science, Cheltenham, (1963).
2. Rau, E., Seglin, L., Fuel 43, (2), 147-57, (1964).
3. Rau, E., Eddinger, R. T., Fuel 43, (3), 246, (1964).
4. Sharkey, A. G., Jr., Schultz, J. L., Friedel, R. A., Coal Sciences, Advances in Chemistry, Ser. 55, 560-65, (1966).
5. Bond, R. L., Ladner, W. R., McConnell, G. I. T., Coal Sciences, Advances in Chemistry, Ser. 55, 650-65, (1966).
6. Kawa, W., Graves, R. D., Hiteshue, R. W., U. S. Bureau of Mines, Department of Investigation, 6829, (1966).
7. Kawana, Y., Makino, M., Kimura Tatsuo, Kogyo Kagaku Zasshi, 69, (6), 1144-50, (6).
8. Newman, J. O. H., Coldrick, A. J. T., Evans, P. L., Kempton, T. J., O'Brien, D. G., Woods, B., 7th International Conference on Coal Science, Prague, (1968).
9. Krukoniš, V. J., Schoenberg, T., Paper 5-132, 7th International Conference on Coal Science, Prague, (1968).
10. Fu, Y. C., and Blaustein, B. D., I. & E. C. Process Design and Development, Vol. 8, p. 257, April 1969.
11. Krukoniš, V. J., Gannon, R. E., Schoenberg, T., 19th Canadian Engineering Conference, Edmonton, Alberta, (1969).
12. Gannon, R. E., Krukoniš, V. J., and Schoenberg, T., I and E. C. Product Research and Development, September 1970, (Scheduled).
13. Wagman, D. D., Kilpatrick, J. E., Pitzer, K. S., Rossini, F. D., J. Res. Nat. Stand., 35, 467, (1945).
14. Howard, Wood, Kaltenbacher, Chem. Eng. Prog., 57, (11) 50, (1961).
15. Steacie, E. W. R., Atomic and Free Radical Reactions, 2nd Ed. Reinhold, New York, (1954).
16. Flooster, M. N., and Reed, T. B., J. Chem. Phys., 1959, 31, p. 66.
17. Borisova, E. N., and Eremin, E. N., Organic Reactions in Electrical Discharges, Consultants Bureau, (1968).
18. Baddour, R. F., and Iwasyk, J. M., I. and E. C. Process Design and Development, Vol. 1, No. 3, July 1962, p. 169.
19. Baddour, R. F., and Blanchet, J. L., I. & C. Proc. Design Devel., Vol. 3, p.258, 1964.



PROBE DIAGNOSTICS OF  
HIGH - TEMPERATURE GASES

Jerry Grey

Greyrad Corporation  
Princeton, New Jersey

INTRODUCTION

Cooled probes have been developed as a direct result of the need to measure gas properties at high temperatures or in corrosive environments. Originally developed for "exotic" gas environments at temperatures so high as to entirely preclude the use of more conventional methods, (e.g., arcjets, rocket engines, hyperthermal wind tunnels), cooled probe techniques have only recently been applied to the more moderate temperatures encountered in industrial furnaces, thermal cracking columns, incinerators, nuclear power reactors, metal smelting and refining furnaces, etc.

The most frequently used cooled-probe method is the calorimetric principle, for the measurement of gas enthalpy (and thereby the gas temperature, in most industrial applications). Specific benefits of this method are as follows:

(a) Maximum probe material temperature may be maintained only a few degrees higher than that of the coolant, thereby providing long life in high-temperature or corrosive gas environments. This feature can be contrasted with thermocouples, resistance thermometers, or even fluidic oscillators, which by their very nature must operate at the temperature of the gas to be measured.

(b) The cooled calorimetric probe functions solely as a mechanical structure; that is, it can be fabricated from materials which are fully compatible with the environment, since it requires no special electrical properties as do thermocouples or resistance thermometers. Further, even if some material deterioration does occur, the probe's operation is totally unaffected, as compared with the other devices, which immediately begin to suffer variations in electrical output.

(c) Effects on probe output signal due to contamination by particulate matter, condensibles, etc., which may erode or coat the probe, are generally negligible or can be eliminated

by either relatively simple coolant flow management or periodic cleaning of the probe's internal passage in situ, with access from the outside.

(d) Since the output sensors are located remotely from the probe tip, they can be serviced or replaced without removing the probe itself from the measurement region. This feature is particularly important in nuclear reactor core measurements or in any other application where instrumentation replacement would otherwise require a plant shutdown.

(e) For environments which are so severe as to have been formerly inaccessible to all but remote temperature measurement (e.g., optical pyrometers), the cooled immersion probe provides a degree of accuracy and multiplicity of measurement far beyond that attainable with non-local viewing devices of comparable cost and complexity.

(f) In many applications, the direct probe output signal can be made proportional to either gas enthalpy (temperature) or total power (product of enthalpy or temperature and mass flow rate).

Disadvantages of the cooled calorimetric probe as compared with more conventional immersion devices (e.g., thermocouples or resistance thermometers) are high first cost and the requirement for a coolant supply. It can, however, be argued that the higher first cost of a cooled probe installation is more than compensated by its greater lifetime and higher reliability, both of which sharply reduce plant shutdown time or failures due to deterioration or loss of control function. Also, in most industrial applications, readily-available shop air supplies or city water provide adequate probe coolant capability.

The present paper provides a review of cooled calorimetric probe principles and applications, and mentions several other cooled-probe diagnostic techniques applicable to industrial environments.

#### THE COOLED CALORIMETRIC PROBE

The basic principle of the calorimetric probe is as follows: a small sample of the gas to be measured is allowed to flow continuously through a hollow-walled tube. The tube walls are cooled by either a gas (e.g., air, nitrogen, hydrogen, helium, etc.) or a liquid (e.g., water, hydraulic fluid, ethylene glycol, etc.). By measuring the heat given up to the coolant by the hot

gas sample, therefore, one can determine directly what its enthalpy was before it was cooled.

The simplest form of this device (Ref. 1) is the so-called "tare-measurement" probe (Figure 1), in which the coolant serves not only as the calorimetric fluid, but also to cool the probe exterior. In this case two measurements are required: first the total coolant energy is measured (coolant flow multiplied by its temperature rise); then the gas sample flow is shut off by a valve and the coolant energy is measured again (the "tare" measurement). The difference between the two coolant energy measurements is then the enthalpy given up by the gas sample:

$$h_{ig} = \frac{(w_c c_{pc} \Delta T_c)_f - (w_c c_{pc} \Delta T_c)_{nf}}{w_g} + c_{p2g} T_{2g}$$

where

$w_c$  = coolant flow rate (lb/sec)

$c_{pc}$  = coolant specific heat, (Btu/lb-°F)

$\Delta T_c$  = coolant temperature rise, (°F)

$w_g$  = gas sample flow rate, (lb/sec)

$c_{p2g}$  = cooled gas sample constant-pressure specific heat at probe exit, (Btu/lb-°F)

$T_{2g}$  = cooled gas sample temperature at probe exit, (°F)

$()_f$  indicates gas sample flowing

$()_{nf}$  indicates gas sample flow shut off

The principal purpose in utilizing this type of probe is that its simplicity of design permits the use of very small over-all diameters (as small as 1/32"), and also provides effective cooling in extremely high heat-flux environments. It is particularly useful where the operating conditions are such that the tare or calibration measurement need only be made periodically (e.g., once per hour or per day), i.e., wherever temperature, flow, and pressure conditions do not vary over wide ranges. Under these conditions, the tare-measurement probe becomes a useful, practical, continuous-output instrument.

Note that in order to provide proper duplication of heat

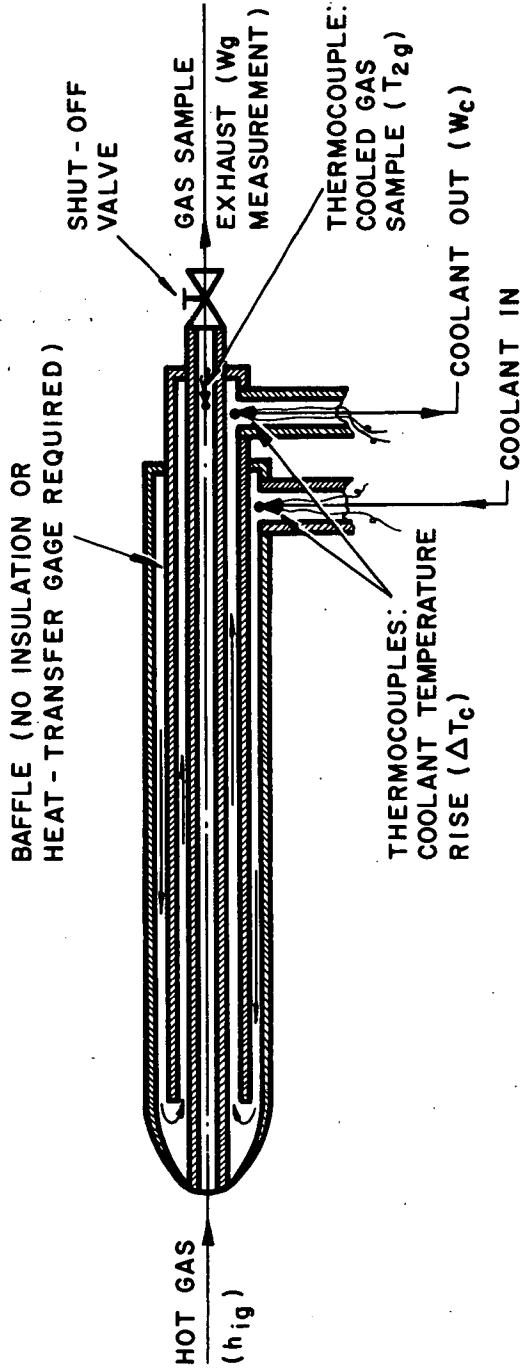


FIGURE 1

SIMPLE TARE-MEASUREMENT PROBE FOR MEASUREMENT OF ENTHALPY,  
IMPACT PRESSURE, AND GAS COMPOSITION.

flux to the exterior of the probe between the "tare" and "non-tare" measurements, it is necessary that the gas sample flow rate be sufficiently small so as not to disturb the general flow pattern at the probe tip. When the product of gas pressure and enthalpy drops so low that this requirement conflicts with the requirement for adequate sensitivity (i.e., difference in coolant temperature rise between the tare and non-tare measurements), this class of probe has reached its limit of usefulness.

In this event, and for lower heat-flux conditions in general, the fully-isolated non-tare-measurement probe of Figure 2 is recommended (Ref. 2). Here the calorimetric portion of the probe is isolated from the cooling jacket by an air gap (this may, obviously, also be vacuum or another gas). The enthalpy measurement is then obtained directly, without the necessity for a tare measurement, as follows:

$$h_{ig} = \frac{(\dot{w}_c c_{pc} \Delta T_c)_i}{w_g} + c_{p2g} T_{2g}$$

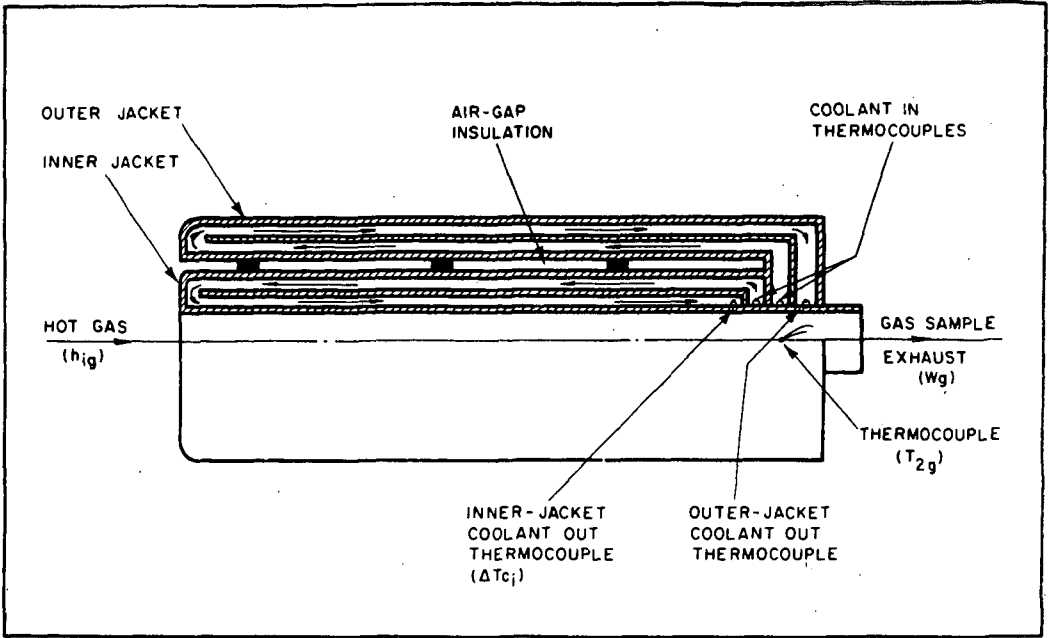
where now subscript ( )<sub>i</sub> indicates the inner calorimetric jacket, and all other notation is indicated below the previous equation.

The only conditions on the use of the non-tare-measurement probe are

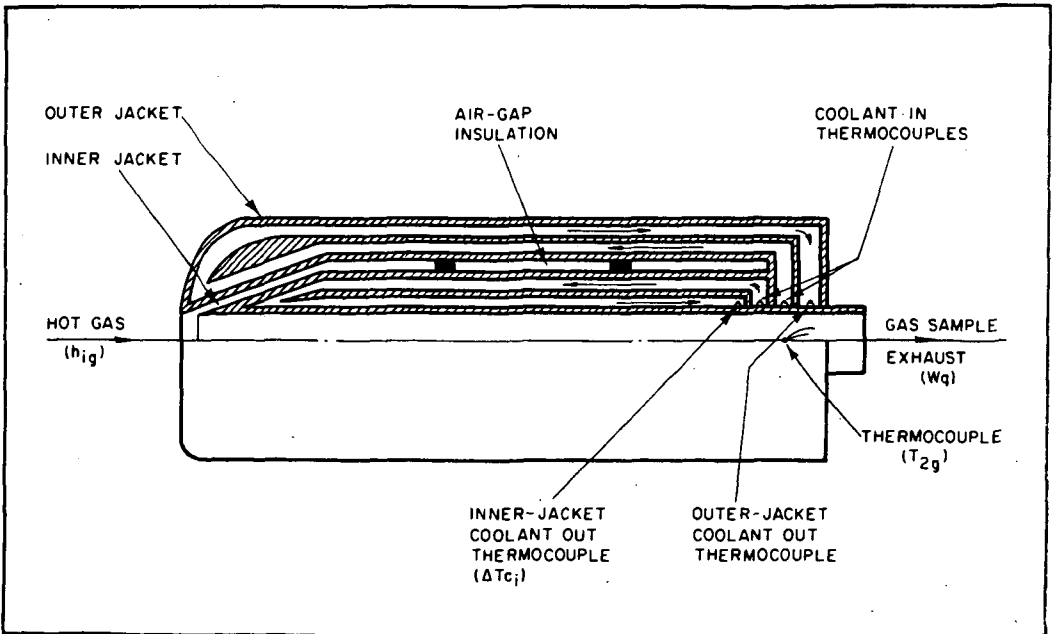
- (a) No heat transfer occurs between the inner and outer jackets of Figure 2.
- (b) All of the gas which is aspirated is cooled by the inner jacket, and none of it is cooled by the outer jacket.

The first of these conditions is accomplished by designing the probe geometries and relative coolant flow rates through the two jackets so that wall temperatures at opposing points all along the air gap will be as nearly equal as possible, thus minimizing interjacket heat transfer. The second condition is achieved either by proper adjustment of the aspirated gas sample flow rate (i.e., locating the flow stagnation point at the insulation-gap entrance), or, in Configuration A of Figure 2, by correcting for the small amount of heat transfer to the exposed portion of the calorimeter.

In either of these probe designs, if the cooled gas sample temperature  $T_{2g}$  is either (a) very nearly equal to the calorimetric coolant exit temperature; (i.e., the probe length/diameter ratio is sufficiently large), or (b) very nearly constant, or



CONFIGURATION "A"



CONFIGURATION "B"

FIGURE 2

CONTINUOUS-FLOW JACKETED CALORIMETRIC PROBE

(c) very low compared with the "unknown" hot gas temperature, the measurement of  $T_{2g}$  can be eliminated. Also, for long-term monitoring purposes, the coolant flow rate can be controlled to a preset value, so it need not be measured, and the cooled gas sample flow can be extracted through a choked orifice so that its flow rate will be directly proportional to the gas pressure at the orifice inlet (its temperature is already known). The only auxiliary requirements under these conditions, therefore, are a constant-mass-flow source of coolant and recorders for one pressure and either the coolant temperature rise or the inlet and outlet coolant temperatures (measured by thermocouples, resistance thermometers, or thermistors).

Note also that both probe designs permit measurement of impact pressure (intermittently in the tare probe; continuously in the jacketed probe, via the insulating gap) and extraction of gas samples for composition measurement or monitoring. Either probe can be bent at angles up to  $90^\circ$ , and all instruments, fittings for coolant flow, etc. are mounted in a series of modular terminator blocks at the probe base (see Fig. 3).

It is of particular interest to note that if the probe  $L/D$  is sufficient, there will be virtually no effect on probe output due to even extensive contamination by combustion or corrosion products. In fact, if  $T_{2g}$  is monitored, no amount of contamination or corrosion can affect the probe output, up to the point of physical failure of the probe structure. (The gas sample passage can be cleaned periodically from the outside, if necessary, without removing the probe, by simply removing the discharge orifice fitting and inserting a pipe cleaner or scraper through the gas sample tube -- see Fig. 3.)

This type of probe has been employed extensively for enthalpy and temperature measurements in arcjet environments (e.g., see Refs. 3,4,5,6,etc.). An indication of the calorimetric probe's repeatability is shown in the turbulent-flow profile measurements of Figure 4 (from Ref. 7); Figure 5 shows the accuracy obtained with even the relatively crude tare-measurement probe (Ref. 3).

One particularly useful application of the calorimetric probe principle is in the control of a Brayton power cycle; e.g., the gas turbine engine. It can be shown (Ref. 8) that if the probe is located at the inlet to the turbine (the combustion chamber exit) and is cooled by compressor discharge gas, the calorimetric jacket temperature rise is almost directly proportional to the turbine inlet temperature; i.e., no flow measurements are required:

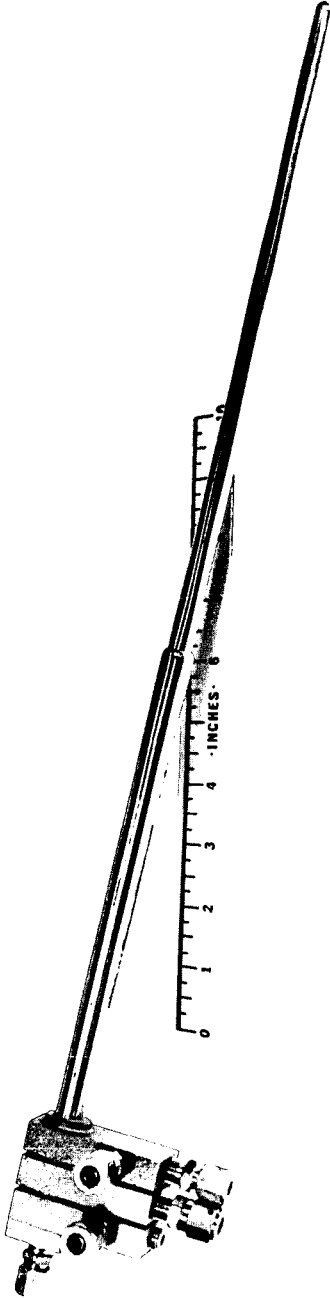


FIGURE 3

TYPICAL COOLED CALORIMETRIC  
PROBE CONFIGURATION FOR  
INDUSTRIAL APPLICATIONS



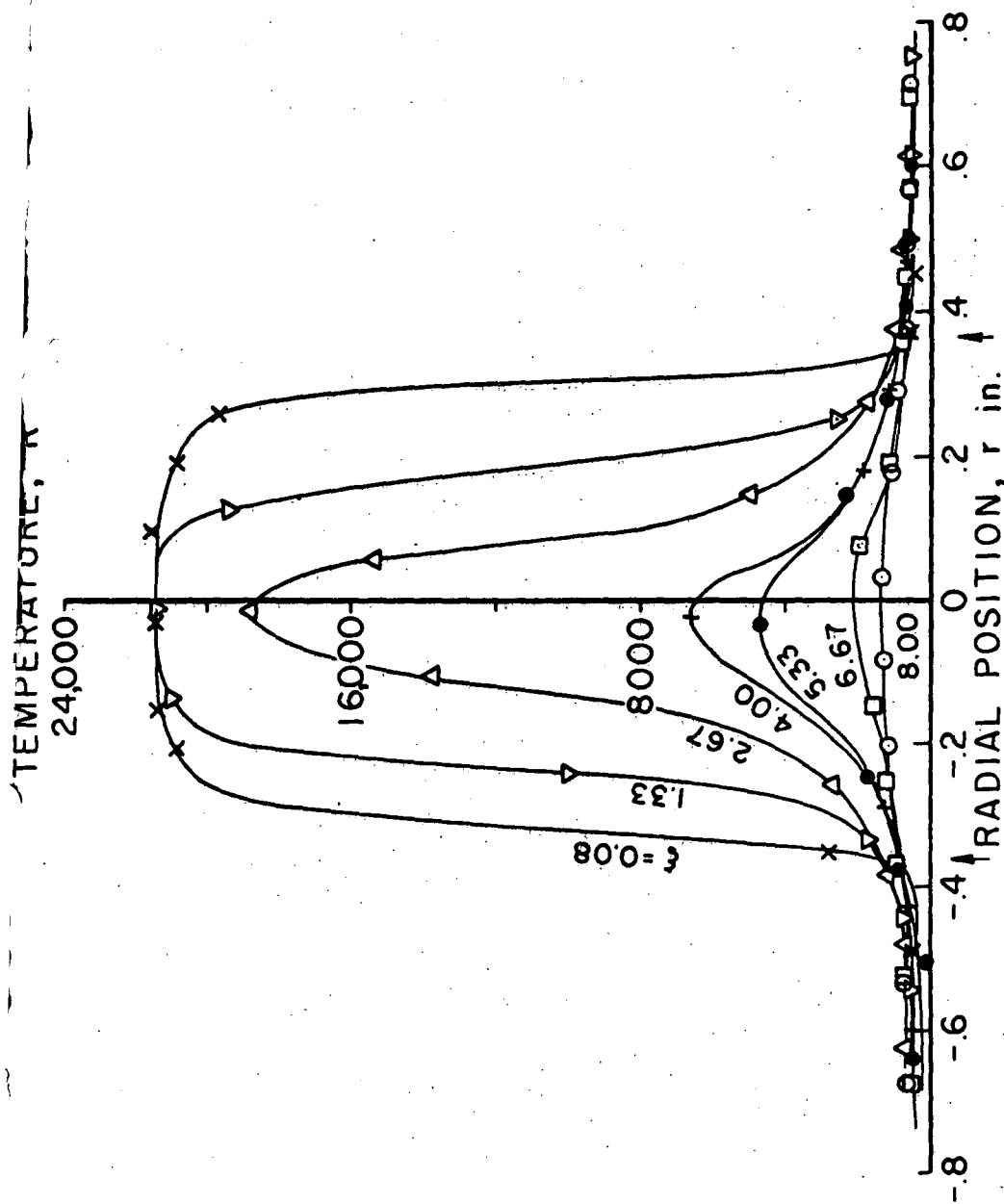


FIGURE 4

TYPICAL COOLED-PROBE TURBULENT-FLOW  
PROFILE MEASUREMENTS

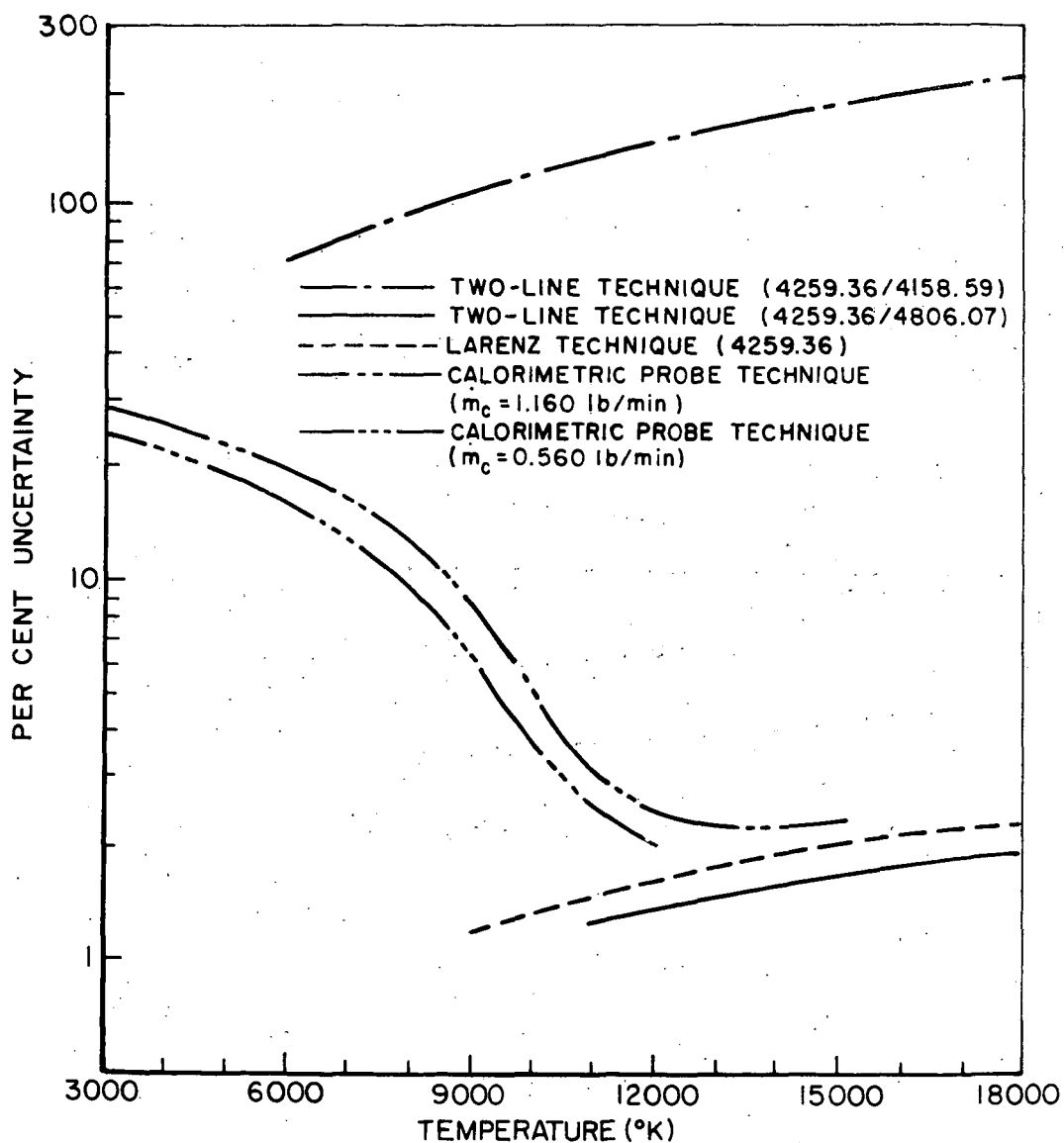


FIGURE 5.

CRUDE TARE-MEASUREMENT CALORIMETRIC  
 PROBE ACCURACY COMPARED WITH  
 SPECTROMETRIC METHODS

PRD-057

$$T_{t4} \approx k_1 + k_2 (\Delta T_i)$$

where  $T_{t4}$  = total temperature at turbine inlet, °R

$k_1, k_2$  are approximately constant

$\Delta T_i$  = temperature rise of the coolant in the calorimetric jacket, °F

On the other hand, if the probe is cooled by a constant-flow, constant-temperature coolant source (e.g., hydraulic fluid, fuel, compressed air, water, etc.), it can be shown (Ref. 8) that the calorimetric coolant temperature rise is directly proportional to the product of engine mass flow rate and turbine inlet temperature; i.e., to total engine power:

$$W_a T_{t4} \approx k_3 + k_4 (\Delta T_i)$$

where  $W_a$  = engine air mass flow rate

$k_3, k_4$  are approximately constant

#### OTHER COOLED-PROBE MEASUREMENTS

The concept of utilizing cooled immersion surfaces has been applied to such diverse hot-gas property measurements as electron temperature and density in plasmas (Ref. 9), scale of turbulence (Ref. 10), degree of nonequilibrium (Ref. 11), radiation intensity (Ref. 12), transient pressure oscillations (Ref. 13), heat flux (Refs. 14, 15), velocity (Ref. 16), temperature (Ref. 17), and, of course, the pressure and gas sampling functions already discussed. In fact, single probes with multiple functions can often minimize the total instrumentation requirement. Figure 6, for example, shows a multipurpose probe used for diagnostics of a sonic-velocity RF-generated plasma, with simultaneous measurement capability for enthalpy, electron temperature and density, impact pressure, static pressure, and gas-sample extraction. In many industrial applications where multiple measurements are required, but where either access is difficult or lifetime is a problem, the use of a single cooled probe to perform many functions can often be highly effective.

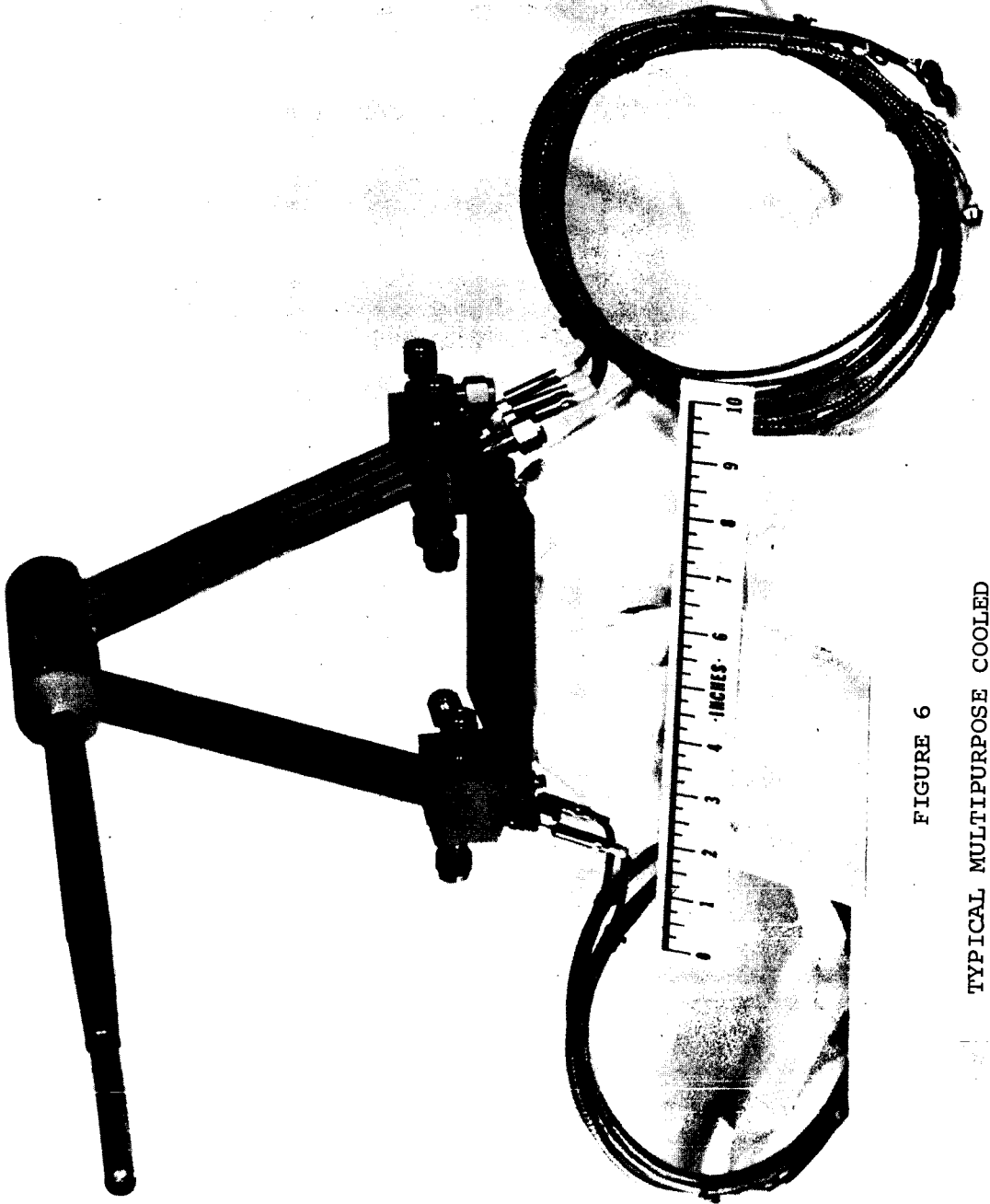


FIGURE 6

TYPICAL MULTIPURPOSE COOLED  
PROBE FOR PLASMA DIAGNOSTICS

## REFERENCES

1. Grey, J., Jacobs, P. F., and Sherman, M. P., "Calorimetric Probe for the Measurement of Extremely High Temperatures," Rev. Sci. Instr. 33, July 1962, pp. 738-741.
2. "High-Sensitivity, Continuously-Aspirating Calorimetric Probe," Greyrad Corporation, Princeton, N. J., Bulletin G-13, 1969.
3. Incropera, F. P., and Leppert, G., "Investigation of Arcjet Temperature-Measurement Techniques," ISA Transactions 6, Jan. 1967, pp. 35-41.
4. Grey, J., "Thermodynamic Methods of High Temperature Measurement," ISA Transactions 4, April 1965, pp. 102-115.
5. Au, G. F., and Sprengel, U., "Kalorimetrische Messungen von örtlichen Temperaturen und Geschwindigkeiten in einem Stickstoff-Plasmastrahl," Zeitschrift für Flugwissenschaften 14, 1966, Heft 4, pp. 188-194.
6. Grey, J., "Cooled Probe Diagnostics of Dense Plasma Mixing and Heat Transfer Processes," AIChE Preprint 9c, 69th Annual Mtg., N. Y., Nov. 26-30, 1967.
7. Grey, J., and Jacobs, P. F., "Experiments on Turbulent Mixing in a Partially Ionized Gas," AIAA Journal 2, March 1964, pp. 433-438.
8. Grey, J., "Calorimetric Temperature Measurement," Tutorial Proc. of the 15th Int'l. ISA Aerospace Instrumentation Symposium, May 5-7, 1969, pp. 110-119.
9. Grey, J., and Jacobs, P. F., "The Cooled Electrostatic Probe," AIAA Journal 5, Jan. 1967, pp. 84-90.
10. Reitsma, D., "Evaluation of Electrostatic Probe for Turbulence Measurements," MSE Thesis, Princeton University, Princeton, N. J., 1969.
11. Jacobs, P. F., and Grey, J., "Criterion for Electron-Heavy Particle Nonequilibrium in a Partly-Ionized Gas Jet," AIAA Paper No. 66-192, Monterey, California, March 2-4, 1966.
12. Grey, J., Jacobs, P. F., and Sherman, M. P., "Measurements of Arcjet Radiation with a Cooled Collimated Probe," IEEE Transactions on Nuclear Science, Vol. NS-11, Jan. 1964, p. 176.

13. Rogero, S., "Internal Rocket-Engine Probes for Use in a Combustion Instability Environment," Proc. 15th Int'l. ISA Aerospace Instrumentation Symposium, May 5-7, 1969, pp. 84-88.
14. Grey, J., "Cooled Probes for Gas Measurements at Very High Temperatures," Space-Aeronautics, Oct. 1968, pp. 82-84.
15. "Cooled Heat-Flux Gages and Probes," Bulletin 68G15, Grey-rad Corporation, Princeton, N. J., 1968.
16. Cooley, W. C. and Wilkinson, J. B., "A Survey of Probe Techniques for Measuring Plasma Velocity," ASME, 88th Winter Annual Meeting, Pittsburgh, Pa., Nov. 12-17, 1967.
17. Raezer, S. D., and Olsen, H. L., "The Intermittent Thermometer: A New Technique for the Measurement of Extreme Temperature," Paper No. 83 in Temperature--Its Measurement and Control in Science and Industry, Vol. 3, Part 2, Reinhold, N. Y., 1962.

## LARGE A.C. ARC HEATER...DESIGN, PERFORMANCE AND ECONOMICS

Authors: M. G. Fey, Westinghouse Electric Corporation, Arc Heater Engineering,  
11L15, East Pittsburgh, Pa. 15112

C. Hirayama, Westinghouse Electric Corporation, R&D Center,  
Churchill Boro, Pittsburgh 35, Pa. 15235

After chemical performance has been demonstrated, a plasma generation device must meet several other requirements before it can be considered for an industrial process. These include: 1) stable, long-time operation on chemical feedstocks, 2) simple, rugged design, 3) minimum downtime and, 4) low capital cost.

An industrial arc heater is described in which the chemical feedstock is passed through a magnetically rotated arc discharge. A unique self-stabilizing feature permits multi-megawatt operation on line-frequency alternating current. Spurious arc extinctions are completely eliminated. A secondary feedstock, which may be a particulated solid, can be admitted axially through the arc discharge. Heat transfer between the arc and the feedstock and turbulent mixing of the reactants are enhanced by high speed arc rotation and a.c. power pulsations. Thermal efficiency and effluent enthalpy are given as functions of feedstock flow for several arc power levels.

A strong emphasis has been placed on mechanical simplicity resulting in the capability to effect fast maintenance of low cost electrodes. Capital cost is shown to be much lower than other types of plasma generation equipment for large installations because no rectification or frequency conversion equipment is needed. Operating costs, including amortization of capital investment, are given for several operating conditions.

# Oxidation of Carbon in Porous Solids

C. Y. Wen and S. C. Wang

Dept. of Chemical Engineering, West Virginia University  
Morgantown, West Virginia

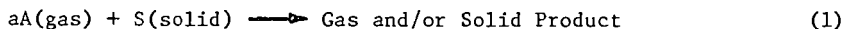
Noncatalytic solid-gas reaction systems are of great industrial importance and are found in daily use in chemical and metallurgical industries. Important examples are combustion of carbonaceous matters and regeneration of carbon-deposited catalysts by oxidation in air.

Weisz and Goodwin (7) observed, in the regeneration of catalysts at temperatures below 450°C, that the carbon burn-off is uniform (or "homogeneous") throughout the catalyst. At temperatures above 600°C, however, the burn-off is of "shell-progressive" or "unreacted-core-shrinking" type, as shown schematically in Figure 1.

Theoretical investigations have been undertaken previously to study the effect of heat and mass transfer processes on the overall rate of a noncatalytic solid-gas reaction occurring in a single solid pellet (4, 5, 8, 9). Phenomenological, rather than mechanistic, approach was adopted in analyzing these complex processes so that the effect of individual processes on the overall rate could be identified. The applicability and limitation of the "unreacted-core-shrinking" and "homogeneous" models were also presented, and the interrelationship between the two models was discussed. The concept of "effectiveness factor" frequently used in the studies of catalysis was extended to noncatalytic solid-gas reaction systems.

The purpose of the present experimental work is to verify the theoretical prediction of the existences of geometrical and thermal instabilities and the transition of the rate-controlling steps (ignition or extinction), which occur in a single particle-gas reaction describable by the unreacted-core-shrinking model.

Consider the simple case of solid-gas reaction taking place on the unreacted core surface:



The rate of reaction for gas component A,  $r_A$ , and for solid reactant S,  $r_S$ , can be represented as

$$r_A = a r_S = -a k_s C_S^m C_A^n$$

The above simplified rate equation will be used in view of the difficulty in obtaining a correct mechanism. As long as the rate equations fit the experimental data satisfactorily, the simple rate equations will provide an adequate analysis of overall characteristics of the reaction system provided no extrapolation beyond the range investigated is allowed.

Based on the unreacted-core-shrinking model as shown in Figure 1, and a constant particle size during an irreversible chemical reaction, a pseudo-steady-state material balance for the reactant component A within the inert solid product layer of the particle can be written as:

$$\nabla \cdot (CD_{eA} \nabla x_A) = (1/r^2)(\partial/\partial r)(r^2 CD_{eA} \partial x_A / \partial r) = 0, \quad r_c < r < R$$

If the ideal-gas law holds for the gaseous phase, i.e.,  $C = P/RT$ , then at a constant total pressure  $P$ ,  $C \propto 1/T$ . The effective diffusivity,  $D_{eA}$ , may be considered to be proportional to  $T^{1.5 \sim 2.0}$  in the molecular diffusion regime, and to  $T^{0.5}$  in the Knudsen diffusion regime. For convenience,  $D_{eA}$  may be taken to be roughly proportional to  $T^{1.0}$  considering the possibility of both types of diffusion through the porous product layer. Therefore, the product  $CD_{eA}$  becomes proportional to  $T^0$ , that is temperature independent. It should be noted, however, that  $C$  or  $D_{eA}$  itself alone is affected by temperature variation. With these simplifications, the last equation now becomes

$$\frac{d^2 x_A}{dr^2} + \frac{2}{r} \frac{dx_A}{dr} = 0 \quad r_c < r < R \quad (2)$$

The boundary conditions for Equation (2) are



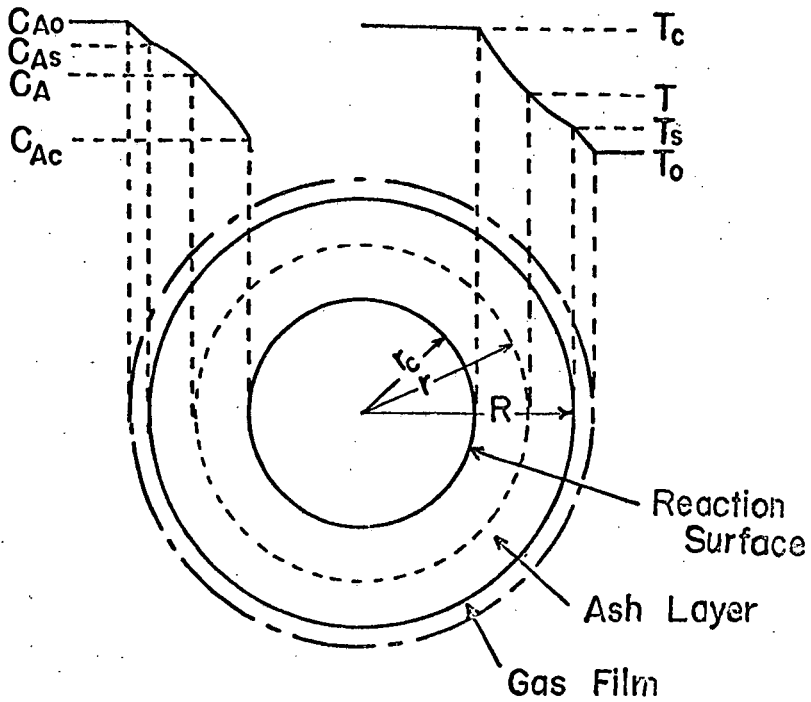


Fig. 1 Concentration and temperature profiles of a single particle-gas reaction indicating the three resistances in series.

$$r = R; (CD_{eA})_{T_0} \left. \frac{dx_A}{dr} \right|_{r=R} = (k_{mA}C)_{T_0} (x_{Ao} - x_{As}) \quad (3)$$

$$r = r_c; (CD_{eA})_{T_0} \left. \frac{dx_A}{dr} \right|_{r=r_c} = a k_{s(T_c)} C_{So}^m C_{Ac}^n \quad (4)$$

$$r = r_c; -(CD_{eA})_{T_0} \left. \frac{dx_A}{dr} \right|_{r=r_c} = a C_{So} \frac{dr}{dt} \quad (5)$$

where the subscripts  $T_0$  and  $T_c$  indicate the quantity to be evaluated at temperatures of bulk gas and reaction interface, respectively. The initial condition is

$$t = 0; r_c = R \quad (6)$$

For a particle with uniform distribution of solid reactant, the solid concentration,  $C_{So}$ , can be considered a constant at the surface of reaction, and therefore the reaction rate considered here is of the  $n$ -th order with respect to the concentration of gas component A.

Although equimolar counter-diffusion is assumed in deriving Equation (2), the application may be extended to non-equimolar cases when there is no significant volume change of gas or when concentrations of reactant and product gases are very dilute.

The heat balance in the ash layer is given by

$$\frac{\partial T}{\partial t} = \frac{k_e}{C_{pe}} \left( \frac{\partial^2 T}{\partial r^2} + \frac{2}{r} \frac{\partial T}{\partial r} \right) \quad r_c < r < R \quad (7)$$

The boundary conditions are

$$r = R; -k_e \left. \frac{\partial T}{\partial r} \right|_{r=R} = h_c (T_s - T_o) + h_R (T_s^4 - T_w^4) \quad (8)$$

$$r = r_c; 4\pi r_c^2 a k_{s(T_c)} C_{So}^m C_{Ac}^n (-\Delta H) + 4\pi r_c^2 k_e \left. \frac{\partial T}{\partial r} \right|_{r=r_c} = \frac{4}{3} \pi r_c^3 \rho_c C_{pc} \frac{dT_c}{dt} \quad (9)$$

The initial condition is

$$t = 0; T = T_c = T_i \quad (10)$$

In Equation (9), it is assumed that the temperature within the unreacted core is uniform at  $T_c$ . The temperature dependency of the reaction rate constant is assumed to be of Arrhenius' type:

$$k_{s(T_c)} = k_s^0 \exp(-E/RT_c) \quad (11)$$

The effectiveness factor is defined as (4,5)

$$\eta_s = \frac{\text{Actual (overall) reaction rate}}{\text{Reaction rate obtainable when the reaction site is exposed to the gas concentration and temperature of the bulk gas phase}}$$

Thus,

$$\eta_s = \frac{4\pi r_c^2 a k_{s(T_c)} C_{So}^m C_{Ac}^n}{4\pi r_c^2 a k_{s(T_o)} C_{So}^m C_{Ao}^n} = \frac{k_{s(T_c)} C_{Ac}^n}{k_{s(T_o)} C_{Ao}^n} = \left( \frac{W_c}{U_c} \right)^n \exp \left[ \frac{E}{RT_o} \left( 1 - \frac{1}{U_c} \right) \right] \quad (12)$$

or, by Equations (4) and (5),

$$\eta_s = - \frac{d\xi_c}{d\theta} \quad (13)$$

Equation (13) is true for all cases including those under isothermal situations.

Equations (2) through (10) are to be solved simultaneously by a numerical method. However, even for the simplest cases of pure heat transfer with moving

boundary, numerical methods are generally difficult and complicated. Therefore, some simplifying assumption seems warranted if there is no great sacrifice in accuracy in the final results. This can be accomplished by assuming  $\partial T/\partial t = 0$  in Equation (7). However, such a pseudo-steady-state assumption could lead to errors as well as unreasonable instantaneous temperature changes (5,8,9). These situations can be compensated for by introducing a simple energy accumulation term into the heat balance equation for the ash layer. For this purpose, the temperature distribution in the ash layer can be approximated at all times by a steady state profile (1):

$$T = T_c + (T_s - T_c) \left( \frac{1}{r_c} - \frac{1}{r} \right) / \left( \frac{1}{r_c} - \frac{1}{R} \right) \quad (14)$$

The accumulation of energy in ash layer is

$$\text{acc.} = \int_{r_c}^R 4\pi r^2 \rho_c \frac{\partial T}{\partial t} dr = 4\pi \rho_c \left( \frac{dT}{dt} \int_{r_c}^R r^2 dr + r_c^2 T \frac{dr_c}{dt} \right) \quad (15)$$

The integral in the last equation can now be evaluated using Equation (14). The accumulation in the ash layer can also be expressed as

$$\text{acc.} = -4\pi r_c^2 k_e \frac{\partial T}{\partial r} \Big|_{r=r_c} + 4\pi R^2 k_e \frac{\partial T}{\partial r} \Big|_{r=R} \quad (16)$$

The heat flux terms in Equation (16) can be obtained from Equations (8) and (9). Upon equating Equations (15) and (16) and simplifying, we obtain

$$\begin{aligned} a k_s(T_c) C_{So}^m C_{Ac}^n (-\Delta H) \xi_c^2 - [h_c(T_s - T_o) + h_R(T_s^4 - T_w^4)] = (R/3)(\rho_c C_{pc} - C_{pe}) \xi_c^3 \frac{dT_c}{dt} + \\ (R/3) C_{pe} \frac{d}{dt} \left[ T_c + (T_s - T_c) \cdot \frac{2-3\xi_c + \xi_c^3}{2(1-\xi_c)} \right] \end{aligned} \quad (17)$$

With some additional mathematical manipulations, we obtain a final set of equations, Equations (17) through (23), which replace Equations (2) through (10).

$$\theta = 0; \quad \xi_c = 1 \quad (18)$$

$$\theta = 0; \quad U_c = U_1 \quad (19)$$

$$W_c = W_s + N_{Sh} (1 - 1/\xi_c) (1 - W_s) \quad (20)$$

$$\frac{N_{Sh} (1 - W_s)}{\phi_s \xi_c^2} = \left( \frac{W_c}{U_c} \right)^n \exp \left[ (E/RT_o) (1 - 1/U_c) \right] = \eta_s \quad (21)$$

$$\frac{N_{Sh} (1 - W_s)}{\phi_s \xi_c^2} = - \frac{d\xi_c}{d\theta} = \eta_s \quad (22)$$

$$U_s = U_c + (1 - 1/\xi_c) [(N_{Nu})_C (U_s - 1) + (N_{Nu})_R (U_s^4 - U_w^4)] \quad (23)$$

Equations (17) through (23) are a set of algebraic and ordinary differential equations, which can be solved easily by a numerical method.

When complete steady-state is assumed, there is no energy accumulation in the ash layer ( $A = 0$ ) and in the unreacted core ( $G = 0$ ). In this case it can be shown that Equations (17) through (23) reduce to

$$\eta_s = \frac{(N_{Nu})_C (U_s - 1) + (N_{Nu})_R (U_s^4 - U_w^4)}{\beta \phi_s (E/RT_o) \xi_c^2} \quad (24)$$

and

$$\frac{Y}{\beta \phi_s \left( \frac{E}{RT_o} \right) \xi_c^2} = \left[ \frac{1 - \frac{1}{N_{Sh}} + \frac{1}{\xi_c} - 1}{1 - \frac{(E/RT_o)/\beta}{U_s - \left( 1 - \frac{1}{\xi_c} \right) \cdot Y}} \cdot Y \right]^n \cdot \exp \left\{ (E/RT_o) \left( 1 - \frac{1}{U_s - \left( 1 - \frac{1}{\xi_c} \right) \cdot Y} \right) \right\} \quad (25)$$

where

$$Y = (N_{Nu})_C (U_s - 1) + (N_{Nu})_R (U_s^4 - U_w^4)$$

Existence of three roots for  $U_s$  at a fixed  $\xi_c$  is possible for equation (25).

Figures 2 and 3 show the plots of effectiveness factor vs. fractional solid reactant conversion, and compare unsteady-state heat transfer analysis to that of pseudo-steady-state. The solid lines in these figures are unsteady-state solutions of Equations (17)-(23) obtained by numerical method. The dashed and dotted lines represent stable and metastable solutions, respectively, of Equations (24) and (25) for the pseudo-steady-state case ( $A = 0$ ,  $G = 0$ ). Multiple solutions for  $\eta_s$  are possible for Equations (24) and (25) at a fixed  $X$ , as shown.

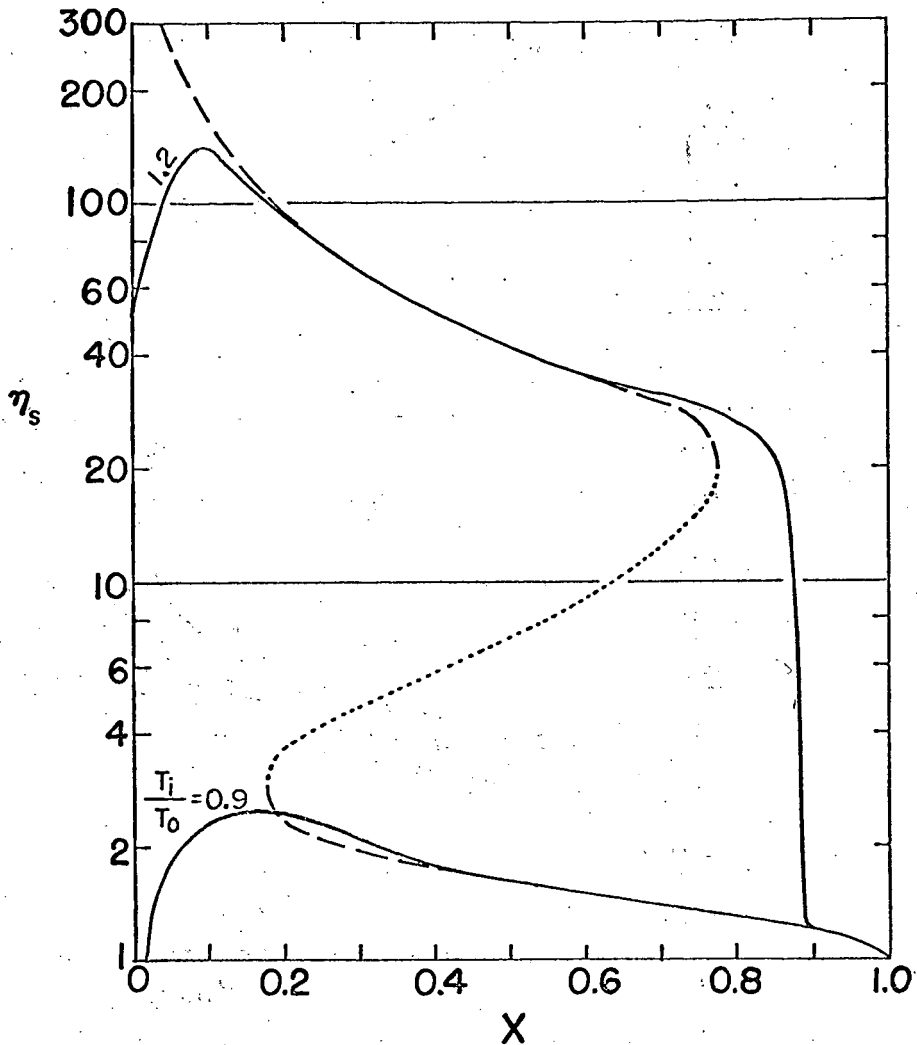
Figure 2 indicates a case in which the pseudo-steady-state analysis could lead to an erroneous conclusion. The chemical-reaction-controlling region would have never been realized if the pseudo-steady-state analysis had been used. The unsteady-state analysis on the other hand shows that chemical reaction could be rate-controlling when the initial temperature of the particle is sufficiently low ( $U_i = 0.90$ ). Figure 3 depicts the effect of heat capacity of unreacted core and heat of reaction on the thermal instability. The occurrence of thermal instability is less likely when the heat capacity is high.

Figure 4 illustrates an example of experimental result, which is computed based on the unreacted-core-shrinking model. The corresponding solutions obtained from Equations (17)-(23) (solid line) and from Equations (24) and (25) (dashed and dotted lines) are also shown in the figure for comparison. The experiment was performed in a thermobalance by burning a single solid sphere in a stream of heated air. The solid pellet was prepared by mixing a desired proportion of activated charcoal with aluminum oxide that serves as an inert porous medium. Waterglass (sodium silicate) diluted with a proper amount of water was used as a binder in forming the pellets. The particle was heated at 700°C in an inert atmosphere prior to the combustion test to remove moisture and to insure no weight loss owing to inert solid during the test. "Extinction" occurred at about 85 percent of solid conversion. The unsteady-state heat transfer analysis (solid line) describes more closely the experimental result than the pseudo-steady-state (dashed line) at the initial stage and during the transition from diffusion- to chemical-reaction-controlled regime. The values of effective diffusivity (6) and effective thermal conductivity (3) are estimated based on empirical correlations. The activation energy and surface rate constant are calculated from a correlation obtained by Field, et al (2) based on data of various investigators. In view of the wide variety of data reported in the literature for the oxidation of carbon, these values are believed to be good estimates for this purpose. The point to be emphasized here is that it is possible to predict the approximate reaction path of a solid-gas reaction from the estimated values of physical and chemical properties.

In general, it was found that most of the characteristic behavior from theoretical predictions are verifiable by the experimental observation. The phenomena of geometrical and thermal instabilities of reacting solid are experimentally verified. The reaction path is easily followed by plotting the effectiveness factor (or rate per unit area of reaction interface) versus solid conversion. Ignition and extinction are also observed under certain conditions agreeing, at least qualitatively, with the theory.

#### NOTATIONS

a	stoichiometric coefficient
A	$C_{Ao}^D e^{A(T_o)} C_{Pe} / a C_{So}^k e$



$$\beta = 0.005$$

$$\phi_s = 0.139$$

$$A = 0$$

$$N_{Sh} = 100$$

$$(N_{Nu})_C = 1$$

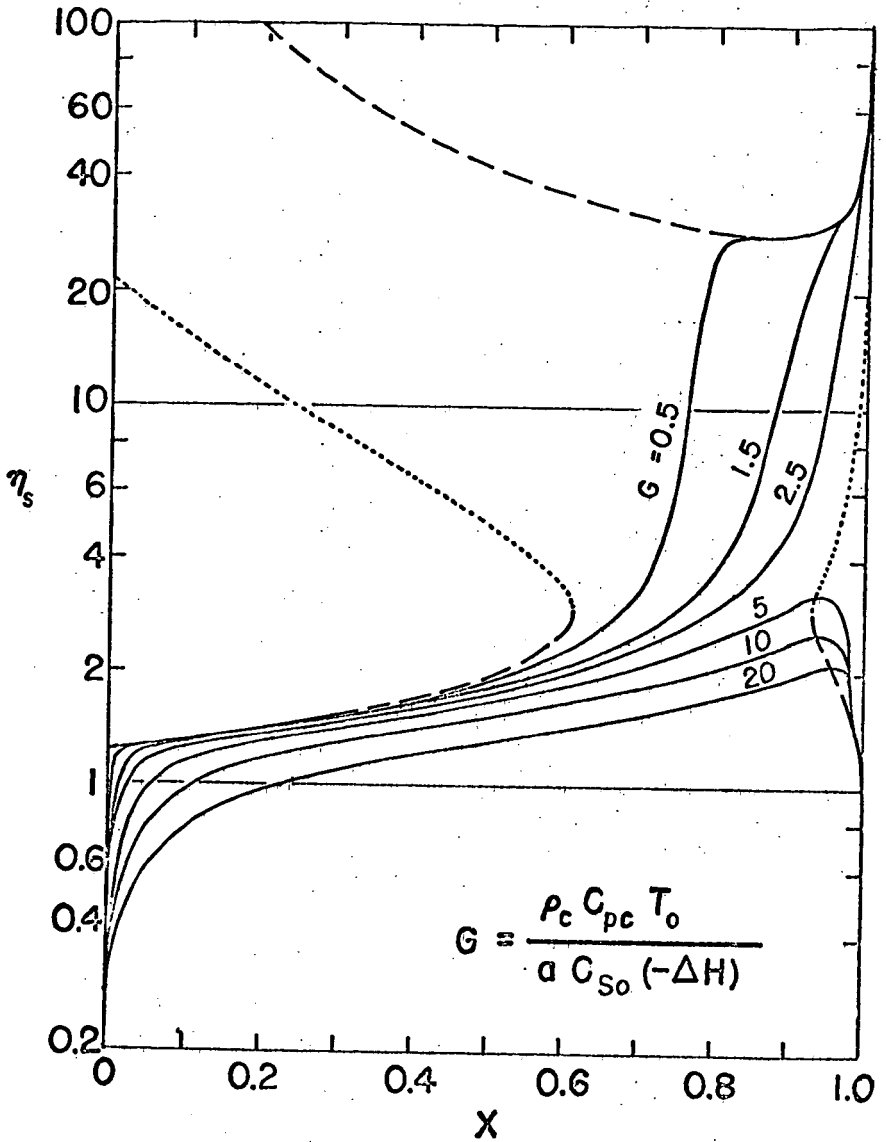
$$(N_{Nu})_R = 0$$

$$\frac{E}{R T_0} = 25$$

$$n = 1$$

$$G = 0.5$$

Fig.2 An Example Showing the Difference between Steady and Unsteady State Analysis



$$\beta = 0.02$$

$$\phi_s = 0.139$$

$$A = 0$$

$$N_{Sh} = 100$$

$$(N_{Nu})_C = 10$$

$$(N_{Nu})_R = 0$$

$$\frac{E}{R T_0} = 25$$

$$n = 1$$

$$\frac{T_i}{T_0} = 0.95$$

Fig.3 The Effect of Heat of Reaction and Heat Capacity of Unreacted Core on Thermal Instability in Terms of  $G$ .

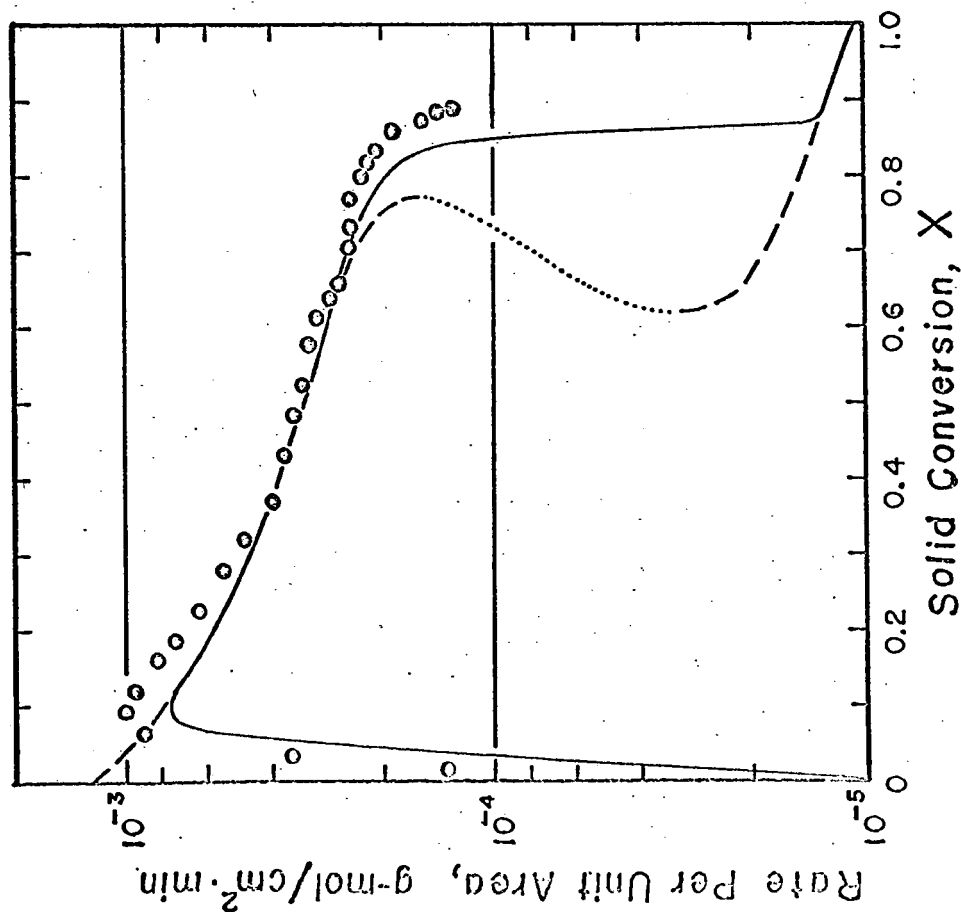


Fig.4 Comparison of Experimental Result and Computer Simulation for Oxidation of Carbon in Porous Solid, Using Unreacted-Core-Shrinking Model

$$T_o = 442^{\circ}\text{C}$$

$$T_w = 573^{\circ}\text{C}$$

$$T_i = 27^{\circ}\text{C}$$

$$N_{Re} = 393$$

$$R = 1.244 \text{ cm}$$

$$C_{S0} = 0.0225 \text{ g-mol/cm}^3$$

$$\epsilon = 0.556$$

$$DeA = 0.321 \text{ cm}^2/\text{sec}$$

$$k_e = 0.0032 \text{ cal/sec}\cdot\text{cm}\cdot^{\circ}\text{C}$$

$$E = 35,700 \text{ cal/g-mol}$$

$$k_{s(T_o)} = 5.16 \times 10^{-4} \text{ cm/sec}$$

C	total concentration of gases, mole/L <sup>3</sup>
C <sub>A</sub>	concentration of species A, C <sub>Ac</sub> at unreacted-core surface, C <sub>Ao</sub> in bulk gas phase, C <sub>As</sub> at outer surface of particle, mole/L <sup>3</sup>
C <sub>S</sub>	concentration of solid reactant S, C <sub>So</sub> initial concentration, mole/L <sup>3</sup>
C <sub>pc</sub>	heat capacity of unreacted core, H/MT
C <sub>pe</sub>	volumetric heat capacity of ash layer, H/L <sup>3</sup> T
D <sub>eA</sub>	effective diffusivity of gaseous component A in ash layer, L <sup>2</sup> /θ
E	activation energy of reaction rate constant, H/mole
G	$\rho_c C_{pc} T_o / a C_{So} (-\Delta H)$ , ratio of enthalpy of unreacted core to heat of reaction
h <sub>C</sub>	convective heat transfer coefficient, H/L <sup>2</sup> θ T
h <sub>R</sub>	radiational heat transfer coefficient, H/L <sup>2</sup> θ T <sup>4</sup>
ΔH	heat of reaction per mole of gaseous reactant, H/mole
k <sub>e</sub>	effective thermal conductivity of ash layer, H/Lθ T
k <sub>mA</sub>	mass transfer coefficient of component A across gas film, L/θ
k <sub>s</sub>	surface reaction rate constant based on solid reactant, L <sup>3(m+n)-2/mole<sup>m+n-1</sup>θ</sup>
k <sub>s</sub> <sup>o</sup>	frequency factor for rate constant, L <sup>3(m+n)-2/mole<sup>m+n-1</sup>θ</sup>
m	order of reaction for solid reactant
n	order of reaction for gaseous reactant
(N <sub>Nu</sub> ) <sub>C</sub>	Rh <sub>C</sub> /k <sub>e</sub> , modified Nusselt number for convective heat transfer
(N <sub>Nu</sub> ) <sub>R</sub>	Rh <sub>R</sub> T <sub>o</sub> <sup>3</sup> /k <sub>e</sub> , modified Nusselt number for radiational heat transfer
N <sub>Re</sub>	particle Reynolds number
N <sub>Sh</sub>	Rk <sub>mA</sub> (T <sub>o</sub> )/D <sub>eA</sub> (T <sub>o</sub> ), modified Sherwood number
P	total pressure, F/L <sup>2</sup>
r	distance from center of sphere, L
r <sub>c</sub>	radius of unreacted core, L
r <sub>A</sub> , r <sub>S</sub>	surface reaction rates of gaseous reactant A and solid reactant S, respectively, mole/L <sup>2</sup> θ
R	particle radius, L
Q	gas constant, H/mole.T
t	time, θ
T	temperature, T <sub>c</sub> at unreacted-core surface, T <sub>i</sub> initial temperature of particle, T <sub>o</sub> at bulk gas phase, T <sub>s</sub> at outer surface of particle, T <sub>w</sub> at reactor wall, T
U	T/T <sub>o</sub>
U <sub>c</sub>	T <sub>c</sub> /T <sub>o</sub>
U <sub>i</sub>	T <sub>i</sub> /T <sub>o</sub>
U <sub>s</sub>	T <sub>s</sub> /T <sub>o</sub>
U <sub>w</sub>	T <sub>w</sub> /T <sub>o</sub>
W	x <sub>A</sub> /x <sub>Ao</sub> , W <sub>c</sub> = x <sub>Ac</sub> /x <sub>Ao</sub> , W <sub>s</sub> = x <sub>As</sub> /x <sub>Ao</sub>
x <sub>A</sub>	mole fraction of component A, x <sub>Ac</sub> at unreacted-core surface, x <sub>Ao</sub> in bulk gas phase, x <sub>As</sub> at outer surface of particle
X	1 - ξ <sub>c</sub> <sup>3</sup> , fractional conversion of solid reactant S
β	C <sub>Ao</sub> D <sub>eA</sub> (T <sub>o</sub> )(-ΔH)Q/k <sub>e</sub> E
ε	porosity of ash layer



$\eta_s$	effectiveness factor
$\theta$	$k_s(T_o) C_{Ao}^n C_{So}^{m-1} t/R$
$\xi$	$r/R$
$\xi_c$	$r_c/R$
$\rho_c$	density of unreacted core, M/L <sup>3</sup>
$\phi_s$	$a R k_s(T_o) C_{Ao}^{n-1} C_{So}^m / D_{eA}(T_o)$

#### LITERATURE CITED

1. Beveridge, G. S. G., and Goldie, P. J., Chem. Eng. Sci., 23, 913 (1968).
2. Field, M. A., Gill, D. W., Morgan, B. B. and Hawksley, P. G. W., COMBUSTION OF PULVERISED COAL, The British Coal Utilisation Research Association, Leatherhead, Surrey, England (1967).
3. Franci, J. and Kingery, W. D., Am. Ceramic Soc. Journal, 37, 99 (1954).
4. Ishida, M. and Wen, C. Y., A.I.Ch.E. Journal, 14, 311 (1968).
5. Ishida, M. and Wen, C. Y., Chem. Eng. Sci., 23, 125 (1968).
6. Satterfield, C. N. and Sherwood, T. K., THE ROLE OF DIFFUSION IN CATALYSIS, Addison-Wesley, Reading, Mass. (1963).
7. Weisz, P. B. and Goodwin, R. D., J. Catalysis, 2, 397 (1963).
8. Wen, C. Y., Ind. Eng. Chem., 60, No. 9, 34 (1968).
9. Wen, C. Y., and Wang, S. C., "Thermal and Diffusional Effects in Noncatalytic Solid Gas Reactions", to appear in Ind. Eng. Chem., July, 1970 issue.

## Mass Spectrometric Volatilization Studies of Oil Shale

S. J. Steck, D. W. Muenow, and J. L. Margrave

Department of Chemistry  
Rice University  
Houston, Texas 77001

Utilization of oil shale as a fuel is a two-fold problem for high temperature chemistry: controlled pyrolysis of organic material, and high temperature sublimation-decomposition reactions of inorganic residues. Because shale differs from petroleum, in that nature's decomposition of the organic matter "kerogen" is incomplete, a vast technology of the conditions<sup>1,4</sup> (e.g., pressure, steam, air, and temperature) for the destructive distillation of kerogen has evolved. Realization of the disposal problem associated with the inorganic residues has also been the impetus for numerable technical studies<sup>1,4</sup> concerned with the effective use of inorganic silicates, carbonates, sulfates, phosphides, etc. found to be present in the shale.

High temperature mass spectrometry has been effectively used for both hydrocarbon studies<sup>5,6</sup> and numerous inorganic vaporization studies.<sup>7,8</sup> While the technique provides direct detection without condensation or possible intermediate reactions of the volatilized species, it is usually limited by the medium mass resolution of the spectrometers and complex introduced mixtures which do not permit unambiguous identification of specific hydrocarbons present. Nevertheless, qualitative and semi-quantitative estimates regarding the types of organic compounds evolved can be made because various functional groups of organic compounds lead to characteristic common ions in the mass spectra.<sup>6,9,10</sup> This technique has recently been applied to a similar problem of compounds found to be present in predominantly inorganic materials such as tektites, meteorites and natural glasses.<sup>10</sup>

## Experimental

Samples (approx. 0.1 g) of Colorado oil shale were vaporized from tantalum Knudsen cells (with boron nitride and high purity alumina crucible liners) into both a Bendix, model 14-206A, time-of-flight mass spectrometer and a 60° magnetic sector field instrument. The crucibles were resistively heated to temperatures of approximately 700°C; higher temperatures were obtained by electron bombardment of the cells. Temperatures were measured with a Pt-Pt-10% Rh thermocouple peened into the base of the cell. A movable beam-defining slit "shutter", located between the furnace and ion source regions of the spectrometer, permitted differentiation of molecular species arising in the reactor from residual background gases in the instrument. Ions were monitored at 20 and 40 eV and the spectra scanned at pressures of  $\sim 1 \times 10^{-6}$  torr in the ion source region. Mass spectra were monitored at selected time intervals with strip chart recorders during the heating cycle period. Continual oscillographic display of the spectra provided by the time-of-flight instrument insured that significant changes due to the evolution of trapped gases would not go unobserved.

## Results and Discussion

Ions up to  $\sim 400$  amu were monitored between room temperature and 1250°C. Neutral molecular progenitors of these ions have been assigned on the basis of mass-to-charge ratios, common fragment ions,<sup>6,9,10</sup> isotopic abundance, shutter profiles, and appearance potentials.

Over the temperature range investigated, the observed mass spectra suggest three distinct regions of volatility: (1) room temperature to  $\sim 350^\circ\text{C}$ , where only small amounts of hydrocarbons are evolved, (2)  $350\text{--}450^\circ\text{C}$  where large quantities of organic material are being released and (3) above  $450^\circ\text{C}$  for which inorganic species

are generally the most significant. The mass spectra reproduced in figures 2-4 are typical of these three categories; a background (room temperature) spectrum in figure 1 may be used for comparison. All four spectra were taken at 20 eV electron energy and have some ions that were off-scale with the sensitivity used.

#### Temperature range 25-350°C

Room temperature spectra obtained with mass spectrometers have characteristic residual peaks resulting primarily from pump fluids, air leaks, and condensation of various gases. Figure 1 shows such a spectrum obtained on the magnetic sector instrument. Nearly all ions attributed to pumping fluids (31, 108, 135, 169, 198-204) become smaller with heating as can be observed by comparison with figure 2. The scan at 160°C (figure 2) shows some significant changes in the hydrocarbon "envelopes"<sup>6,10</sup> which correspond to different numbers of carbon atoms in the fragment ions. Since comparison of numerous spectra of organic compounds indicates that those with different levels of unsaturation or functional groups frequently give different characteristic ions, the change between figures 1 and 2 is indicative of a change in the hydrocarbon species present. Monitoring several of these ions (m/e 78, 92, 106, 111, 159) with the shutter indicated they arose from the sample; thus at temperatures below 200°C, principal ions of aromatic (m/e 78, benzene; 92, toluene; 106, xylene) or hetero-aromatic (78, 92, 106 pyridyl; 111, thiophenes) molecules are released from the shale. At ~200°C an increase of ions characteristic to those of alkanes, alkene and alkynes suggest that a large variety of hydrocarbons are beginning to be released from the sample.

#### Temperature range 350-450°C

Ion intensities for most organic species increased by a factor of 10. A spectrum taken at 400°C (figure 3) shows the large characteristic hydrocarbon envelopes observed. In general, there is relatively little evidence for nitrogen or oxygen containing organics. A number of thiophenes but not mercaptans seem to be present. In addition to the organics, H<sub>2</sub>S (m/e 34), COS (m/e 60), and H<sub>2</sub>O also showed large shatterable increases. These sulfur-containing species eventually disappeared at lower temperatures and more quickly than did the hydrocarbons. As the temperature was increased in this range, a distinct trend towards greater unsaturation was observed; at 350°C, alkane common ions were the largest in the spectra but by 400°C, alkene ions were larger than the alkane fragments.

#### Temperature range 450-1250°C

Most hydrocarbons have been volatilized at these temperatures. A significant feature between 500-700°C is the gradual increase in the CO<sup>+</sup> ion intensity with a corresponding decrease in the CO<sub>2</sub><sup>+</sup> ion intensity. These molecules probably result from thermal decomposition of carbonates present in the shale matrix. At ~550°C, relative intensities of m/e 15-18 suggest that small amounts of ammonia were being evolved from the sample; evidence for release of this by-product of oil shale is generally missing from most of this series of mass spectra. At ~1000°C, Na<sup>+</sup> (m/e 23) and P<sub>2</sub><sup>+</sup> (m/e 62) were observed as significant, highly shatterable ions in the spectrum; at slightly higher temperatures, SiO<sub>2</sub><sup>+</sup> (m/e 60), Mg<sup>+</sup> (m/e 24) and Al<sup>+</sup> (m/e 27) were identified as well.

Sample residue of oil shale heated to 700°C retained their original shape but became black in color; a residue of shale heated to 1250°C changed to a dark, glassy bead.

In general, the results obtained in these studies agree with those found in previous oil shale technology. The most favorable temperature for hydrocarbon processing has been found to be 320°C. Greater unsaturation of the hydrocarbons with increasing temperature agrees with previous experimental work. The approximate 1% sulfur has been observed as thiophenes and H<sub>2</sub>S but not as mercaptans. In agreement with the small theoretical yield of nitrogen from Colorado oil shale, only small amounts of nitrogen-containing species can be identified in these experiments.

Fig. 1, 25°C



Fig. 2, 160°C

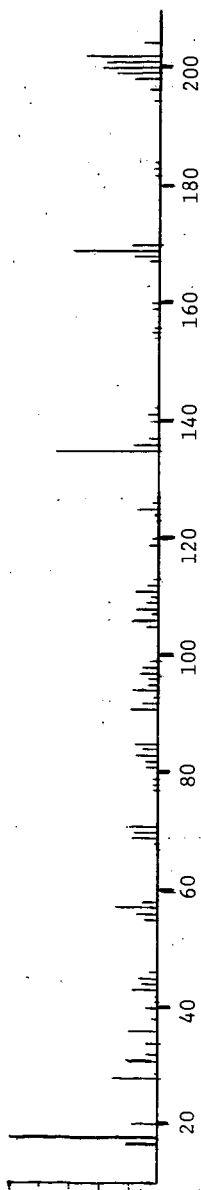


Fig. 3, 400°C (Scale 1/3)

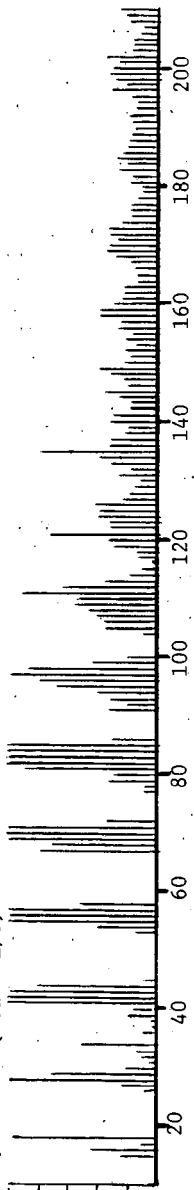
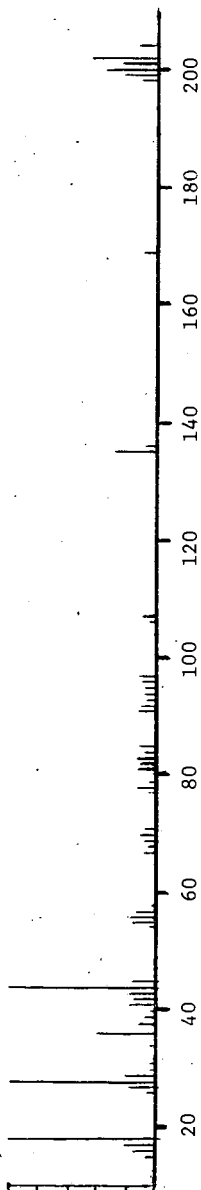


Fig. 4, 700°C



### Acknowledgments

This work was supported by the Robert A. Welch Foundation and the Atomic Energy Commission.

### References

<sup>1</sup>R. D. George, "Oil Shales of Colorado", Colorado Geological Survey Boulder, Bulletin 25, Denver, Colorado 1921.

<sup>2</sup>"Chemistry and Technology of Combustible Shales and Their Products," Leningrad, 1958, translated from Russian and published for the National Science Foundation, Washington, D. C. by the Israel Program for Scientific Translations, Jerusalem 1962.

<sup>3</sup>"Hydrocarbons from Oil Shale, Oil Sands, and Coal," John B. Jones, Jr., Ed., Chemical Engineering Progress Symposium Series, No. 54, Vol. 61, Am. Inst. of Chem. Engineers, New York, N. Y. 1965.

<sup>4</sup>"Utilization of Oil Shale," Dept. of Economic and Social Affairs, United Nations, New York, N. Y., 1967.

<sup>5</sup>W. A. Chupka, J. Berkowitz, D. J. Meschi, and H. A. Tasman, Advan. Mass Spectrometry, Proc. Conf. 2nd, Oxford, 1961, 99 (1963).

<sup>6</sup>S. J. Steck, G. A. Pressley, Jr., S-S. Lin and F. E. Stafford, J. Chem. Phys., 50, 3196 (1969).

<sup>7</sup>R. T. Grimley in "The Characterization of High Temperature Vapors", J. L. Margrave, Ed., John Wiley & Sons, New York, N. Y., 1967, p. 195.

<sup>8</sup>J. Drowart in "Condensation and Evaporation of Solids," E. Rutner, P. Goldfinger, and J. P. Hirth, Eds., Gordon and Breach, New York, N. Y., 1964, p. 255.

<sup>9</sup>F. W. McLafferty, "Interpretation of Mass Spectra," W. A. Benjamin, New York, N. Y., 1967.

<sup>10</sup>D. W. Muenow, S. J. Steck, and J. L. Margrave, "Mass Spectrometric Evidence for Organic Constituents in Tektites," to be published.

## RAPID THERMAL DECOMPOSITION OF BITUMINOUS COALS

Morris Mentser, Hugh J. O'Donnell and Sabri Ergun

Pittsburgh Energy Research Center, Bureau of Mines

U. S. Department of the Interior

4800 Forbes Avenue, Pittsburgh, Pennsylvania 15213

## INTRODUCTION

Pyrolysis studies of coals and chars have been pursued mainly with the objective of gaining knowledge about the kinetics of reaction processes involved in combustion and gasification. Slow heating studies are numerous,<sup>1/</sup> but they have little relevance to the combustion of pulverized fuel where the rate of temperature rise of fuel particles has been estimated at  $10^4$  °C/sec or more.<sup>2/</sup> Emphasis has therefore shifted to conditions of rapid heating.

In this study electrical pulse heating was employed to simulate the temperature transients experienced by fuel particles. The method combines the advantage of rapid heating with that of controlled energy input to the sample and a high probability for thermal equilibrium between sample and heat source. A constant heating rate of nearly  $10^4$  °C/sec was developed. The pulse heating technique has been used elsewhere<sup>3-4/</sup> for measurement of physical properties of conducting materials at high temperatures. Results are presented here on the devolatilization of a series of vitrains of different rank.

## EXPERIMENTAL

The procedure involved in these measurements consisted essentially of heating microgram quantities of coal by pulses of electrical current. The coal was contained in a cylinder of metallic screen which served as a resistance-heating element and at the same time retained the residue left after reaction. The yield of volatile products was determined from the weight loss of the coal sample after rapid heating.

Cylindrical screens, fabricated from 400-mesh, type 304, stainless steel wire cloth, were 6 cm long, 1.2 mm in diameter, and weighed 75 mg on average. When the screens were initially heated in vacuo, a significant weight loss occurred. Successive firings, however, produced no further weight changes. To eliminate this potential source of error, all screens were prefired at 900° C before determining their weights with a micro-balance.

Coal, having a particle size of 44-53  $\mu$ m, was introduced into the cylindrical screens, and the quantity of coal was determined by reweighing the screens. Typically, the amount of coal approximated 250  $\mu$ g. In some experiments, however, the coal charge was as small as 100  $\mu$ g or as large as 370  $\mu$ g. A correlation between quantity of coal sample and weight loss was sought, but none was found, and this result indicates that all of the coal samples reached thermal equilibrium with the heat source.

A cylindrical screen, containing coal, was clamped between electrodes, and the assembly was inserted into the vacuum system as shown in Figure 1. The pressure was reduced to 10-3 torr, and the system was then isolated from the pump. The screen was heated by an electrical current which was controlled to provide a constant time rate of increase of temperature. The circuit which controlled the current was designed to allow the current to increase as a function of time to compensate for the increase in resistance of the screen and the increase in radiant heat loss. In this mode of heating the increase in temperature of the screen was proportional to the length of time the current was applied.

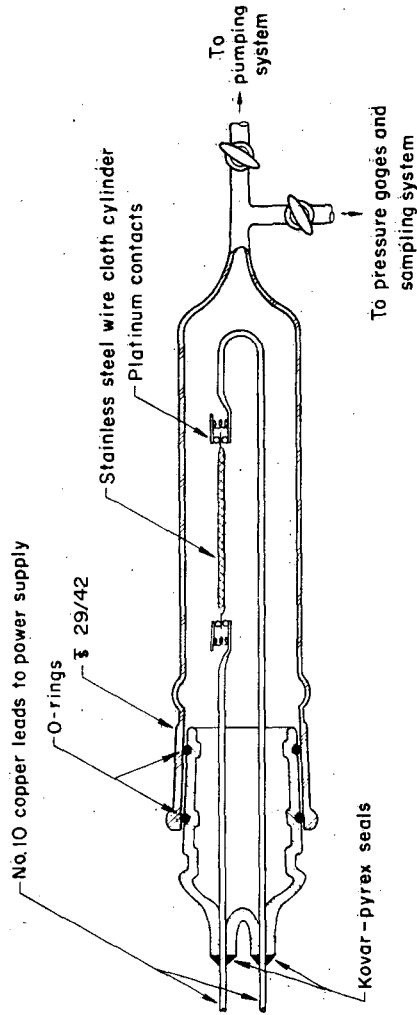


Figure 1—Thermal decomposition assembly

L-11666K

After firing, the screen with its residue from the reaction was removed from the system and reweighed. The resultant weight loss is a measure of the total volatile yield of gases and condensable products. The attendant pressure increase in the calibrated volume of the system is a measure of the gases evolved.

Calibration of screen temperature was accomplished by firing pure metals, comparable in weight and particle size to the coal samples, and observing the time required for them to melt. The condition of melting was determined by microscopic examination of the metal particles after heating. By this method the time to reach the melting point could not be pinpointed, but a time spread could be established for the extremes of complete melting and non-melting. The time spreads, indicated in Figure 2 for the different metals, amount to an uncertainty in temperature of at most  $\pm 70^\circ\text{C}$ . A line drawn through the mid-points of these time intervals corresponded to a constant heating rate of  $8.25 \times 10^3^\circ\text{C/sec}$ .

Proximate and ultimate analyses of the vitrains used in this study are presented in Table 1. The vitrains represent a wide range of volatile matter content, i.e., from 20.4 to 48.0 percent. The ash content has been kept low by careful selection of vitrain from the coal.

Table 1.--Analyses of vitrains

	Pocahontas No. 3 lvb	Pittsburgh hvAb	Illinois No. 2 hvcB
Proximate analysis (mf)			
Volatile matter	20.4	35.1	48.0
Fixed carbon	79.3	63.1	51.1
Ash	0.3	1.8	0.9
Ultimate analysis (maf)			
H	4.6	5.4	5.8
C	90.8	84.0	79.2
O	3.3	8.2	11.2
N	0.7	1.7	1.3
S	0.6	0.7	2.5

#### RESULTS AND DISCUSSION

Results of the decomposition of bituminous coals in the temperature region  $400\text{--}1160^\circ\text{C}$  are presented in Table 2 and graphed in Figure 3. The volatile yield or weight loss is the cumulative effect of reaction over an interval of rapidly changing temperature, and the temperatures designated in the table represent the maximum temperatures attained by the coal samples. The weight losses are averages of ten or more tests conducted at each temperature. Standard deviations indicated for the data points are larger than those generally obtained from physicochemical measurements on chemically pure materials. Lack of high precision was due to a number of factors: inhomogeneities in the coal itself; non-uniformities in the heating of the screens; and variability in the distribution of coal along the length of the cylinders.



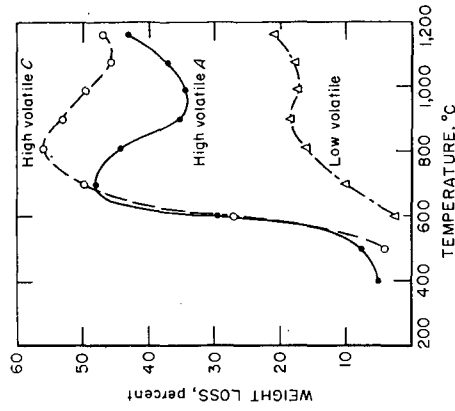


Figure 3 - Decomposition of vitrains from bituminous coals by rapid heating.

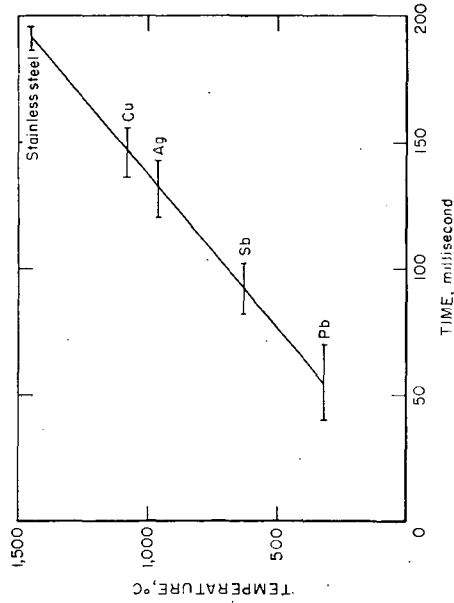


Figure 2 - Heating rate obtained by electrical pulse heating.

L-11660K

L-11691

Table 2.--Volatile yields from the decomposition of vitrains.

Temperature, °C	Weight loss, percent		
	Pocahontas No. 3, lvb	Pittsburgh, hvAb	Illinois No. 2, hvCb
400	--	4.9	--
500	0.0	7.6	4.1
600	2.4	29.4 ± 12	26.9 ± 8.2
700	10.0 ± 5.3	47.9 ± 3.2	49.7 ± 3.6
810	16.0 ± 2.3	44.1 ± 4.4	55.8 ± 1.6
900	18.5 ± 2.5	35.2 ± 4.8	53.0 ± 2.9
990	17.2 ± 1.4	34.5 ± 3.3	49.5 ± 3.4
1075	17.7 ± 2.1	37.1 ± 2.7	45.6 ± 2.5
1160	20.8 ± 1.9	43.1 ± 4.0	47.0 ± 1.9

The decomposition curves of Figure 3 obtained by heating vitrains at a rate of  $8.25 \times 10^3$  °C/sec, indicate that the release of volatiles is indeed rapid. Decomposition of hvC and hvA vitrains begins around 400° C as has been reported for slow heating studies of coal.<sup>5-6</sup> After the onset of reaction, volatile yields from the low rank coals quickly increase to a maximum in the region 700°-800° C. The maximum volatile yields are larger than the volatile matter of the coals determined by the standard ASTM method (Table 1), and in this respect our results are similar to those from other types of rapid heating studies.<sup>7-9</sup> With increase in temperature above 800°, there is a decrease in volatile yield to about the values given by proximate analysis. At 1160° C, which is the highest temperature attainable in this study, there is indication that the volatile yields from all coals are again trending upward.

The behavior of low volatile vitrain differs in some respects from that of the lower rank coals. Its threshold of reaction occurs at an elevated temperature of 600°. Its weight loss curve, although giving the appearance of a very weak peak at 900°, should most probably be construed as having reached a plateau in this region because the precision indices are too large to justify the existence of a real maximum.

The appearance of peaks in the weight loss curves from rapid heating is in marked contrast to the monotonic increase in weight loss that is observed when coal is devolatilized at a slow, constant heating rate.<sup>10</sup> A suggested explanation for the maxima in the weight loss curves of the low rank vitrains is that there is a competition between the bond-breaking reactions, which give rise to the initial decomposition products, and the recombination reactions, which cause initial products to form molecules more stable than the parent coal. Recently the idea of complex depolymerization and repolymerization reactions has been invoked to explain the ESR spectra of tars produced by the rapid pyrolysis of coal.<sup>11</sup>

Gases evolved during decomposition were measured by the pressure increase in the system. The moles of gas were converted to a weight basis by means of gas compositions reported in the literature,<sup>12</sup> and the amount of liquid or condensables was obtained by difference.

Table 3.--Dependence of gas-liquid composition of volatiles upon rank of vitrain.

Coal rank	Temperature °C	Coal weight μg	Total volatile yield		Gas yield		Liquid yield	
			μg	% of coal	μg	% of coal	μg	By diff. % of volatiles
Pocahontas No. 3 lvb	990	332	54	16	41	12	76	24
	900	282	46	16	33	12	72	28
Pittsburgh, hvAb	810	258	113	44	30	12	26	74
Illinois No. 2., hvCb	810	217	122	56	29	13	24	76

Gas and liquid yields corresponding to the maximum volatile yields from the coals are shown in Table 3. The gas yield in terms of  $\mu\text{g gas}/\mu\text{g coal}$  remains constant at about 12 percent, irrespective of the rank of the coal. At the same time the total yield of volatiles increased from 16 to 56 percent with decrease in coal rank. It is quite apparent, therefore, that the increased volatile yields obtained from the lower rank coals are due entirely to the increased formation of condensable products.

#### SUMMARY

Rapid pyrolysis of vitrains from bituminous coals was effected by heating them at a rate of  $8.25 \times 10^3$   $^{\circ}\text{C}/\text{sec}$ , and the extent of devolatilization was measured gravimetrically.

Yields of total volatiles from the low rank hvC and hvA coals do not increase monotonically with temperature, but instead reach a maximum in the temperature region  $700^{\circ}\text{--}800^{\circ}\text{C}$ . The peak volatile yields exceed the volatile matter contents of the coals that are determined by the standard ASTM method.

At temperatures above  $1100^{\circ}\text{C}$  there is evidence that the production of volatiles from all bituminous coals again increases with the temperature.

Low rank coals produce larger volatile yields than high rank coals. The increased yields are due almost entirely to increases in amounts of condensable reaction products.

#### ACKNOWLEDGMENT

The authors wish to thank A. R. Plantz and H. E. Butzert for the design and construction of the current control circuit, and A. F. Headrick for preparation of cylindrical screens.

#### REFERENCES

1. Yellow, P. C., BCURA Mon. Bull., 29, 285 (1965).
2. Field, M. A., Gill, D. W., Morgan, B. B. and Hawksley, P.G.W., BCURA Mon. Bull., 31, 193 (1967).
3. Taylor, R. E. and Finch, R. A., J. Less Common Metals, 6, 283 (1964).
4. Finch, R. A. and Taylor, R. E., Rev. Sci. Instr., 40, 1195 (1969).
5. Van Krevelen, D. W., Van Heerden, C. and Huntjens, F. J., Fuel, 30, 253 (1951).
6. Boyer, A. F., Compt. rend. 69th Congr. ind. gaz 1952, 653.
7. Eddinger, R. T., Friedman, L. D. and Rau, E., Fuel, 45, 245 (1966).
8. Loison, R. and Chauvin, R., Chim. Ind., 91, 269 (1964).
9. Kimber, G. M. and Gray, M. D., Combustion and Flame, 11, 350 (1967).
10. Van Krevelen, D. W., "Coal," Elsevier, Amsterdam, 1961, p. 266.
11. Chauvin, R., Chiche, P., Quinton, M. F. and Uebersfeld, J., Carbon, 7, 307 (1969).
12. Karn, F. S., Friedel, R. A. and Sharkey, A. G., Jr., Carbon, 5, 25 (1967).

## STUDIES OF THE SOLID AND GASEOUS PRODUCTS FROM LASER PYROLYSIS OF COAL

F. S. Karn, R. A. Friedel, and A. G. Sharkey, Jr.

Pittsburgh Energy Research Center, Bureau of Mines,  
U.S. Department of the Interior, Pittsburgh, Pa.

### INTRODUCTION

The Bureau of Mines has made an extensive effort to find new techniques to investigate the structural units in coal for both theoretical and practical purposes. One of the newer research tools is the laser, which can produce high temperatures accompanied by rapid heating and cooling. Although many of the products from laser irradiation have already been produced from coal by other high-temperature devices<sup>1-3/</sup>, the laser excels in the production of certain pyrolysis products.

### EXPERIMENTAL

Two lasers have been used in this study. A pulsed ruby laser with a focused beam gave an energy concentration of 55,000 watts  $\text{cm}^{-2}$  at a wavelength of 6943 Å.<sup>4/</sup> A continuous  $\text{CO}_2$  laser with a focused beam gave an energy output of 140 watts  $\text{cm}^{-2}$  at a wavelength of 106,000 Å.<sup>4/</sup>

The general irradiation procedure was to seal the coal sample in a glass vessel into which the laser beam can be fired. Coal samples, usually 8-mm cubes, were heated under vacuum to 100° C for 20 hours before sealing. Samples for the ruby laser were sealed in a pyrex tube under vacuum or under an inert gas at pressures up to 1 atmosphere. Pyrolysis occurred rapidly and both gaseous products and entrained solids escaped from the hot surface at a rate estimated at 11,000  $\text{cm sec}^{-1}$ .<sup>6/</sup> Samples pyrolyzed by the  $\text{CO}_2$  laser were irradiated in a tube with a sodium chloride window. Pyrolysis of these samples was a continuous process which could be observed for several minutes, at the end of which the coal sample was usually exhausted. The escape of the gaseous and solid products from the reaction zone of the  $\text{CO}_2$  laser was relatively slow, only 28  $\text{cm sec}^{-1}$ . Gases were collected in an evacuated bulb for analysis by mass spectrometry. An effort was made to accelerate the solid product out of the pyrolysis zone. Rapid removal of the solid was attempted by increasing the gas evacuation rate, flushing with inert gas, an electric discharge, and use of a refrigerated collection bulb.

### RESULTS

#### Ruby Laser

Coal-pyrolysis products using the ruby laser were 53 percent solid and 47 percent gas. No significant amounts of liquid were recovered, consistent with previous high-energy investigations.<sup>5/</sup> Gas composition data are summarized in table 1, where ruby-laser data are compared with gases from high-temperature coal carbonization, low-temperature carbonization, and pyrolysis with the  $\text{CO}_2$  laser.

The ruby laser produced an increase in acetylene and a decrease in methane and other hydrocarbons relative to gases from pyrolysis at lower temperatures.

Direct observation of pyrolysis with the ruby laser was impossible due to high light intensity and high rate of discharge. Photographic studies were reported previously;<sup>6/</sup> at 26,000 frames per second the movement of products out

of the reaction zone was observed. Gaseous products cooled quickly and were stable during their introduction into the ionizing chamber of the mass spectrometer. Solids, deposited on the tube walls, were easily removed. The unreacted portion of the sample was weighed for material balance calculations. The solid product was analyzed by infrared. An ultimate analysis of this solid was similar to the original coal (table 2).

The infrared spectrum indicated that most of the bands characteristic of the parent coal are missing.<sup>4/</sup> The high-resolution mass spectrum of the solid is similar to that of coal. It is probably not significant because some of the original coal was entrained in the rapidly expanding gas stream and mixed with the solid product. This is indicated by high ash in table 2.

### Carbon Dioxide Laser

Coal-pyrolysis products using the CO<sub>2</sub> laser were 29 percent gas and 71 percent solid. The only liquids observed were traces of pentane and hexane in the vapor phase. Typical gaseous products are summarized in column 3 of table 1. These gases seem to represent a transition between industrial coal carbonization and the rapid pyrolysis available with the ruby laser. The CO<sub>2</sub> laser produces a series of hydrocarbons, but not acetylene, which apparently requires higher temperatures than available.

Hot gases from the CO<sub>2</sub>-laser irradiation were passed through a bed of powdered Raney nickel catalyst.<sup>7/</sup> The catalyst was not heated directly but only indirectly, by incoming gases and by heats of reaction of the gases. The usual complex mixture of gases was converted into a simple mixture consisting of 91 percent methane, ethane, and propane (table 3). The low yields of hydrogen and carbon oxides indicate a gas synthesis reaction as well as hydrogenation occurred. The fuel value of the gas was increased from 698 Btu/ft<sup>3</sup> to 1325 Btu/ft<sup>3</sup> by the catalytic treatment.

### Solid Product from CO<sub>2</sub> Laser

The solid product from the CO<sub>2</sub>-laser pyrolysis evolved as a fine brown powder which was suspended in the reaction tube and slowly deposited on the tube walls. Exposure to the reflected radiation of the laser beam caused melting and condensation reactions which resulted in a tarry mass. Secondary heating could be prevented by intermittent laser operation or by removing the powder in a stream of inert gas.

The solid was removed from the walls of the collection vessel in the form of a powder which softened between 108° and 112° C and volatilized at 250° to 300° C. The apparent density of the freshly prepared solid was 0.033 g cm<sup>-3</sup>, only 2 percent of the density of the coal (table 4). In a closed tube the material remained stable for several months.

This solid was separated into three fractions by extracting with benzene at 80° C, evaporating the solvent, then extracting with hexane.<sup>8/</sup> The distribution was benzene-insoluble (36 percent), asphaltene or benzene-soluble and hexane-insoluble (26.7 percent), and hexane-soluble (37.3 percent). The average molecular weight of the benzene-soluble material is 396 by the osmotic method. In contrast with the 64 percent solubility of the laser solids Pittsburgh seam coal is less than 1 percent soluble in benzene at 80° C.

Since the solubility of coal is increased by reduction,<sup>9/</sup> the laser solids were dehydrogenated to determine if their solubility could be attributed to hydroaromatics. The sample was prepared by refluxing the laser solid in phen-

anthridine with a catalyst of palladium on calcium carbonate.<sup>10/</sup> Thirty percent of the total hydrogen was removed, decreasing the hydrogen to carbon ratio as follows:

	<u>H:C, atomic ratio</u>
Pittsburgh seam coal	0.81
Laser solids	0.90
Dehydrogenated laser solids	0.63

#### High-Resolution Mass Spectrometry

The mass spectrum of the laser solids was obtained using a Consolidated Electrodynamics Corp. model 21-110B high-resolution mass spectrometer at a source temperature of 300° C. The laser solids are identified as sample 1 in table 5. This spectrum was compared with the spectrum of sample 2, which represents a similar laser product separated by gel permeation chromatography into 52 fractions.<sup>11/</sup> The fractions were analyzed by the mass spectrometer and their qualitative analyses combined. Spectra for samples 3 and 4 represent the solid products obtained from Pittsburgh seam coal by other processes. Sample 3 is the composite of distillates from a high-temperature coal carbonization<sup>12/</sup> and sample 4 is a pyridine extract of Pittsburgh coal obtained by mechanical agitation at room temperature.<sup>13/</sup>

An inspection of table 5 shows that pyrolysis of coal using a CO<sub>2</sub> laser produces a complex product which includes naphthalenes, phenanthrenes, and pyrenes. Many of the methyl substituted homologs are present. The maximum molecular weight of sample 1 (laser solids volatilized into the mass spectrometer) was 440. Since this maximum molecular weight is only slightly higher than the value of 396 found for the average molecular weight by the osmotic method, it indicates that the sample residue (20 percent remained in the sample holder) contains higher molecular weight compounds. Sample 2 has a lower range of molecular weights because only the toluene-soluble portion of the laser sample was introduced.

#### SUMMARY

Products from the laser pyrolysis of coal are predominantly gases and solids. There is little evidence of tar and pitch which are characteristic of coal carbonization. Gases from the CO<sub>2</sub> laser have high fuel value following catalytic treatment. Solid products are a complex mixture having low-ash, low-density, and high-hydrogen content. Efforts were made to analyze these solids using solvation, dehydrogenation, gel permeation chromatography, and mass spectrometry. Coal pyrolysis using laser irradiation provides a variety of organic compounds.

1. High-energy laser irradiation, available from a pulsed ruby or other solid laser, produces simple gas mixtures which are high in hydrogen, acetylene, and carbon monoxide.

2. A moderate energy irradiation from a 10-watt CO<sub>2</sub> laser produces a more complex mixture of gases with little or no acetylene. The solid product has low density, is highly soluble in benzene, and has an ultimate analysis similar to that of an ash-free coal.

## REFERENCES

1. G. Kolling and D. Hausigk, Brennstoff-Chemie, No. 3, Mar. 1969, pp. 65-68. Trans. No. 3636, Scripta Technica, Inc.
2. B. D. Blaustein and Y. C. Fu, Advances in Chemistry Series, R. F. Gould, ed., Am. Chem. Soc., Washington, D. C., No. 80, p. 259 (1968).
3. W. R. Ladner, The British Coal Util. Res. Asso., Monthly Bull., v. 28, No. 7, July 1964, pp. 281-301.
4. F. S. Karn, A. G. Sharkey, Jr., A. F. Logar, and R. A. Friedel, Bureau of Mines Rept. of Inv. 7328, 1970, 32 pp.
5. T. Aust, W. R. Ladner, and G. I. T. McConnell, Sixth Inter'l Conf. on Coal Science, Munster, Germany, 1965, Sec. 7, pp. 1-15.
6. F. S. Karn and J. M. Singer, Fuel, v. 47, May 1968, pp. 235-240.
7. R. J. Kokes and P. H. Emmett, J. Am. Chem. Soc., v. 81, Oct. 5, 1959, pp. 5032-5037.
8. C. O. Hawk and R. W. Hiteshue, Bureau of Mines Bull. 622, 1965, 42 pp.
9. L. Reggel, C. Zahn, I. Wender, and R. Raymond, Bureau of Mines Bull. 615, 1965, 57 pp.
10. L. Reggel, I. Wender, and R. Raymond, Fuel, v. 48, Sept. 1968, pp. 373-389.
11. T. Edstrom and B. A. Petro, J. Polymer Science: Part C, No. 21, 1968, pp. 171-182.
12. J. L. Shultz, R. A. Friedel, and A. G. Sharkey, Jr., Bureau of Mines Rept. of Inv. 7000, 1967, 14 pp.
13. T. Kessler, R. Raymond, and A. G. Sharkey, Jr., Fuel, v. 48, April 1969, pp. 179-196.

Table 1.- Gas composition of pyrolysis products, mole percent

Pyrolysis method:	Ruby laser	CO <sub>2</sub> laser	High-temperature carbonization	Low-temperature carbonization
Estimated temperature, °C <sup>a/</sup>	1200	1000	900	500
H <sub>2</sub>	52	47	56	17
CO	22	9	7	3
CO <sub>2</sub>	9	2	0	5
CH <sub>4</sub>	5	21	31	73
C <sub>2</sub> H <sub>2</sub>	11	0	0	0
Other HC	0	20	5	2

<sup>a/</sup> Reference 4.



Table 2.- Elemental analyses of Pittsburgh seam coal and of pyrolysis solids

<u>Weight percent</u>	<u>Pittsburgh seam coal</u>	<u>Solid product</u>	
		<u>Ruby laser</u>	<u>CO<sub>2</sub> laser</u>
C	78.3	79.0	83.0
H	5.3	4.6	6.2
O,N,S	11.6	8.6	9.9
Ash	4.8	7.7	0.9
Atomic ratio, C/H	1.23	1.43	1.11
C/O	12.3	12.2	16.2

Table 3.- Irradiation of Pittsburgh seam coal with CO<sub>2</sub> laser. Gases exposed to Raney nickel

	<u>Direct pyrolysis</u>	<u>Gases over Raney nickel</u>
H <sub>2</sub> , mole percent	51	3
CO	10	2
CH <sub>4</sub>	23	60
C <sub>2</sub> H <sub>6</sub>	3	23
C <sub>3</sub> H <sub>8</sub>	1	8
CO <sub>2</sub>	2	0
Other hydrocarbons	10	4

Table 4.- Data for solid from CO<sub>2</sub>-laser irradiation of coal

Apparent density	0.033 g cm <sup>-3</sup>
Softening point	108° - 112° C
Volatilization temperature	250° - 300° C
Solubility in benzene	64 percent
Molecular weight, benzene-soluble fraction	396

Table 5.- Coal degradation products examined by mass spectrometry

Sample:	1 <sup>a</sup> /	2 <sup>b</sup> /	3 <sup>c</sup> /	4 <sup>d</sup> /
<u>Example of possible compound</u>				
Indene		116	116	
Indan		118	118	
C <sub>3</sub> alkyl benzene		120	120	
C <sub>2</sub> alkyl phenol	122	122	122	
Naphthalene		128	128	128
		130	130	130
	132	132	132	132
	134	134	134	134
	136	136	136	136
		138	138	138
		140		
Methylnaphthalene		142	142	
	144	144	144	
	146	146	146	
	148			
Acenaphthylene			152	152
Acenaphthene			154	154
C <sub>2</sub> alkyl naphthalene	156	156	156	
	160	160	160	
Fluorene			166	
Dibenzofuran			168	168
	170		170	
Anthracene	178	178	178	178
	180	180	180	
	182		182	
	184		184	
	186	186		
Methylphenanthrene	192	192	192	
Phenanthrol	194		194	
	196		196	
	198	198	198	
Pyrene	202		202	

Table 5.- Coal degradation products examined by mass spectrometry  
(cont'd)

Sample:	1a/	2b/	3c/	4d/
<u>Example of possible compound</u>				
Dimethylantracene	206	206	206	
	208		208	
	210	210	210	
	212	212	212	
	216	216	216	
	218	218	218	
	220	220	220	
	222		222	
	224		224	
Benzo[ghi]fluoranthene	226		226	226
Chrysene	228	228	228	228
	230	230	230	
	232		232	
	234	234	234	
	236		236	
	238		238	
	244	244	244	
	246		246	
	248	248	248	
	250		250	
Perylene	252		252	
	*		*	

\* Sample has additional mass peaks up to 440.

a/ Solids from CO<sub>2</sub> laser.

b/ Solids from CO<sub>2</sub> laser, dissolved in toluene and separated by gel permeation chromatography.

c/ Composite data from high-temperature coal carbonization, reference 12.

d/ Room-temperature pyridine extract, reference 13.

# IGNITION AND INCENDIVITY OF SINGLE MICRON SIZE MAGNESIUM PARTICLES IRRADIATED BY A LASER BEAM

Israel Liebman, John Corry and Henry E. Perlee

Theoretical Support, Safety Research Center, Bureau of Mines  
U. S. Department of the Interior, Pittsburgh, Pennsylvania

## INTRODUCTION

This paper describes an experimental study of the ignition and incendivity characteristics of magnesium particles heated by intense radiation. While many investigations have been concerned with determining ignition temperatures of metal particles, much of their work has been with the ignition of single particles by hot gases.<sup>(1,2,3)\*</sup> In dust or hybrid flames, however, a large portion of the particle ignition energy is supplied through radiation. Indeed, in a study of dust flames of aluminum and graphite,<sup>(4)</sup> the contribution of radiation was estimated to be 30 to 60 percent of the total ignition energy. The ignition of combustible gases by flying abrasion sparks and the incendivity of heated passive pellets shot into explosive gases have been examined by many investigators<sup>(5,6,7)</sup>; however, the relative motion between particles and environment complicates the analysis and interpretation. In the present study, single micron size magnesium particles were radiatively heated while suspended in quiescent cold environments of oxygen, air, He-oxygen, and methane-air mixtures, and the ignition and incandive mechanisms of the particles were examined.

## EXPERIMENTAL APPARATUS AND PROCEDURE

Figure 1 shows a schematic of the experimental apparatus. The laser used a 1.3-cm-diameter neodymium-doped glass rod and had a pulse duration of about 0.9 millisecond. The laser beam was collimated by a simple 17-cm-focal-length convex lens positioned 9.5 cm from the magnesium particle suspended in the center of the levitation device. Devices of this nature have been used by other investigators.<sup>(8)</sup> The levitator consisted of four 0.3-cm-diameter by 8-cm-long vertically mounted metal rods which formed a 1.4-cm square. The rod ends were supported by two teflon insulating disks; alternate rods were connected together and to a 200- to 1500-volt AC supply. Two metal circular plates attached to the inner face of the top and bottom teflon disks and insulated from the rods were connected to a DC source of 100 to 1000 volts. In practice several milligrams of the magnesium dust placed in a centrally located cavity in the bottom metal disk were dispersed in the apparatus by charging with a high-voltage pulse. A few of the scattered particles were captured in the levitation apparatus and retained along the central vertical axis of the device by the rotating electric field.

All particles but one were readily eliminated by varying the AC and DC potentials; the single remaining particle was then positioned in line with the laser beam and its size determined by use of a microscope. The levitator was contained in a transparent glass chamber 6 x 6 x 10 cm having two vents for use with flammable mixtures. In the experiments, single spherical magnesium particles (99 percent pure) ranging in size from 28- to 120-microns diameter were suspended and irradiated in the glass chamber after filling with dry gas mixtures of air, helium-20 percent oxygen, pure oxygen, pure argon and stoichiometric methane-air. Streak and high-speed framing cameras were used to photograph the particles during irradiation. In order to determine when particle ignition occurred, a sample of the laser beam was picked up by the photodiode (fig. 1) and amplified to energize

\* Underlined numbers in parentheses refer to references at the end of the paper.

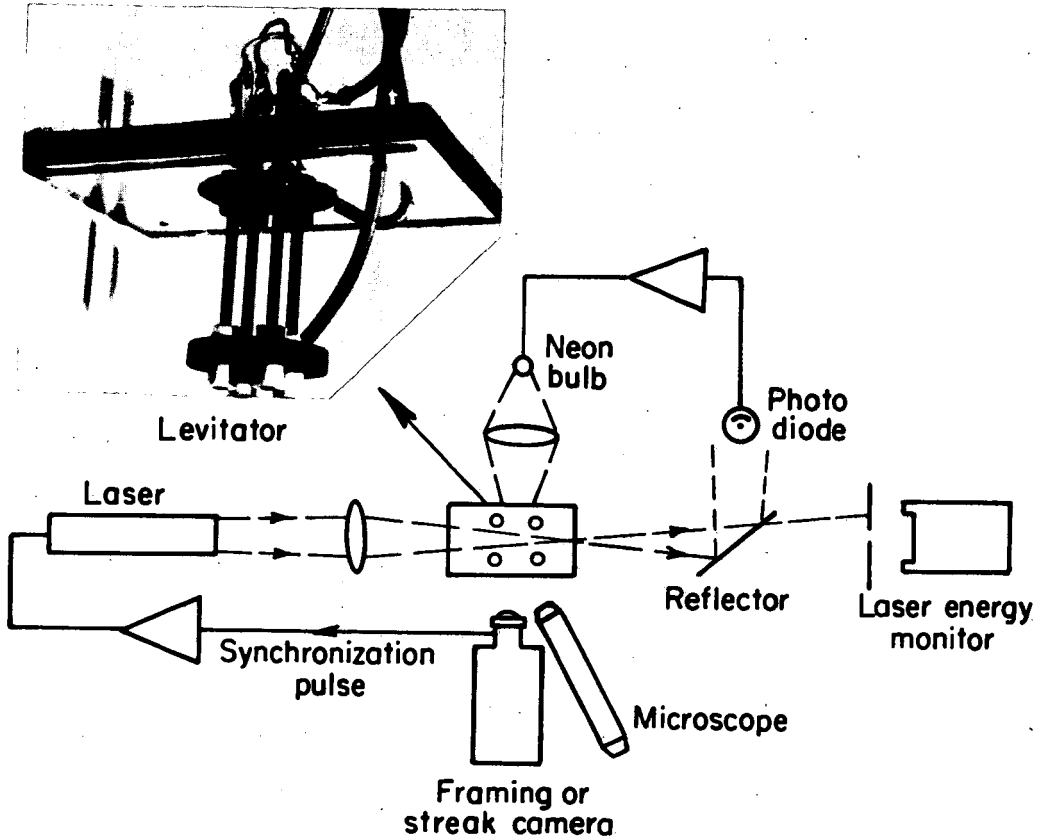


Fig. 1. - Apparatus for laser ignition of single magnesium particles.

a neon bulb whose focused image on the camera film correlated with the laser pulse. The laser pulse duration was measured by connecting the photodiode output to an oscilloscope. Due to the characteristic energy inhomogeneity in the laser beam cross-section, the magnesium particle was reproducibly positioned in a small, relatively uniform section of the laser beam and a 1-mm-diameter aperture in front of the laser energy monitor limited the measured energy to this uniform section. The monitor was a radiometer based on the calorimetric principle and measured total pulse energy passing through the apparatus. The collimating lens position was fixed and laser beam energy was varied by changing the charge voltage on the laser flash tube capacitor bank. Since the magnesium particle blocked a small portion of the laser beam, the laser energy was monitored between tests in the absence of a particle. The calculated laser power densities irradiating the particle were a function of the measured laser energy passing through the aperture, the aperture cross-section projected back to the particle site, and the pulse duration.

Schlieren photographs were taken during the irradiation of single magnesium particles (60- and 120-micron diameter) suspended in air, pure argon and stoichiometric methane-air mixtures. In the experimental arrangement shown in figure 2, a ruby laser having an approximate 0.9 millisecond length pulse was convenient to use for the radiation heating source. It was also advantageous to use the illustrated glass light guide to reflect a portion of the laser light on the film for time correlation of the irradiated particle with the laser pulse.

## RESULTS AND DISCUSSIONS

### Particle Ignition

In previous hot-gas ignition experiments of single magnesium particle in air, it was established that gas temperatures of 6400 to 7400°C are necessary for ignition of particles ranging in diameter from 120 to 20 microns, respectively(3); the observed gas temperature increase with decreasing particle size was attributed to the increased heat loss per particle surface area with decreasing particle diameter during the ignition process. In our experiments, the particle was initially surrounded by a cold gas; therefore, higher particle temperatures were necessary for ignition to compensate for the increased heat losses to the cold ambient atmosphere. In addition, maximum temperatures attained by a particle during irradiation by a short pulse depend on the particle heat capacity, thus requiring that the ignition energy supplied by the laser increase with particle size.

Figure 3 is a streak photograph of a laser-ignited, 84-micron-diameter magnesium particle burning in air. Particle spiraling during combustion, shown in this photograph, was frequently observed and is ascribed to preferential burning of the particle. In many cases the particle was seen to fragmentize following ignition. Burning lifetimes of the particles were usually much shorter than reported in the previous hot-gas ignition studies.

Figure 4 is a plot of our experimental data showing the laser beam power density required to ignite single magnesium particles suspended in various atmospheres. At these critical powers, ignition always occurred near the end of the laser pulse. As laser power was increased above the critical value, ignition delay time could be shortened appreciably. As expected, the radiant power for ignition increases with particle size and with increased thermal conductivity of the ambient gases (thermal conductivity of helium is approximately 5 times that of air). The similar critical radiant powers required for particle ignition for air and pure oxygen agree qualitatively with results of the hot-gas ignition experiments (1) in which ignition temperature was found to be approximately equal for magnesium particles in air and pure oxygen; these findings suggest that oxygen diffusion is not a controlling factor in the ignition mechanism.

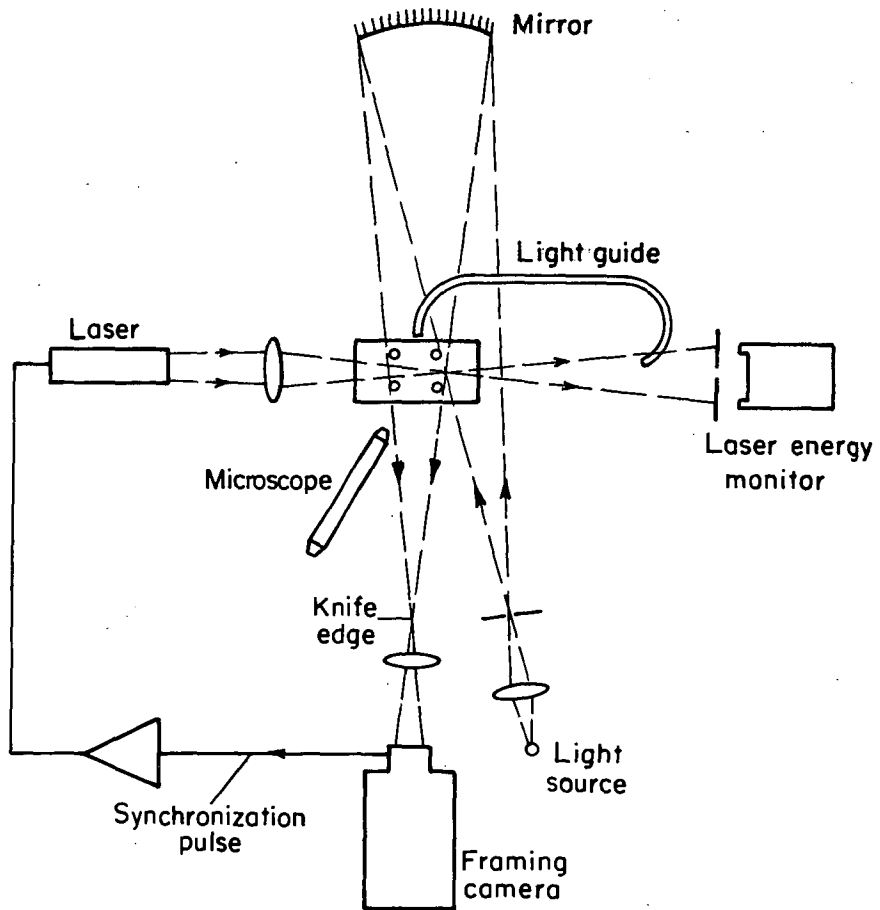


Fig. 2. - Apparatus for schlieren study.

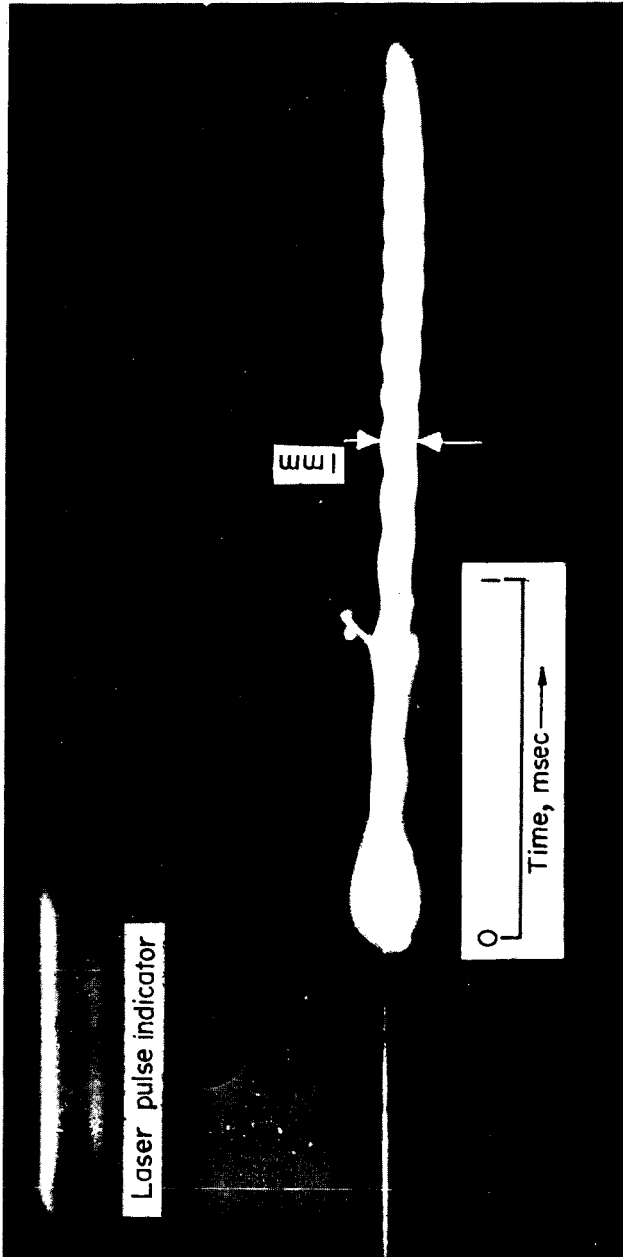


Fig. 3. - Streak photograph of laser ignited 84 micron diameter particle burning in air.



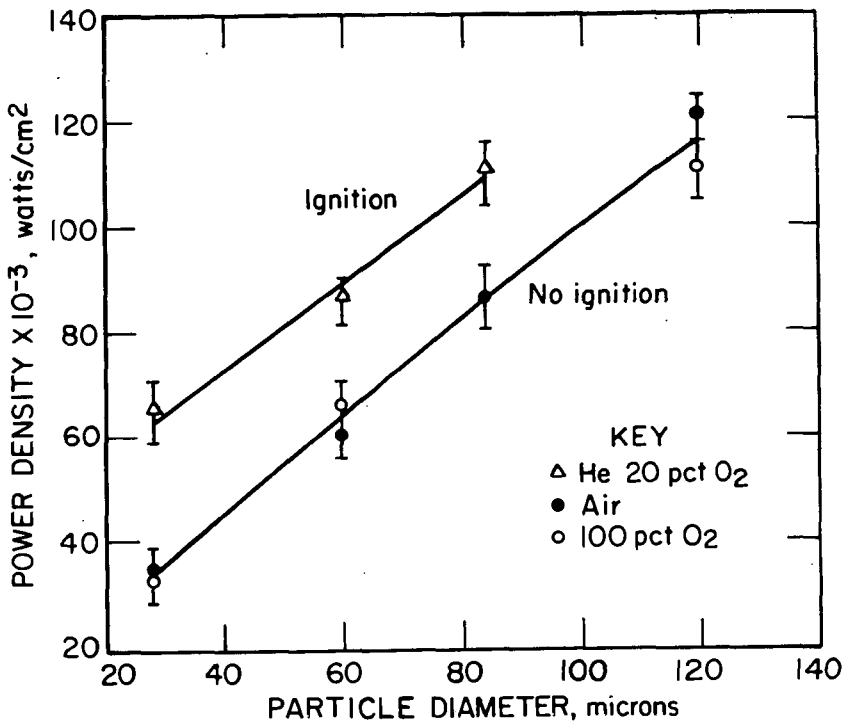


Fig. 4. - Laser power density required to ignite single magnesium particles in various atmospheres.

In additional experiments, single particles (60- and 84-micron diameter) suspended in pure argon and illuminated by a long-duration photoflash light were irradiated by laser powers equal to that previously required for ignition in air. The photoflash light revealed the rapid growth of a cloud surrounding the particle (presumably, condensed metal vapors) near the termination of the laser pulse. The particle was usually still discernable within the cloud.

A sequence of schlieren photographs of a 60-micron-diameter particle irradiated in pure argon is shown in figure 5; the laser power density was again just sufficient to ignite a similar size particle in air. The expanding schlieren image is considered to be mainly due to the expelled hot metal vapor, and is first visible near the mid-point of the laser pulse. A graph of the schlieren growth rate for an irradiated particle suspended in argon and in air is shown in figure 6. The increased growth of the schlieren taken in air is indicative of the magnesium-air reaction process.

In previous investigations of magnesium particle ignition by hot gas, the maximum required gas temperature was 740°C and in the ignition of magnesium ribbon by resistance heating, (9) metal temperatures were estimated to be in the vicinity of the metal melting point (621°C) during the onset of ignition. Our experiments suggest that ignition of a magnesium particle by a 0.9 msec intense radiation pulse occurs in the vapor phase. During the radiation pulse the particle's surface rises to the boiling point, the particle vaporizes, and ignition follows. For critical radiant powers, vaporization begins near the mid-point of the laser pulse and ignition occurs in the proximity of the pulse end.

Table I shows the average burning lifetimes of magnesium particles ignited by critical laser energies as compared to hot-gas ignition experiments. The shorter lifetimes for the laser-induced ignitions are ascribed to particle vaporization prior to ignition and disintegration of the particle during combustion.

TABLE I

Average burning lifetime of laser-ignited magnesium particles in air compared with hot-gas ignition

Diameter, microns	Lifetime, msec	
	Laser ignited	Hot gas ignited
120	5.0	16.8
84	2.4	6.2 (80 micron)
60	.9	1.8 (50 micron)
28	.1	

For the relatively low laser radiant power densities used in our experiments and large thermal diffusivity of the particle, the particle has a relatively small temperature gradient. A rough approximation of this gradient can be obtained from the relationship  $\epsilon E_0 = \lambda dT/dr$ , where  $\epsilon$  is the surface coefficient of absorptivity (assumed to have a value of 0.3),  $E_0$  is the laser beam power density,  $\lambda$  is the metal thermal conductivity having an average value of 1 Joule/cm sec °C,  $T$  is the temperature, and  $r$  is the particle radius. From this relationship the temperature difference between the particle surface and center would be of the order of 9 to 180°C for the 28 to 120 micron particle respectively using the data of figure 4 for the air environment. For a radiantly heated magnesium particle suspended in an inert atmosphere, the time for the particle surface to begin boiling and the quantity of metal vaporized during the pulse can be readily calculated if the following assumptions are made.

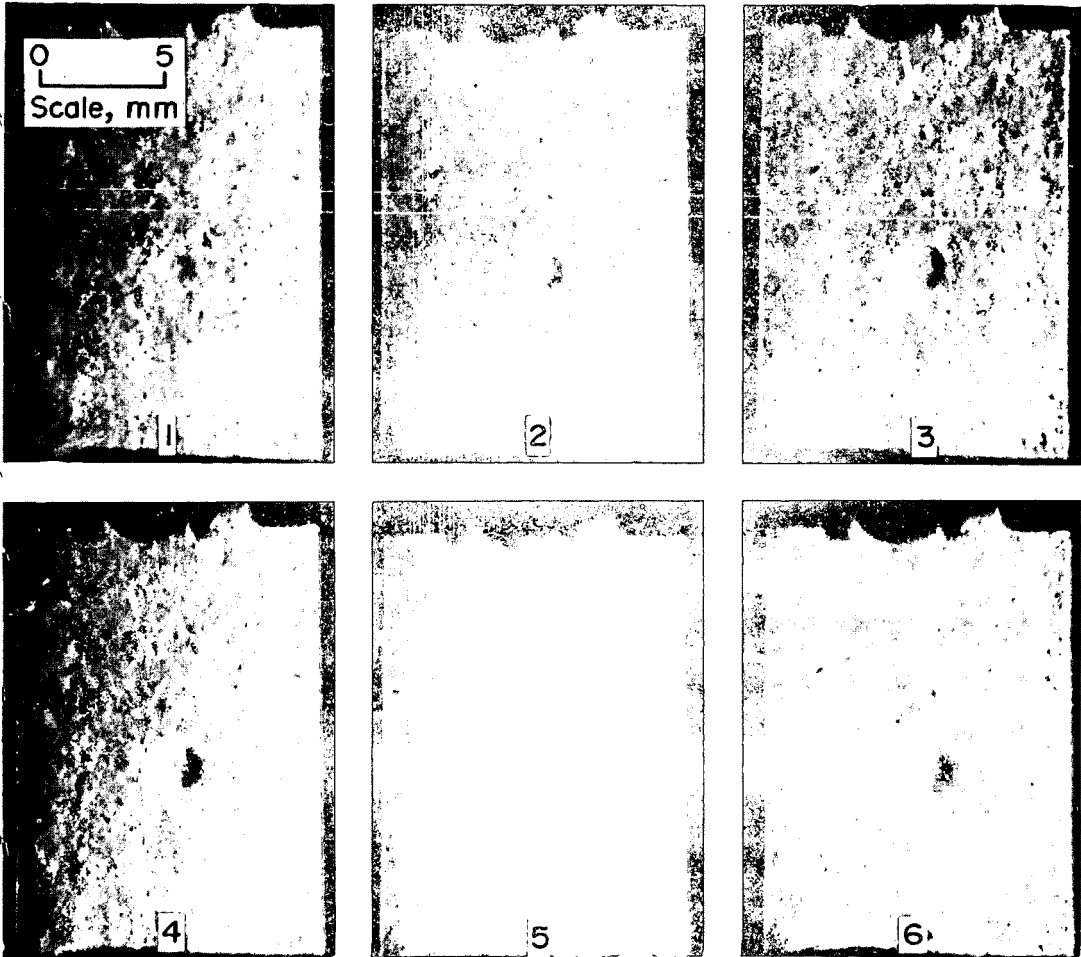


Fig. 5. - Schlieren records of a laser irradiated 60 micron particle  
in pure argon, 0.13 msec between frames.

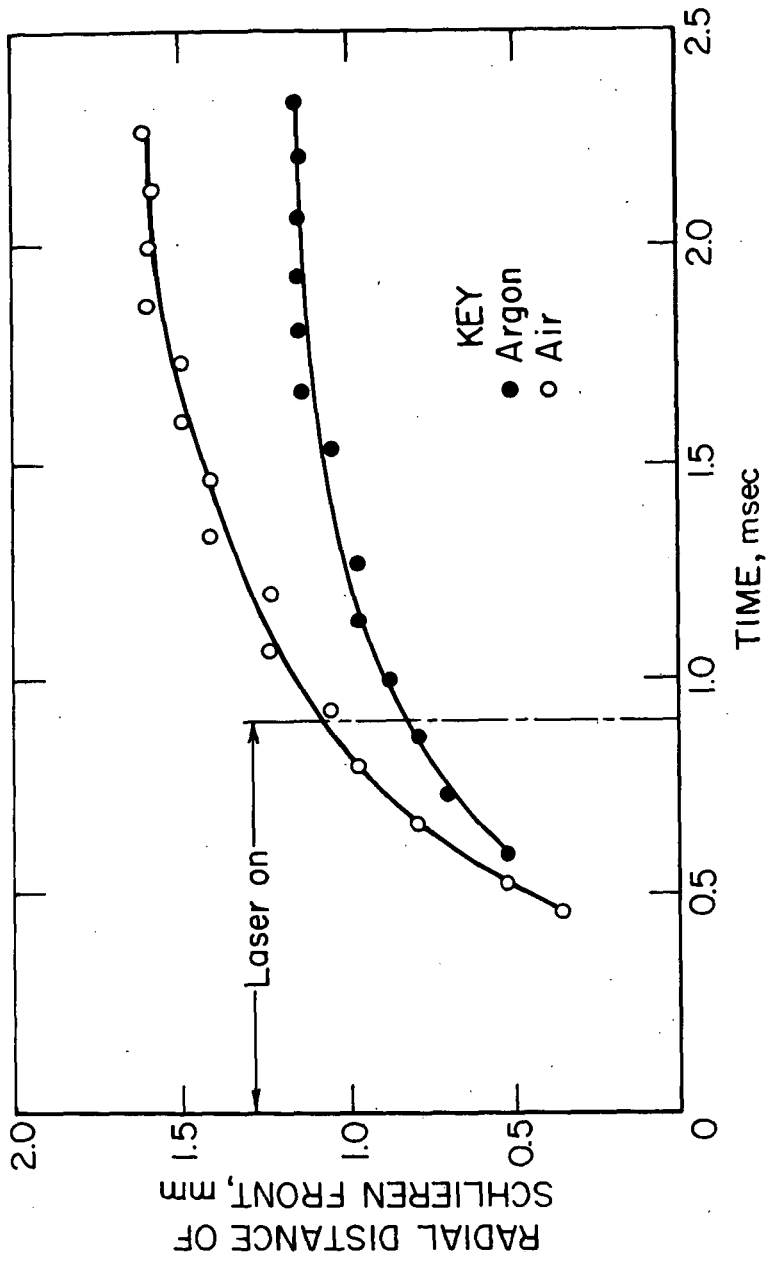


Fig. 6. - Growth of schlieren sphere surrounding a laser irradiated 60 micron diameter magnesium particle.

(1) The radiant flux absorbed by the particle is equally distributed over the entire particle surface. The particle surface coefficient of absorptivity ( $\epsilon$ ) is given an average value of 0.3 -- the thickness of oxide coating on the particle is less than several hundred Angstroms and has little effect on  $\epsilon$  or the heat conduction.

(2) The temperature distribution within the particle is uniform.

(3) Radiative heat losses and heat transfer to the surrounding gases can be neglected.

Using these assumptions, the energy balance equation for the particle can then be written:

$$\epsilon E_0 \pi r^2 t_b = \frac{4}{3} \pi r^3 \rho \left[ C_p \Delta T + H_M \right], \quad (1)$$

where  $E_0$  is the radiant power density in joules/cm<sup>2</sup>-sec,  $r$  is the particle radius in cm,  $t_b$  is the time in seconds for the particle to reach the boiling point,  $\rho$  the average particle density = 1.7 gms/cm<sup>3</sup>,  $C_p$  the average particle specific heat = 1.3 joules/cm °C,  $\Delta T$  the temperature difference from ambient to the metal's boiling point (1100°C), and  $H_M$  is the heat of fusion of the metal (380 joules/gm). The reduction in particle size due to evaporation can be expressed by:

$$E_0 \pi r^2 = L_v \rho 4 \pi r^2 \frac{dr}{dt} \quad (2)$$

where  $L_v$  is the heat of vaporization (5500 joules/gm) and  $t$  is the time remaining in the laser pulse after the particle surface reaches the boiling point.

Using these equations, table II shows the calculated times for particles to reach the boiling point and the final particle size for critical laser powers obtained from figure 4 for air environments.

TABLE II

Boiling times and final particle size for  
laser irradiation at critical power densities

Particle diameter, microns	Time to boiling point, msec	Final particle diameter, microns
28	0.52	26
60	.62	56
84	.65	80
120	.70	116

The calculated times to reach the boiling point for the small particles (table II) are approximately 20 percent larger than our experimental results; the increased calculated values for the larger particles are probably due to our assumption of a uniform temperature within the particle. The small reduction in particle size due to vaporization prior to ignition accounts only partially for the short burning lifetimes noted in our experiments. In addition, the possible absorption of laser energy by the vaporized metal would be effective in reducing the particle absorptivity and thereby lessen the vaporization rate. Results of this analysis suggest that particle disintegration is the most significant factor in decreasing the burning lifetimes.

### Incendivity

Figure 7 shows a plot of the critical radiant power density required for the incandive ignition of stoichiometric methane-air mixtures by irradiatively heated single magnesium particles. For comparison purposes, the curve of particle ignition in air from figure 4 is also included. It is significant to note that the 120-micron-diameter particle requires less radiant power for incandive ignition than for particle ignition in air, whereas critical radiant power for the 84- and 60-micron particles appear to be similar to the values obtained in air, and the smaller 50- and 28-micron particles need greater radiant power for incandivity than for particle ignition. This latter observation indicates that the smaller particles can be burned in a flammable environment without igniting the environment.

Table III lists the energy released during combustion of magnesium particles and the computed radiant energy absorbed by the particles during the laser pulse using equations 1 and 2 and the critical radiant powers for incandivity shown in figure 7. Information for a 20-micron-diameter particle, which did not ignite the methane-air mixture when irradiated with radiant power densities as high as 270 watts/cm<sup>2</sup>, is also listed in this table for comparison purposes.

TABLE III

Energy released during combustion and radiant energy  
absorbed by magnesium particles during irradiation

Particle diameter, microns	Energy of combustion, millijoules	Energy absorption, millijoules
120	36.7	2.7
84	12.6	1.3
60	4.6	.5
50	2.7	.4
28	.5	.1
20	.16	.05

All the particles listed in table III except for the 28 and 20 micron, have greater absorbed energies than the reported (0.25 mJ) minimum spark ignition energy for stoichiometric methane-air mixtures. However, gas ignition by relatively slowly heated hot bodies should require considerably more energy than by short duration sparks. Nevertheless, since the 120-micron particle requires much less radiant flux for incandive ignition than for particle ignition in air, then this particle apparently ignites the methane-air mixture by hot-body mechanisms. Therefore, neglecting any magnesium-O<sub>2</sub> reaction, the minimum ignition energy of the gas mixture by small hot particles (1100°C) should be of the order of 3 mJ. The smaller particles apparently ignite first then in turn ignite the gas mixture since the energy required for incandive ignition is as great or greater than that required for particle ignition. The drop in the radiant power density required for incandivity ignition for the 60-micron particle shown in figure 7 is evidently due to an interaction of particle ignition and methane-air ignition processes. The 50- and 28-micron particles require energies in excess of particle ignition in order to shorten their burning lifetimes and thereby enhance the incandive process. The combustion and absorbed energy calculated for the 20-micron particle is seen to be less than the spark ignition requirements, therefore nonignitability by this particle size is not surprising. Rae(7) estimated the minimum mass of rapidly moving and burning magnesium particles capable of igniting a methane-air mixture to be 1.0 microgram which corresponds to a 105-micron-diameter sphere. This value is almost fourfold greater than the minimum particle size used in our experiments and illustrates the probable effect

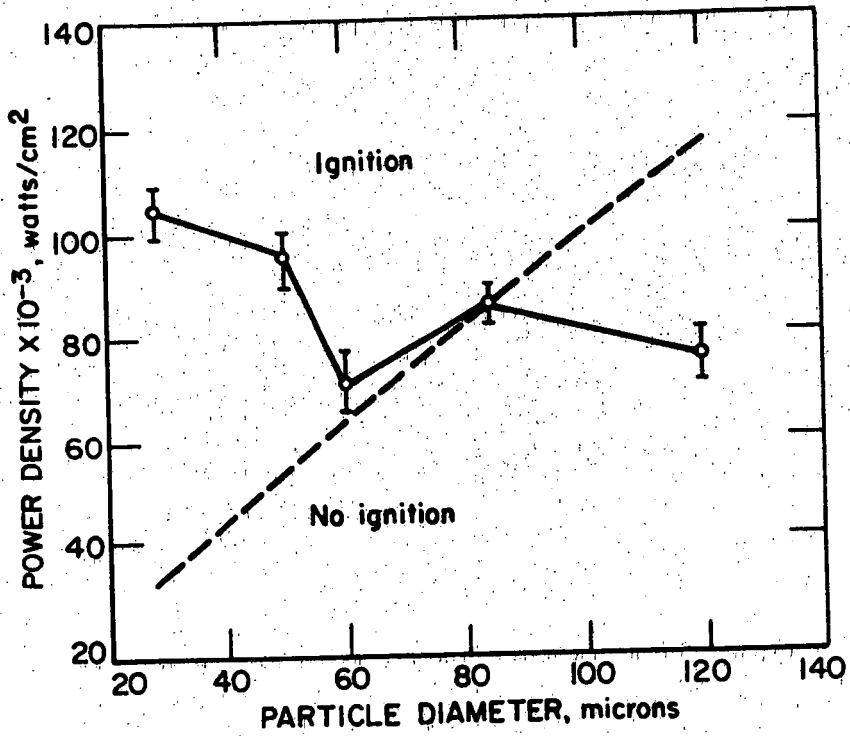


Fig. 7. - Laser power density required for single magnesium particle to ignite stoichiometric methane-air mixture.

of particle motion and burning lifetime on incandive efficiency. The effect of particle size and motion on hot-body ignition is demonstrated in work by Silver(5) and Paterson(6) who ignited gas mixtures with heated platinum and quartz spheres; their results showed that ignition temperature of the spheres increased with decreasing sphere diameter and increasing sphere velocity through the fuel mixture.

Figure 8 shows a sequence of schlieren photographs obtained during the irradiation of a 60-micron-diameter magnesium particle suspended in a stoichiometric methane-air mixture. Figure 9 is a plot of the growth of the schlieren image during the irradiation of a single 60-micron and a 120-micron-diameter particle using the radiant power density (critical) necessary for incandive ignition of stoichiometric methane-air mixtures. Figure 10 is a similar plot for a 120-micron particle irradiated by critical and twice-critical radiant power densities. The results of these studies suggest that the incandive mechanism can be described as a three-stage process; the first stage being an extremely rapid growth of a spherical envelope surrounding the particle resulting from the expanding hot metal vapors and magnesium-methane-air reaction; the second stage is characterized by a much slower growth rate and is considered to result from the continued pre-ignition process of the methane-air reaction; the third stage is the methane-air combustion front and corresponds to an expanding front traveling at a constant velocity. The rate of growth of all stages is observed to depend on laser energy and particle size. Stoichiometric methane-air flame speeds should be about 270 cm/sec. This corresponds approximately to the value obtained for the 120-micron particle irradiated by twice critical power shown in figure 10. Hot-wire ignition experiments of methane-air systems by Ashman(10) showed a similar pattern, a decreased flame speed with a decrease in wire temperature. His results also indicated that an exothermic reaction occurred in the methane-air pre-ignition period. The distance traveled by the wave to the beginning of the methane-air combustion front varies from about 3 to 5 mm, this is about one-half the distance of corresponding zones as measured by Ashman.



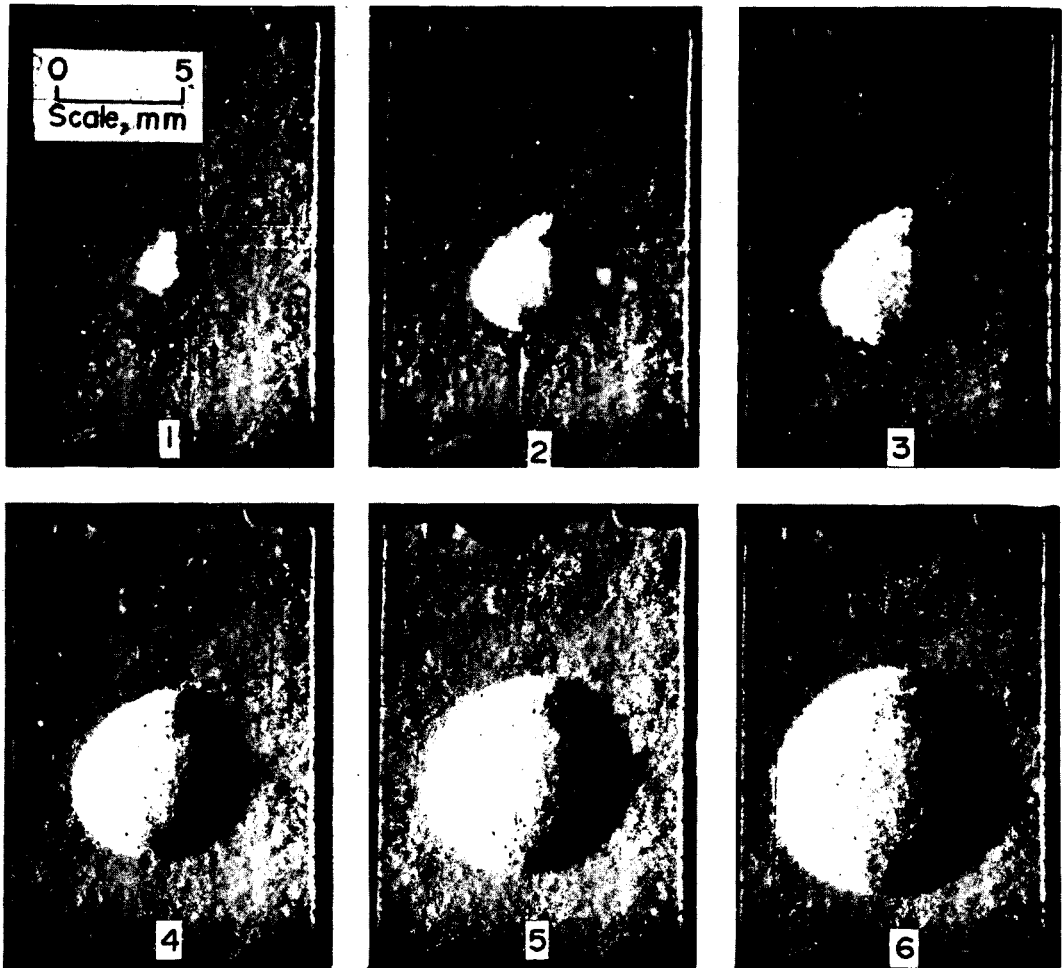


Fig. 8. - Schlieren record of laser irradiated 60 micron particle  
in stoichiometric methane-air mixture, 0.27 msec between frames.

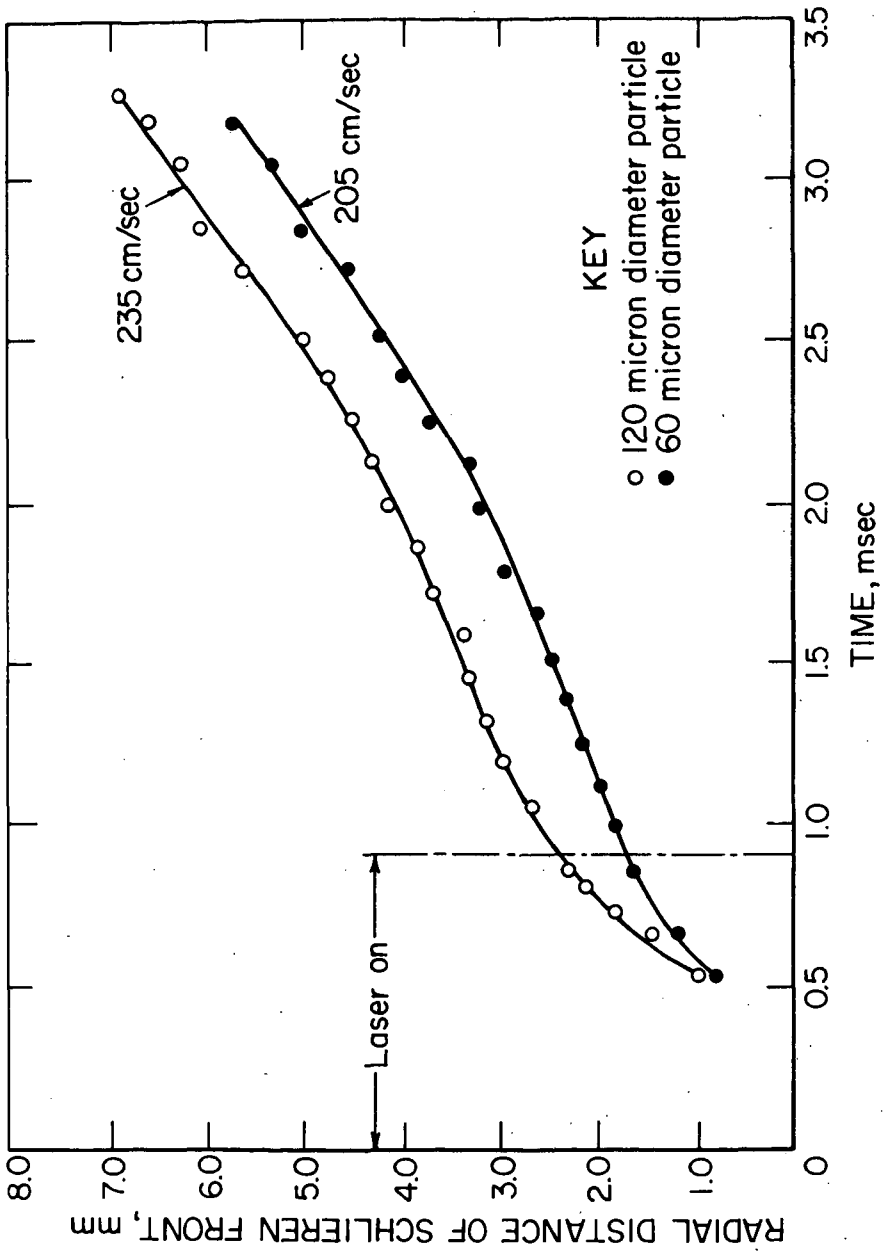


Fig. 9.- Schlieren growth surrounding a single magnesium particle irradiated by critical laser power density to ignite stoichiometric methane-air mixture.

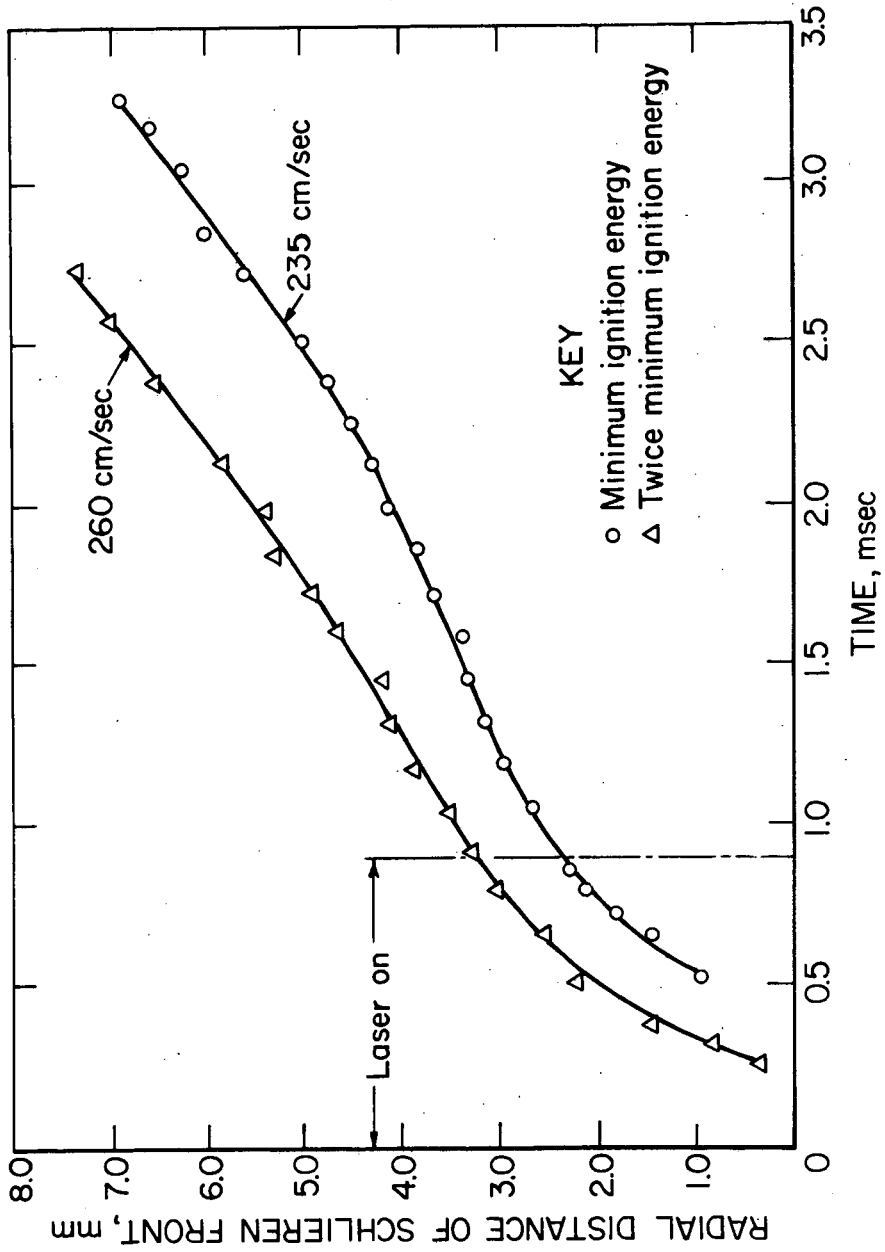


Fig. 10. - Schlieren growth surrounding a single 120 micron diameter magnesium particle during laser irradiation and ignition of stoichiometric methane-air mixture.

References

- 1) Cassel, H. M., and Liebman, I., "The Cooperative Mechanism in the Ignition of Dust Dispersions", *Combustion and Flame*, 1959, 3, 467.
- 2) Friedman, R., and Macek, A., "Ignition and Combustion of Aluminum Particles in Hot Ambient Gases", *Combustion and Flame*, 1962, 6, 9-19.
- 3) Cassel, H. M., and Liebman, I., "Combustion of Magnesium Particles II - Ignition Temperatures and Thermal Conductivities of Ambient Atmospheres", *Combustion and Flame*, 1963, 7, 79-81.
- 4) Cassel, H. M., and Liebman, I., "Radiative Transfer in Dust Flames", *Sixth Symposium (International) on Combustion* (Reinhold Publishing Corp., New York, 1957), 602-605.
- 5) Silver, R. S., "Ignition of Gaseous Mixtures by Hot Particles", *Phil. Mag.*, 1937, Series 7, 23, 633.
- 6) Paterson, S., "Ignition of Inflammable Gases by Hot Moving Particles II", *Phil. Mag.*, 1940, Series 7, 30, 437.
- 7) Rae, D., "Ignition of Explosive Gas Mixtures by Small Combustible Particles: Part I - Ignition by Particles of Pyrophor Bar", *S.M.R.E. Research Report No. 129*, 1956.
- 8) Nelson, L. S., Richardson, N. L., and Prentice, J. L., "Apparatus for the Production and Ignition of Metal Droplets with a Pulsed Laser", *The Review of Scientific Instruments*, 1968, Vol. 39, No. 5, 744-747.
- 9) Brzustowski, T. A., and Glassman, I., "Vapor-Phase Diffusion Flames in The Combustion of Magnesium and Aluminum: II. Experimental Observations in Oxygen Atmospheres", *Progress in Astronautics and Aeronautics*, Vol. 15 (Academic Press, New York, 1964).
- 10) Ashman, L. E., and Buchler, A., "The Ignition of Gases by Electrically Heated Wires", *Combustion and Flame*, 1961, Vol. 5, No. 2, 113-120.